Transforming descending input into behavior: The organization of premotor circuits in the *Drosophila* Male Adult Nerve Cord connectome

Cheong, H. S. J.*[1,5], Eichler, K.*[2], Stuerner, T.*[3,2], Asinof, S. K.[1], Champion, A. S.[2,3], Marin, E. C.[2], Oram, T. B.[1], Sumathipala, M.[1], Venkatasubramanian, L.[3,2], Namiki, S.[4], Siwanowicz, I.[1], Costa, M.[2], Berg, S.[1], Janelia FlyEM Project Team[1], Jefferis, G. S. X. E.[3,2†], Card, G. M.[1,5†]

[1]Janelia Research Campus, Howard Hughes Medical Institute, Ashburn, United States
[2]*Drosophila* Connectomics Group, Department of Zoology, University of Cambridge, Downing Street, Cambridge, UK
[3]Neurobiology Division, MRC Laboratory of Molecular Biology, Cambridge, UK
[4]Research Center for Advanced Science and Technology, University of Tokyo, Tokyo, Japan
[5]Zuckerman Institute, Columbia University, New York, United States

*These authors contributed equally to this work
[†]Correspondence to: gwyneth.card@columbia.edu and jefferis@mrc-lmb.cam.ac.uk

Abstract

In most animals, a relatively small number of descending neurons (DNs) connect higher brain centers in the animal's head to motor neurons (MNs) in the nerve cord of the animal's body that effect movement of the limbs. To understand how brain signals generate behavior, it is critical to understand how these descending pathways are organized onto the body MNs. In the fly, *Drosophila melanogaster*, MNs controlling muscles in the leg, wing, and other motor systems reside in a ventral nerve cord (VNC), analogous to the mammalian spinal cord. In companion papers, we introduced a densely-reconstructed connectome of the *Drosophila* Male Adult Nerve Cord (MANC, Takemura et al., 2023), including cell type and developmental lineage annotation (Marin et al., 2023), which provides complete VNC connectivity at synaptic resolution. Here, we present a first look at the organization of the VNC networks connecting DNs to MNs based on this new connectome information. We proofread and curated all DNs and MNs to ensure accuracy and reliability, then systematically matched DN axon terminals and MN dendrites with light microscopy data to link their VNC morphology with their brain inputs or muscle targets. We report both broad organizational patterns of the entire network and fine-scale analysis of selected circuits of interest. We discover that direct DN-MN connections are infrequent and identify communities of intrinsic neurons linked to control of different motor systems, including putative ventral circuits for walking, dorsal circuits for flight steering and power generation, and intermediate circuits in the lower tectulum for coordinated action of wings and legs. Our analysis generates hypotheses for future functional experiments and, together with the MANC connectome, empowers others to investigate these and other circuits of the *Drosophila* ventral nerve cord in richer mechanistic detail.

1 Introduction

The fly ventral nerve cord (VNC) is a vital part of its central nervous system. It receives input both from the brain and from sensors of the fly's body and integrates these to drive local circuits that control motor output to the neck, wings, halteres, legs, and abdomen. It also contains ascending neurons that feed back information about ongoing circuit activity to the brain (Figure 1A). Premotor circuits in the VNC thus must perform many tasks, including decoding descending commands from the brain, locally modulating motor output based on immediate incoming sensory information, controlling the muscles of individual limbs and body parts, and coordinating movements across multiple body parts with millisecond precision. The organizational logic of the individual circuits that accomplish these feats remains largely unknown. Here, we present a system-wide look at the structure of premotor circuits by using the fly Male Adult Nerve Cord (MANC) connectome to examine patterns of synaptic connectivity in the networks connecting brain input, carried by descending neurons (DNs), to motor output, transmitted by motor neurons (MNs).

DNs as a population represent a bottleneck in the transmission of information between sensory processing areas in the brain and premotor circuits in the nerve cord. In the brain, DNs chiefly receive input from the brain's lateral accessory lobe (LAL) and posterior slope (PS), regions implicated in navigation and visual motion processing, the posterior lateral and ventrolateral protocerebra (PLP, PVLP), regions implicated in escape and other rapid responses to salient visual stimuli, and the gnathal ganglion (GNG), a region involved in mechanosensory, gustatory and locomotor responses (Hsu and Bhandawat, 2016; Namiki et al., 2018). In the VNC, DNs innervate either VNC layers that contain wing/neck/haltere MNs or layers containing leg MNs, but rarely both (Namiki et al., 2018). A separate subset of DNs terminate in the posterior neuropil, where motor neurons controlling the abdominal muscles reside, and control abdominal motor behavior such as copulation (Pavlou et al., 2016) and oviposition (Castellanos et al., 2013). Thus, most DNs carry information specific to a particular motor system. One exception is a subset of DNs that targets intermediate VNC layers, which do not contain any motor neurons but likely coordinate behaviors requiring both legs and wings, such as takeoff (Court et al., 2020; Namiki et al., 2018). Previous studies estimated the number of DNs to be roughly 1000, which is 1-2 orders of magnitude fewer than the number of neurons in the brain or VNC networks that they connect (Hsu and Bhandawat, 2016; Namiki et al., 2018). The brain thus provides input to the VNC in the form of a relatively compressed code across a small number of neurons targeted to specific motor systems.

Many DN types initiate motor activity when activated. In some cases DN activity triggers clear motor programs, such as walking, flight, takeoff, or singing (Bidaye et al., 2014; Cande et al., 2018; Guo et al., 2022; Koto et al., 1981; McKellar et al., 2019; Rayshubskiy et al., 2020; von Philipsborn et al., 2011) and in other cases it modulates ongoing motor activity (Aymanns et al., 2022; Namiki et al., 2022). Some DN types produce uncoordinated actions when optogenetically activated (Cande et al., 2018), suggesting that some behavioral patterning requires the simultaneous activation of multiple DNs or DN activation during the correct internal state. Further supporting DN population encoding of behavior, silencing DNs often does not eliminate

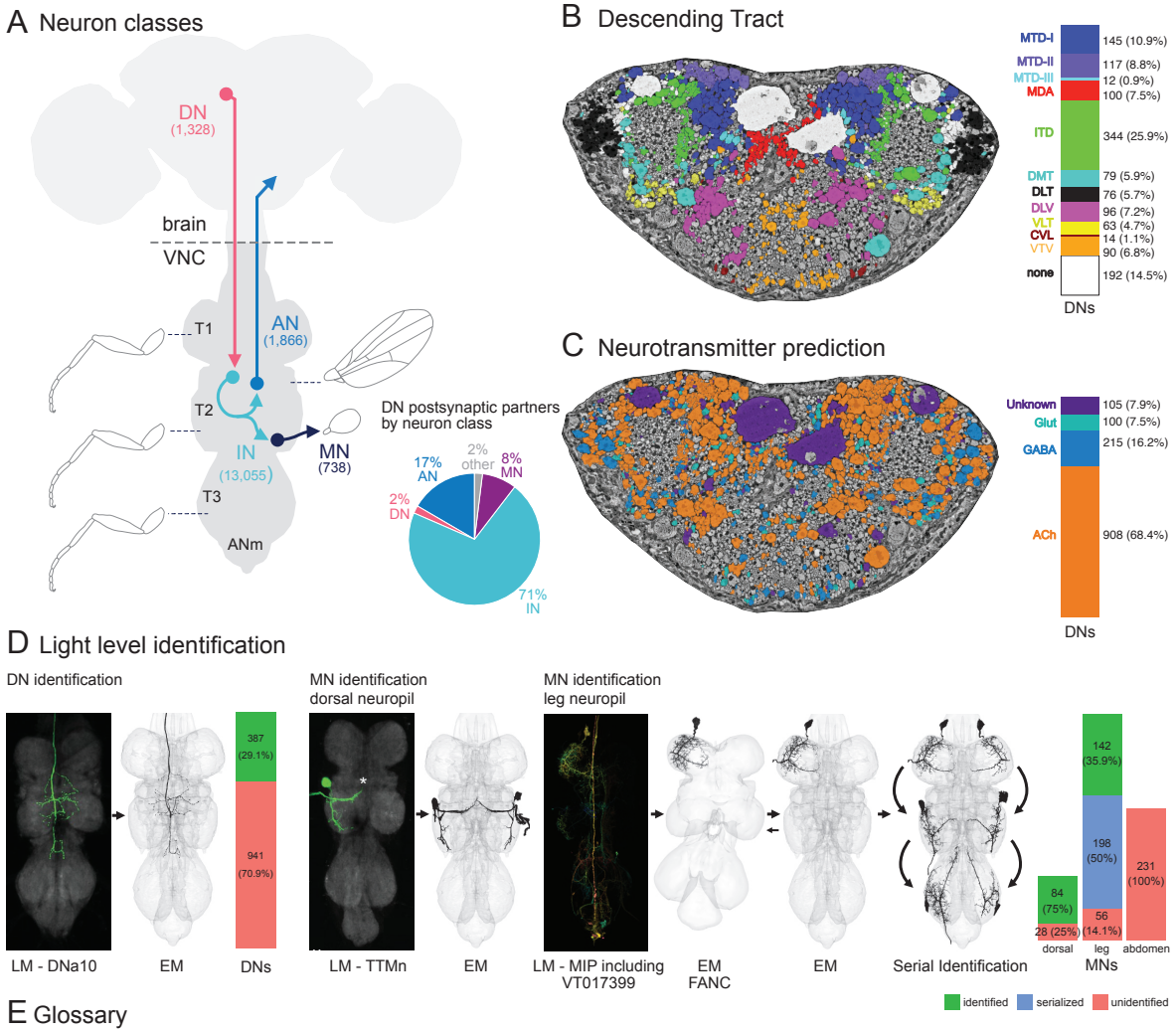

E Glossary

soma_ neuromere	neuromere of soma origin
soma_side	side of soma origin
root_side	axon entry side
group	matched within neuromere
serial	matched across neuromeres
serial motif	pattern of serial homology
class	broadest cell class (motor, sensory, etc)
subclass	more detailed cell class
origin	neuropil with > 80% of input
target	neuropil with > 80% of output
systematic_type	cell type, systematic nomenclature
type	cell type
entry_nerve	nerve by which axon enters VNC
exit_nerve	nerve by which axon exits VNC
predicted nt	"winning" neurotransmitter prediction for a neuron (>0.7)
predicted nt prob	measure of confidence of "winning" neurotransmitter prediction

Descending neuron (DN)
systematic_type = DN + target + #

If DN is matched to light level data
type = literature name (e.g., DNa01)

If DN does not have a light level match
type = **systematic_type** (e.g., DNxl132)

instance = root_side (e.g., DNa01_R)

Motor neuron (MN)
systematic_type = MN + target + #

If MN is matched to light level data
type = literature name (e.g., b1 MN)

If MN does not have a light level match
type = **systematic_type** (e.g., MNnm06)

instance = root_side (e.g., MNnm06_L)

Figure 1: Overview of MANC connectome. A. Schematic of the *Drosophila melanogaster* central nervous system, including brain and ventral nerve cord (VNC). Neuron classes focused on in this study: descending neurons (DNs), intrinsic neurons (INs), motor neurons (MNs), and ascending neurons (ANs). Numbers indicate the total number of that neuron class found in MANC. Approximate areas corresponding to the neuropils controlling a few of the fly's primary motor systems (leg, wing, haltere) indicated by dashed lines. The three thoracic segments are indicated with T1, T2 and T3. The abdominal neuropil (ANm) controls movements of the abdomen. Pie chart shows the neuron class composition of postsynaptic partners of all DNs, the majority of which are intrinsic neurons. **B-C.** Cross section of the *D. melanogaster* neck connective at the location of the black dashed line in **A**. DN profiles are color coded by tract membership (**B**, see Figure 2) and predicted neurotransmitter (**C**, see Figure 4). Side bars show percentage of DNs per tract or predicted neurotransmitter. Predicted neurotransmitter type was 'unknown' if prediction probability was <0.7). *(cont.)*

Figure 1 *(cont.)* **D.** DNs and MNs were identified by matching MANC EM reconstructed neurons to published light microscopic (LM) level descriptions of DNs (mainly (Namiki et al., 2018), for more references see Supplementary File 1) and MNs either manually by eye or aided by neuronbridge queries of maximum intensity projections (MIP) of driver lines against the EM dataset. Left, DN identification example: A neuronbridge query for SS02384, which was described to cover DNa10 (Namiki et al., 2018), revealed group 10506 to be a good match. 29.1% of MANC DNs matched a previous DN description in the literature. Center, MN identification example for the dorsal neuropils. Matching to SS02623 (which contains the tergotrochanteral muscle motor neuron, TTMn) revealed group 10068. Right, MN identification example for the leg neuropils. A recent study identified all leg MNs in the T1 compartment (FANC, Azevedo et al., 2020). T1 MNs in this dataset (MANC) were matched to FANC using NBLAST. Utilizing both datasets aided LM identification of leg MNs in both FANC and MANC. Further, serially homologous neurons of T1 leg MNs in T2 and T3 were identified (see Materials & Methods). The bar chart shows the status of LM identification of MNs. 75% of dorsal neuropil MNs are matched to previous descriptions. 35.9% of leg MNs are matched to FANC and thus their muscle targets are identified. By identifying serial homologous neurons of the T1 MNs the muscle targets of an additional 50% of leg MNs are characterized. We did not match abdominal MNs to light level descriptions in this study. **E.** Left, glossary of terms and acronyms used in this study. Right, systematic naming of DNs and MNs. For more information on other neuron classes and terms, see accompanying paper (Marin et al., 2023).

Figure 1—Supplement 1: Overview of Identified DNs. Morphology of DN types described by Namiki et al. (2018) identified in the EM volume. Nomenclature according to Namiki et al. (2018). Three types could not be identified in the EM dataset (indicated by an empty VNC outline and “not found”). See Supplementary File 1 for more information on identification confidence and other synonyms of DNs in the literature.

the action that activation of the same DN initiates (Ache et al., 2019). Thus, a reasonable framework for DN input to the VNC based on current knowledge is that DN activity represents higher-order behavioral modules carried either by individual DNs acting more like “command neurons" or by groups, or small populations, of DNs whose combined activity is required to produce the correct behavior pattern.

On the motor output end, MNs in the fly VNC support five primary motor systems: the wings, legs, halteres, neck, and abdomen. By patterning activity onto MNs in these systems, VNC premotor circuits are able to control two distinct forms of locomotion (walking and flying) and a wide array of behaviors that combine actions from multiple motor systems (e.g. escape, grooming, courtship, aggression and oviposition). To understand how VNC premotor circuits create these diverse behaviors, it is necessary to consider the biomechanics of each motor system being controlled. In particular, wing and leg motor systems have very different mechanical arrangements, which would suggest the structure of their underlying control circuits may also differ greatly.

In dipterans, such as *Drosophila*, the wing motor system includes three classes of muscles: power, steering, and indirect control muscles (Dickinson and Tu, 1997). The power muscles are divided into two types that attach orthogonally relative to each other across the thorax, such that when one set contracts it deforms the thoracic exoskeleton and stretches the other. The muscles themselves are stretch-activated, meaning that once started, the power muscles alternately activate each other, setting up the rhythmic deformations of the thorax that flap the wings, providing power during flight and the primary oscillations used in courtship song (Dickinson and Tu, 1997; Ewing, 1977). Power muscle oscillations will continue as long as activity in MNs continues to provide an influx of calcium to the muscles. However, this can be asynchronous and does not need to occur at the frequency of the wingstroke (Dickinson and Tu, 1997). Steering is accomplished through synchronous and direct control of wing hinge elements by the steering muscles, a series of 14 muscles that attach directly to three of the four axillary sclerites that form the wing hinge (the first, third and fourth axillary sclerites: i, iii, and hg) and the basalare sclerite (b) anterior of the wing hinge (Deora et al., 2017; Dickinson and Tu, 1997). Timing is critical for these muscles as the orientation and movement direction of the wing is determined by the phase of the wingstroke at which they are activated (Egelhaaf, 1989; Götz, 1983; Heide, 1983, 1975; Heide and Götz, 1996). Finally, of the indirect control muscles, pleurosternal (ps) and tergopleural (tp) muscles control thoracic stiffness and resonant properties, thereby indirectly modulating wingbeat amplitude (Dickinson and Tu, 1997), while tergotrochanteral muscle (TTM) activation rapidly depresses the middle legs and ‘jump-starts’ the power muscles during escape takeoffs (Dickinson and Tu, 1997).

In contrast, the leg motor system of the fly includes six separate jointed appendages, each of which is composed of 10 segments (coxa, trochanter, femur, tibia, five tarsal segments and the claw or pretarsus). However, only the proximal joints are “true” joints that can be actively moved, as there are no muscles internal to the tarsal segments. The musculature of the *Drosophila* leg consists of 13 muscle groups confined within the proximal leg segments, and another five in the thorax that insert in the leg (Azevedo et al., 2022; Brierley et al., 2012). These leg muscles are estimated to be innervated by around 70 MNs in each leg, that originate from ~15 hemilineages

(Baek and Mann, 2009; Brierley et al., 2012; Phelps et al., 2021). Muscles in the leg are not innervated uniformly; indeed, in the T1 legs the number of MNs per muscle varies by as much as an order of magnitude (Azevedo et al., 2022; Baek and Mann, 2009). Individual MNs also exhibit considerable heterogeneity in their intrinsic properties, correlating with the speed and force with which they activate downstream muscles as well as the order in which they are recruited by afferents (Azevedo et al., 2022, 2020). Complex movements require the coordinated control of multiple muscles (such as the activation of one muscle at the same time as the deactivation as its opposing counterpart). Premotor circuits that produce fluid patterns of motion in a single leg (e.g., repeated cycles of swing and stance associated with walking forwards) must therefore be capable of activating or suppressing tens of MNs in an appropriate sequence to actuate movement at each of the fly's leg joints.

Compared to the wing and leg motor systems, less is known about the neck, haltere, and abdominal motor systems. As abdominal MNs in MANC, while reconstructed and grouped, still require future identification efforts to determine their muscle targets, we do not focus on the abdominal motor system in this paper. Neck muscles serve to move the fly's head, which is critical for gaze-stabilization as *Drosophila* are highly visual animals, yet have compound eyes fused to their head. So, with the exception of small retinal movements (Fenk et al., 2022), neck muscles are responsible for minimizing motion blur during flight maneuvers. The neck muscles and MNs are not yet well-described in *Drosophila* but a comprehensive description of the neck motor system is available in the blowfly, *Calliphora erythrocephala* (Strausfeld et al., 1987). Of note, fly neck MNs are split between those residing in the VNC and the brain, and so the neck MNs are not complete in the MANC dataset. The halteres are appendages derived from hindwings that in *Drosophila* beat antiphase to the wings during flight. They are equipped with sensors at their base that allow them to detect Coriolis forces and hence provide fast mechanosensory feedback to the flight system to enable rapid maneuvering. Similar to the wing system, the haltere motor system consists of a reduced set of eight muscles that are homologous to the wing muscles, divided into a single power muscle and seven steering muscles (Dickerson et al., 2019). Movements of the neck and halteres are tightly coordinated with the wings during flight through both mechanical linkages and neural control (Deora et al., 2021, 2015). As such, during the flight state, they may be considered to be under the control of a single "flight" motor system, as suggested by the fusion of neck, wing, and haltere neuropils into a single dorsal "upper tectulum" layer in the VNC.

VNC motor control circuits are further patterned by developmental identity. Identified neuroblasts (stem cells) generate neurons in stereotyped lineages. Single hemilineages often give rise to neurons which are implicated in a single or related set of motor functions (Harris et al., 2015) and in many cases are capable of semi-autonomous patterned motor output. Indeed, experiments with decapitated flies show that the VNC local circuitry can, with mechanical or optogenetic stimulation (or occasionally spontaneously), generate the appropriate signals for patterned motor activities including walking, flight, grooming, and courtship song (Clyne and Miesenböck, 2008; Gao et al., 2013; Harris et al., 2015; Vandervorst and Ghysen, 1980). This arrangement could allow signals from the brain to act in a command or modulatory manner on motor output, independently of the details of the desired patterned motor output.

Despite decades of investigation into DNs, VNC circuits, and their role in behavior, only small portions of VNC circuitry and specific pathways are well-understood, and we lack both large- and fine-scale understanding of circuit connectivity and organization across the VNC. In recent years, electron microscopy-based (EM) connectomics has emerged as a powerful tool to dissect and understand neural circuitry, enabling the reconstruction of neurons from EM imagery and quantification of synapse connectivity strength, thus giving us a direct method to analyze neural pathways at synaptic resolution. Several large connectomics efforts have been undertaken in *Drosophila* including the larval CNS (Ohyama et al., 2015; Winding et al., 2023), Female Adult Fly Brain (Dorkenwald et al., 2022; Zheng et al., 2018), Hemibrain (Scheffer et al., 2020), and Female Adult Nerve Cord (Phelps et al., 2021), which are further enhanced by development of bioinformatics tools for analyzing neuroanatomical and connectomics data (e.g. Bates et al., 2020). Of note, the Female Adult Nerve Cord (FANC) (Phelps et al., 2021) is the first complete EM volume of the adult *Drosophila* VNC, providing valuable insight into motor neuron morphology, count and organization in the VNC thoracic segments, as well as allowing labs to further reconstruct and investigate VNC circuits of interest. More recently, work based on proofreading an automated segmentation of the FANC volume has identified all T1 leg MNs and the majority of wing MNs in EM by matching to light-level data (Azevedo et al., 2022). A concurrent work to ours has also further reconstructed and analyzed the connectivity of the direct upstream partners of these MNs, giving us insights into synapse-resolution connectivity and organization of the first layer of premotor neurons upstream of motor output (Lesser et al., 2023).

In the Hemibrain project, advances in sample preparation, EM methods and acquisition, image stack alignment, autosegmentation, synapse prediction, and proofreading software and methods, in combination with efforts of a dedicated proofreading team, made practical the production of large densely reconstructed connectomes where users need only query neurons or circuits of interest through a web or software interface (Plaza et al., 2022; Scheffer et al., 2020). Using these advances, the Janelia FlyEM project team has now produced the *Drosophila* Male Adult Nerve Cord (MANC) connectome (Takemura et al., 2023), a densely reconstructed connectivity map of the entire fly VNC. Proofreading and annotation teams have further added a rich set of metadata to all neurons of the VNC, describing neuron properties including (but not limited to) neuron class, hemilineage, morphological groupings, serial homology, and systematic typing based on morphology and connectivity (Marin et al., 2023; Takemura et al., 2023), allowing the intrepid neurobiologist to more easily mine the VNC connectome for neurons or circuits of interest.

Here, we carry out focused proofreading and annotation of all DNs and MNs in MANC, and match their cell types to published light-level imagery when possible. We then broadly survey DN-to-MN connectivity with system-wide analyses examining feedforward information flow. We further specifically investigate motor circuit organization in the wing tectulum, leg neuropils, and lower tectulum. Within these analyses, we focus on examining select DNs with known or putative function in locomotion and navigation, salient visual responses, memory and learning, and olfactory responses. We present a general overview of VNC pre-motor network organization as well as detailed connectivity graphs of some of these behavioral circuits of interest.

2 Results

2.1 Connectome generation and cell typing

Creation and cell type annotation of the MANC connectome are necessary precursors to analysis of DN-to-MN pathways. These aspects of the project are presented in two companion papers: Takemura et al. (2023), which describes generation of the MANC connectome, and Marin et al. (2023), which describes cell type annotation. Briefly, MANC used an optimized connectome production pipeline consisting of a system of sample preparation, EM imaging, volume assembly (stitching), automated segmentation, and synapse prediction. Following initial segmentation of the EM volume, trained proofreaders manually examined the morphology of all putative VNC neurons, corrected major false merges, and connected major neurite segments. These efforts captured 42% of the overall synaptic connectivity in the VNC, ranging from 33 to 62% for individual neuropils. During proofreading, all MANC neurons were categorized into one of the following classes: intrinsic neuron (IN), descending neuron (DN), ascending neuron (AN), motor neuron (MN), efferent neuron (EN), efferent ascending (EA), sensory neuron (SN) and sensory ascending (SA). In total, 23,569 neurons were reconstructed and annotated in this dataset, which comprises 13059 INs, 1328 DNs, 1866 ANs, 737 MNs, 94 ENs, 8 EAs, 5938 SNs, and 539 SAs. All neurons were further categorized by morphology and synaptic connectivity into a 'group', and, where applicable, into a 'serial group' that reflected the matching of putative serially homologous neurons across segments. A developmental 'hemilineage' was assigned to neurons with soma in the VNC. Neuron groups were then assigned 'systematicType' names based on connectivity and hemilineage identity for VNC intrinsic neurons, while DNs and MNs were separately assigned as explained in sections 2.2 and 2.3 (also see Figure 1E). If a neuron was previously identified in the literature, then its published name was defined as its 'type,' the primary name by which we refer to it in our analyses. Previously unidentified neurons retained their 'systematicType' as their 'type.' In addition, automated synapse prediction achieved synapse retrieval comparable to human annotation. Finally, neurotransmitter type was predicted for all MANC neurons using a convolutional neural network (Eckstein et al., 2020), trained using 187 neurons with identified neurotransmitter types as ground truth, to assign a probability that a given neuron utilized one of the three major fast-acting neurotransmitters: acetylcholine (ACh), GABA or glutamate (Glu). Thus, MANC reconstruction completeness and synapse prediction are sufficient to identify most major synaptic partners of all neurons, and allows quantitative analyses of VNC-wide connectivity.

2.2 Identification of descending neurons

To systematically annotate all DNs in MANC, we first seeded every profile in a transverse plane through the neck connective and proofread them to recognition of neuron type (AN, EA, SA, or DN). Types were distinguished based on the following criteria: ANs and EAs both have a soma in the VNC, but ANs have only one axon branch through the neck connective, whereas EAs may send multiple processes through the neck connective and also enter VNC nerves; SAs and DNs both lack VNC somata, but SA axons enter the VNC through a nerve, whereas DNs enter

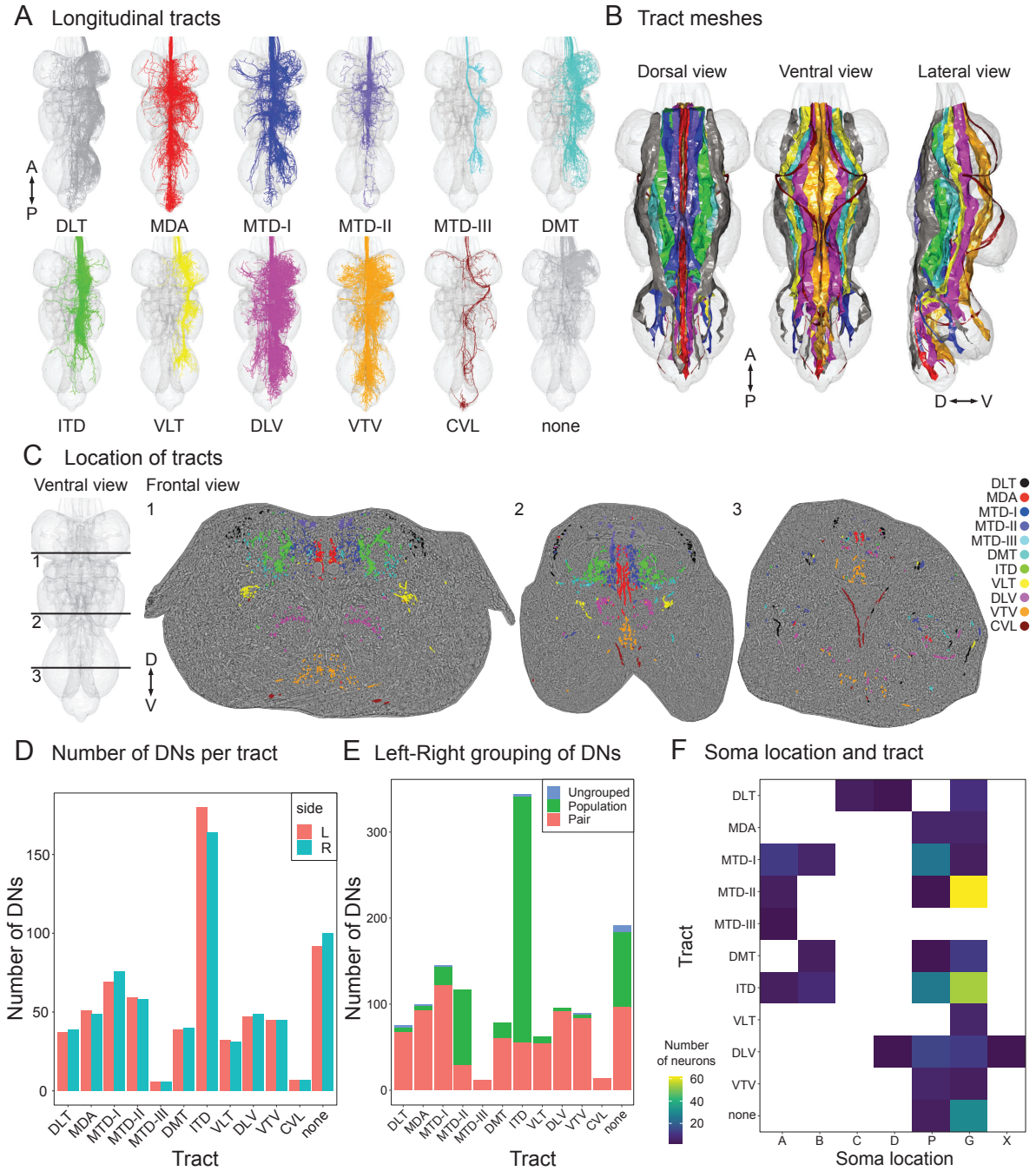

Figure 2: Tract based analysis of descending neurons. A. Tract analysis of all left hemisphere DNs (right hemisphere DNs are mirror symmetric). DNs run through different tracts in the VNC (Boerner and Duch, 2010; Court et al., 2020; Namiki et al., 2018). Tract names are based on previous publications: DLT, dorsal lateral tract of dorsal cervical fasciculus; MDA, median dorsal abdominal tract; MTD, median tract of dorsal cervical fasciculus; DMT, dorsal medial tract; ITD, intermediate tract of dorsal cervical fasciculus; VLT, ventral lateral tract; DLV, dorsal lateral tract of ventral cervical fasciculus; VTV, ventral median tract of ventral cervical fasciculus. We identified two previously unknown tracts: a third type of MTD and CVL, curved ventral lateral tract. DNs with a short primary neurite were not assigned to a tract in agreement with (Namiki et al., 2018). **B.** Tract meshes created from skeletons of DNs assigned to each tract respectively in dorsal, ventral and lateral view. Colors in **B** correspond to **A**. **C.** Cross section (frontal) view of all DN primary neurites color coded by their tract membership (DNs without tract membership were omitted for clarity). Position (1, 2, 3) of section in the VNC indicated by lines on the VNC ventral view. **D.** Number of DNs for each tract separated by cervical connective side. **E.** DNs were grouped based on morphology and connectivity. Groups can consist of one (pair) or more (population) DNs per hemisphere. DNs for which we could not identify a group were labeled 'ungrouped'. Shown are the compositions of DN grouping status separated by tract membership. **F.** Correlation of soma location and tract membership for identified DN types (based on light microscopy data, Namiki et al., 2018).

through the neck connective. In addition to the above types, we also identified four neck MNs running through the neck connective. Once identified, DNs were further annotated for the descending tract of their axon (Figure 1B, see below) and computer-vision-assigned neurotransmitter type (Figure 1C, see below).

As part of our focus on DN-to-MN pathways, we next proofread the DNs to higher completion in order to reach a greater coverage of presynaptic sites. To aid this process, we mapped all neurons from the left hand side of the dataset to the right using a mirroring registration and then carried out NBLAST morphological clustering (Bates et al., 2020). This procedure naturally grouped neurons into either left-and-right pairs or larger groups (populations) of neurons. This procedure provided a preliminary cell typing which was then used as the basis for comparing neurons with established light level data. We then manually matched DNs to light microscopy stacks (primarily from Namiki et al., 2018) showing expression patterns for genetic driver lines targeting single DN types (Figure 1D, Supplementary File 1). Matches were scored for confidence and only those with high scores were assigned the literature names as their 'type'. We were able to confidently identify matches for all but three types of published DNs (Figure 1-Supplement 1). This corresponds to 29% of all DNs (Figure 1D) in the EM dataset.

To provide spatial characterization of each DN, we identified their longitudinal tract and neuropil innervation. DNs run in tightly bundled tracts through the neck connective before diverging to target different VNC neuropils. Previous work described eight main tracts (Court et al., 2020; Merritt and Murphey, 1992; Namiki et al., 2018). To identify the tracts for DNs in the MANC dataset, we took the longest neurite of each DN and performed an NBLAST clustering (Costa et al., 2016). Clusters were then manually compared with published tract morphologies and rendered volumes (meshes from Court et al. 2020, Figure 2A-C). We found that the median tract of the dorsal cervical fasciculus (MTD), which was previously described as containing two subgroups (MTD-I and MTD-II), had an additional subgroup in our dataset, which we named MTD-III. We also found one of our NBLAST clusters that did not match any previously reported tracts. DN axons in this cluster were in a ventral lateral position within the VNC but did not align with the ventral lateral tract (VLT). We named this new tract the curved ventral lateral tract, CVL, after its very curved morphology. Both of these new tracts contain only a few DNs, which could explain their exclusion from previous light level studies (Figure 2D). In total, we were able to assign 85% of DNs in MANC to tracts. We used these to generate new tract volumes to be compared to future VNC datasets (Figure 2B). The ITD tract has by far the largest number of DNs and the highest proportion of population DNs (Figure 2D, E). MTD-II was the other identified tract that contained a high proportion of population DNs (Figure 2E). Neurons running in these two tracts have soma located in the GNG neuropil ('G') of the brain, as observed previously (Namiki et al., 2018)(Figure 2F).

We determined the target neuropil of all DNs by analyzing their synaptic output in the different neuropil areas of the VNC. The VNC is divided along the anterior-posterior axis into three thoracic neuromeres (T1-T3) and one fused abdominal neuromere (ANm), corresponding to the different segments of the fly body. Along the dorsal-ventral axis, the VNC divides into layers. The dorsal-most layer is the upper tectulum (UTct), which is composed of the neck (NTct), wing (WTct) and haltere (HTct) tectulums that contain motor neurons for those respective

appendages. The ventral-most neuropils are the leg neuropils (LegNp), which are composed of the front (LegNpT1), middle (LegNpT2) and hind leg neuropils (LegNpT3) that contain motor neurons for muscles of the leg in their respective segment. The ventral neuropils also include the sensory region mVAC. In between lie the intermediate tectulum (IntTct), lower tectulum (LTct), and the ovoid (Ov). If a DN had more than 80% of its output in a single neuropil, we designated that neuropil as the DN's target. If a DN had more than 80% of its output in two neuropils, with each contributing at least 5%, we assigned both neuropils as a target, annotated in the NeuPrint database as the two neuropil names separated by a full stop (e.g. IntTct.ANm). Neurons that had over 80% combined output to the three upper tectulum neuropils (neck, wing and haltere tectulum) or to the leg neuropils (LegNpT1, LegNpT2, LegNpT3), we assigned the layer label UTct or LegNp as a target, respectively (Figure 3A). Previous work suggested a correlation between a DN's tract and its target neuropil (Namiki et al., 2018). We see that this still holds loosely for the entire DN population analyzed at synaptic resolution (Figure 3B, Figure 3–Supplement 1C).

DN neurons were previously named following a convention that divided them into subclasses based on soma location in the brain (Namiki et al., 2018). We sought to systematically name the 376 newly identified DN types in MANC, but did not have soma location available to us to follow the published nomenclature. We therefore adopted a new systematic naming convention based on our annotation of a DN's VNC neuropil target. This system has the advantage of grouping DNs into subclasses of broadly similar function. Future work should unify these two naming conventions. All DNs annotated with a single target neuropil were given a two-letter subclass abbreviation corresponding to their target neuropil as follows: DNnt (neck tectulum), DNwt (wing tectulum), DNht (haltere tectulum), DNfl ("front leg," T1 leg neuropil), DNml ("middle leg," T2 leg neuropil), DNhl ("hind leg," T3 leg neuropil), DNit (intermediate tectulum), DNlt (lower tectulum), DNad (abdominal neuropil). In the 'systematic type' name, individual DN types were then further distinguished within their subclass by a three-digit number (e.g. 'DNnt001'). DNs that had more than one target neuropil were named according to the group of neuropils they targeted as follows: DNut (upper tectulum, including neck, wing, and haltere tectulums), DNxl (all leg neuropils), DNxn (broad targeting of many neuropils). For a further breakdown of DNxn types, see Figure 3–Supplement 1A, B.

These DN subclasses differ not only in the neuropils they target but also in the classes and subclasses of postsynaptic neurons to which they signal (Figure 3F). While all DNs primarily output to intrinsic neurons (IN), the largest VNC class, a high proportion of DNnt and DNad subclasses also output to motor neurons (MNs) in the neck and abdomen, respectively. Within the INs, there is a distinction between the DNs of the dorsal neuropils, which have a higher proportion of their output to bilateral interconnecting INs and DNs innervating the leg neuropils, which mostly target INs local to a single leg neuropil. There are small groups of DNs that strongly target some of the other classes of neurons in the VNC, such as efferent neurons or local sensory neurons (see Figure 3–Supplement 1D).

Knowing whether DNs are excitatory or inhibitory is critical for forming functional hypotheses about pathways in the connectome. Takemura et al. (2023) predicted ACh, GABA, or Glu neurotransmitter type for all MANC neurons using a trained convolutional neural network (Figure

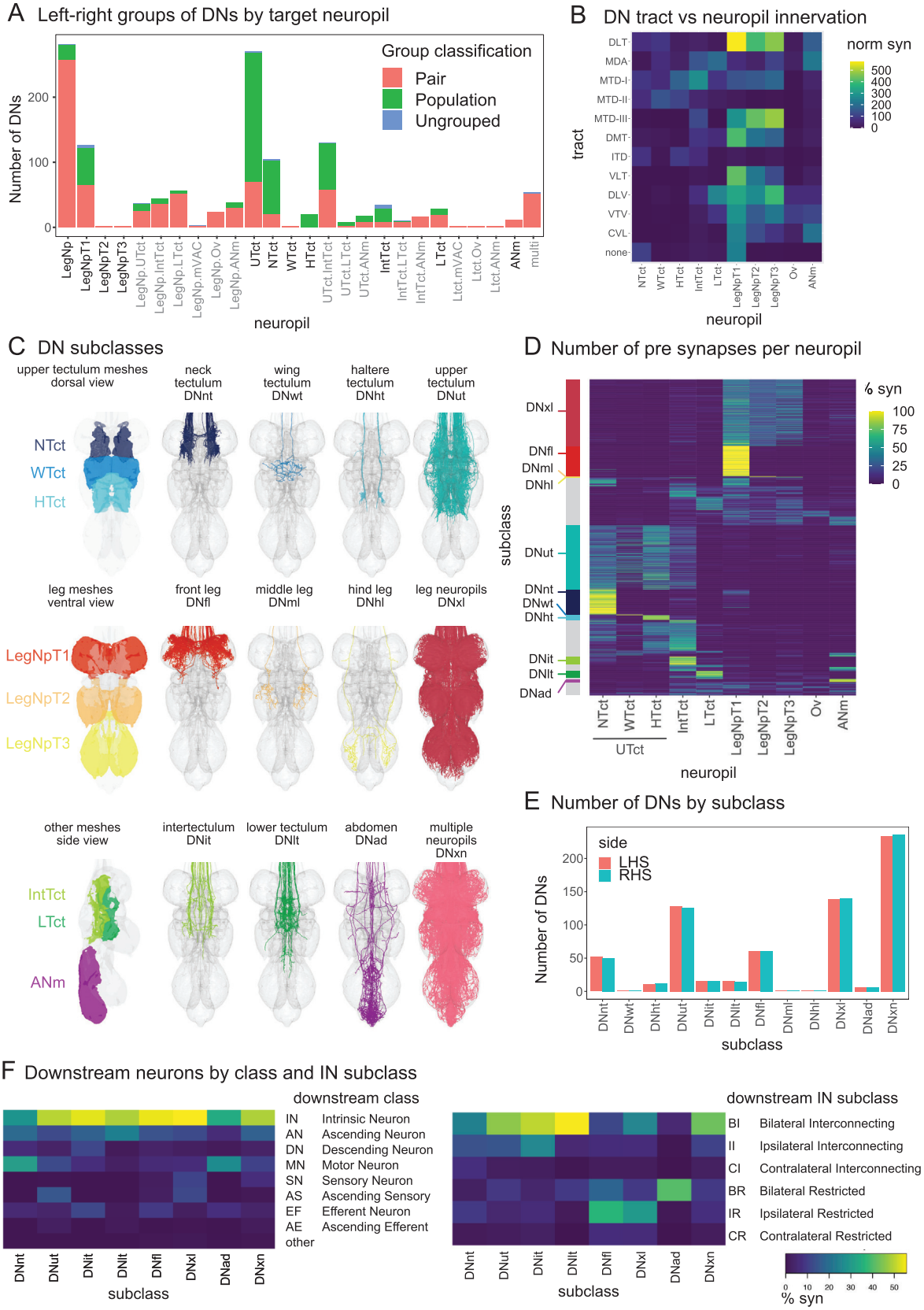

Figure 3: DN subclasses. *(cont.)*

Figure 3: *(cont.)* **A.** Descending neurons were analyzed based on neuropil innervation. X-axis indicates target neuropil designations (the ROI neuropils that together receive more than 80% of the DNs output, see Methods) and bar color DN grouping status (as in Figure 2). Target neuropil groups that were used to subsequently define DN subclasses are in black, all grey target neuropil groups received the subclass DNxn (see Figure 3–supplement 1). **B.** The relationship between neuropil location of DN presynaptic sites and tract membership. Total synapse number normalized by the number of DNs in the tract is shown. **C.** DNs are assigned a subclass based on their target neuropil: DNnt, Neck Tectulum; DNwt, Wing Tectulum; DNht, Halter Tectulum; DNut, upper tectulum, if they target a combination of neck, wing, and haltere neuropils; DNfl, DNml, DNhl, innervating single leg neuropils front leg, middle leg, and hind leg respectively; DNxl, if they target a combination of several leg neuropils; DNit, Intermediate Tectulum; DNlt, Lower Tectulum; DNad, Abdominal Neuromere. DNs that innervate more are referred to as DNxn, for multiple neuropils. **D.** Heatmap representation of DN neuropil innervation, by percent of each DN's synaptic output. Every row is a single DN output. Bar along the y-axis shows the subclass assigned to different DNs, grey are those in xn category (see Figure 3–supplement 1). **E.** The number of DNs in a given subclass assigned to either left or right side. There is a single pair of DNs for the subclasses DNwt, DNml and DNhl (see images in C). **F.** DN postsynaptic partner composition by neuron class and interneuron subclass.

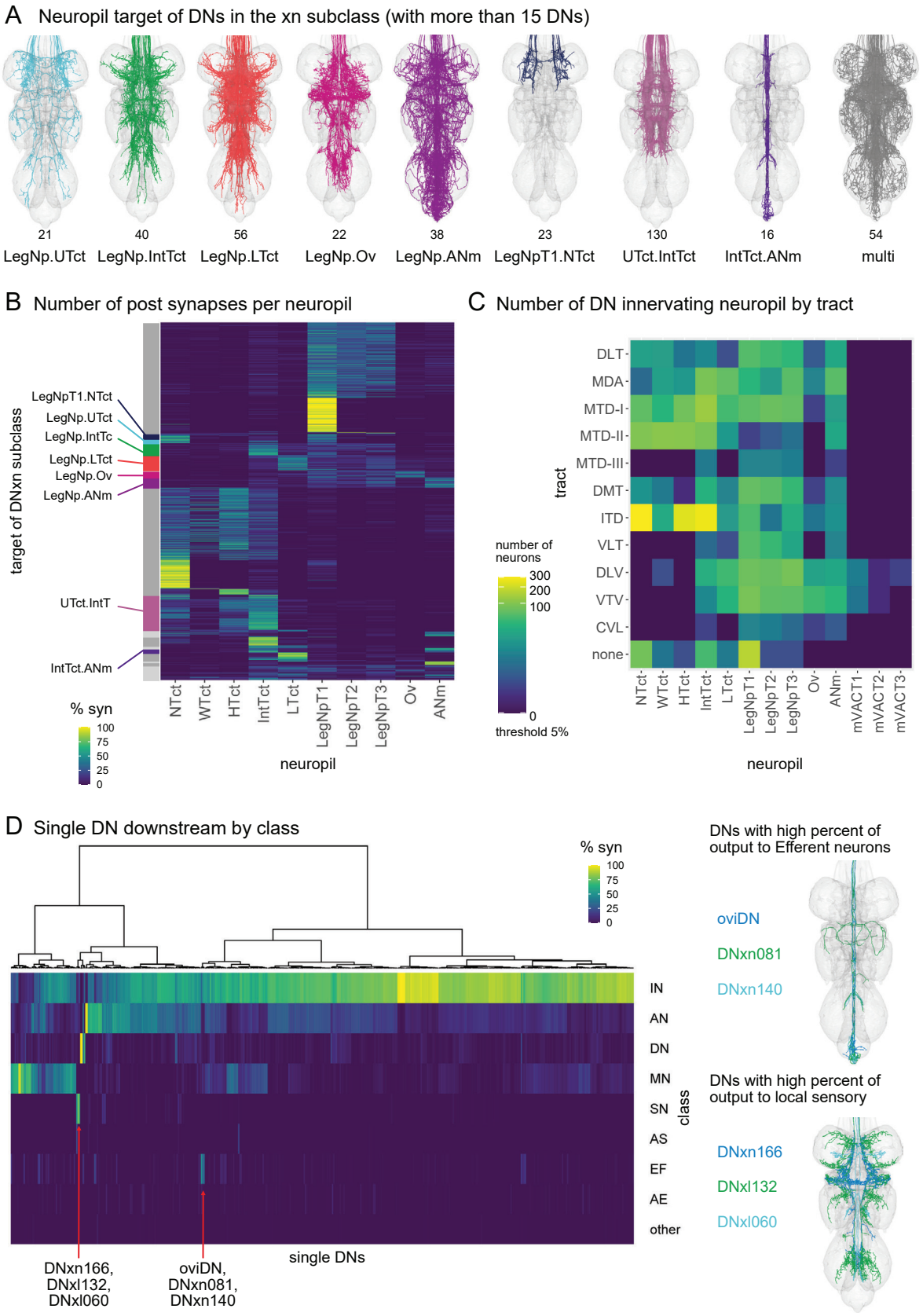

Figure 3—Supplement 1: DN subclass. A. DNs of subclass xn, which consisted of large groups (>15 single DNs) of DNs with common target distribution in the VNC. Number of single DNs within each xn subclass and names of combined target neuropils shown below each group. 'Multi' DNxns had 80% of the DN output in more than two neuropils. **B.** Heatmap representation of DN neuropil innervation by number of neurons. Every row is a single DN. Bar along the y-axis shows the neuropil targets (with >15 DNs) assigned to subclass DNxn, coloured only the ones shown in **A**. **C.** Number of DNs by tract innervating neuropils. Innervation in a neuropil is counted if the DN has more than 5% of its output to that neuropil. **D.** DN output to a neuron class in percent for every single DN, plotted on the x-axis. Red arrows point to two small groups of DNs, one with a high proportion of output to efferent neurons and the other with a high proportion of output to local sensory neurons.

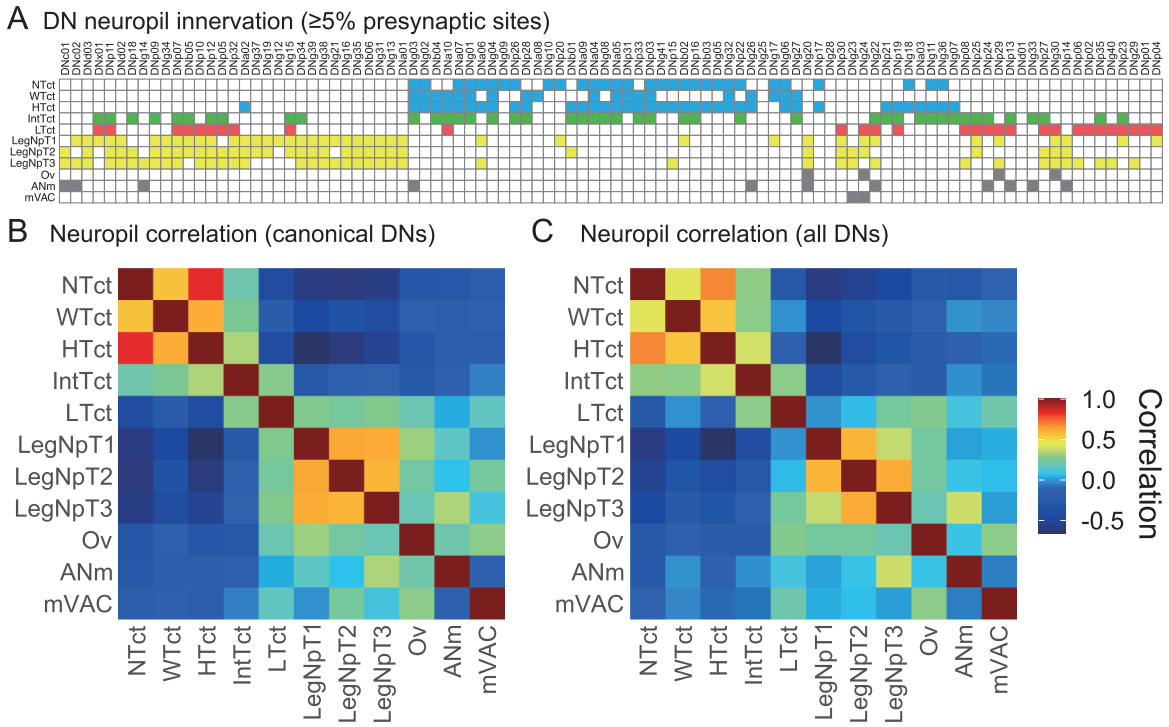

Figure 3—Supplement 2: ROI innervation for descending neuron types described in Namiki et al., 2018. A. Neuropil innervation of DN types. Filled pixels indicate that at least 5% of a DN group's presynaptic sites are located in a given ROI. X-axis order determined by Namiki at al., 2018, Figure 7. **B-C.** Autocorrelation matrix of DN innervation pattern in the VNC. The Pearson's correlation coefficient was calculated for each pair of ROIs between DN innervation of identified canonical Namiki types (**B**) and all types in the MANC EM volume (**C**).

4A-D). For DNs, neurotransmitter predictions appear associated with their ratio of output to input in the VNC– those with high neurotransmitter prediction confidence also have high output to input ratios (with a few outliers), while those with low confidence have a lower ratio (Figure 4E-G). However, the fidelity of DN neurotransmitter predictions is unclear, as they were not included within the initial training dataset. Also, the distribution of DN neurotransmitters predicted differed markedly from prior experimental results: EM prediction—68.4% cholinergic, 16.2% GABAergic, 7.5% glutamatergic and 7.9% other or below threshold (with a cutoff score of 0.7), co-labeling with neurotransmitter GAL4 lines—38% cholinergic, 37% GABAergic, and 6% glutamatergic DNs (Hsu and Bhandawat, 2016). These differences could be due to incorrect EM neurotransmitter prediction, but may also be due to incomplete or inaccurate labeling commonly-used neurotransmitter marker GAL4 lines, or due to underlying biological details (e.g. marker expression does not always equate to neurotransmitter usage). To evaluate the quality of the neurotransmitter predictions for the DNs, we selected a panel of 58 DN types for which we had a confident match between a MANC DN and a DN targeted in a split-GAL4 line. We used these to perform fluorescent in situ hybridization (FISH, Meissner et al., 2019) or Expansion-Assisted Iterative FISH (EASI-FISH) (Eddison, 2022; Wang et al., 2021) against the neurotransmitter markers *ChAT*, *Gad1* and *VGlut* that mark ACh, GABA and Glu, respectively. A subset of 15 DNs that either had low neurotransmitter prediction scores or were of interest were also probed for markers for the minor neurotransmitters octopamine, tyramine, serotonin, dopamine and histamine. We found 23 out of 28 cholinergic (additional 4 uncertain), 3 out of 9 GABAergic (additional 1 uncertain), and 9 out of 10 glutamatergic (additional 1 uncertain) predictions to be correct (Figure 4H, Figure 4–Supplement 1). Interestingly, we observed possible co-transmission of Glu and ACh for DNg27, DNg40, DNp08 and DNp49, possible co-transmission of Glu and tyramine for DNd02, and Glu (weakly expressing) with tyramine or octopamine in DNg34, which was a likely match for known octopaminergic DN aDT8/OA-VPM1 (Busch et al., 2009; Yu et al., 2010). Overall, neurotransmitter FISH results suggest that for DNs, ACh and Glu predictions are a good indication of actual neurotransmitter identity, whereas GABA predictions are still unverified. Thus, neurotransmitter predictions allow users a reasonable first guess at DN neurotransmitter identity but must be followed up with independent validation.

2.3 Identification of motor neurons

To identify the motor neurons (MNs), we first annotated all the nerves exiting the VNC (Figure 5A), and marked all neurons that passed through these. MNs were distinguished from the two other neuron classes that have profiles in the nerves by both having a soma in the VNC (which sensory afferents lack) and no profile in the neck connective (which efferent ascendings have). As with DNs, we carried out additional proofreading and categorization of all MNs of the VNC to obtain a higher degree of upstream completeness (Figure 5B). We note that, though the quality of the EM data underlying the MANC connectome was generally very high, some MNs, mainly of the leg neuropils but also several of the neck and halteres, showed signs of degeneration (dark cytoplasm and irregularly-shaped neurites) due to axonal damage during dissection. As a result, both morphology and connectivity for affected MNs was sparser than for non-affected MNs, and more processing of the EM data, both manually and with a second round of

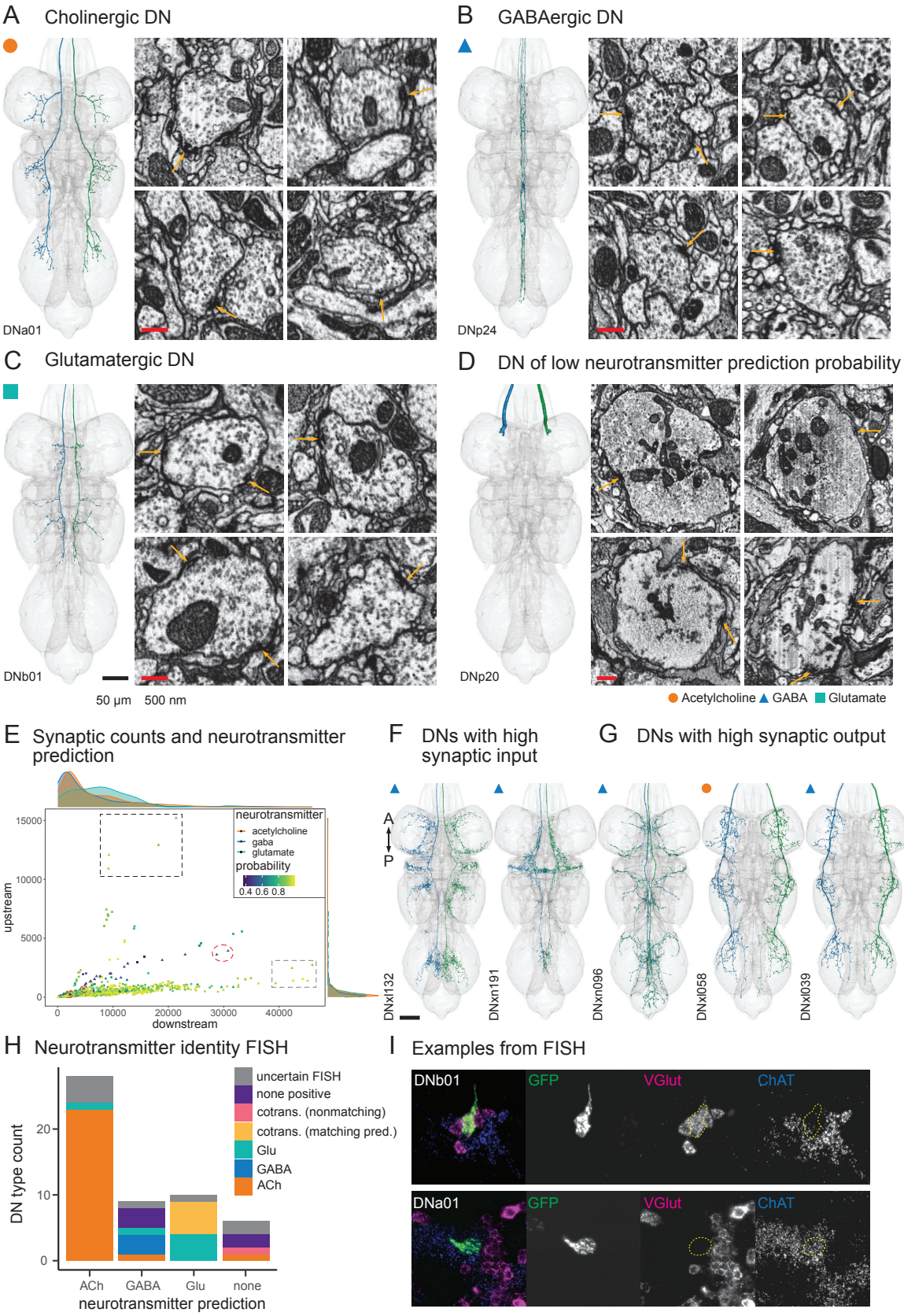

Figure 4: Neurotransmitter prediction for DNs. *(cont.)*

Figure 4: *(cont.)* **A-D** Morphology of example DNs with high probability neurotransmitter predictions for acetylcholine (**A**), GABA (**B**), glutamate (**C**) and very low probability neurotransmitter prediction (**D**). Four presynaptic sites in the EM volume are shown for each DN. Yellow arrows indicate the presynaptic density (T-bar) and synaptic cleft. Note, DNp20 (**D**) has few vesicles and might be electrically coupled to postsynaptic partners. **E.** Counts of pre- and postsynaptic sites of DNs and neurotransmitter predictions shown as shapes (acetylcholine, circle; GABA, triangle; glutamate, square). The prediction probability is color coded. Red circles indicate DNs shown in **D** and black rectangles indicate DNs shown in **F** and **G. F.** Morphology of two DN pairs with high synaptic input in the VNC. For both the predicted neurotransmitter is GABA. **G.** Morphology of three DN pairs with high synaptic output in the VNC, two of which were predicted to be GABAergic and one cholinergic. Black scale bars are 50 µm, red scale bars are 500 nm. Scale bars in EM synapse panels are the same if not indicated otherwise. **H.** Neurotransmitter identity for DNs based on FISH experiments, see Figure 4—supplement 1 for images and DN identities. **I.** Example images from the FISH analysis for DNb01 (SS02383) and DNa01 (SS00731). Dotted yellow line indicates the DN soma location (see Materials and Methods for details).

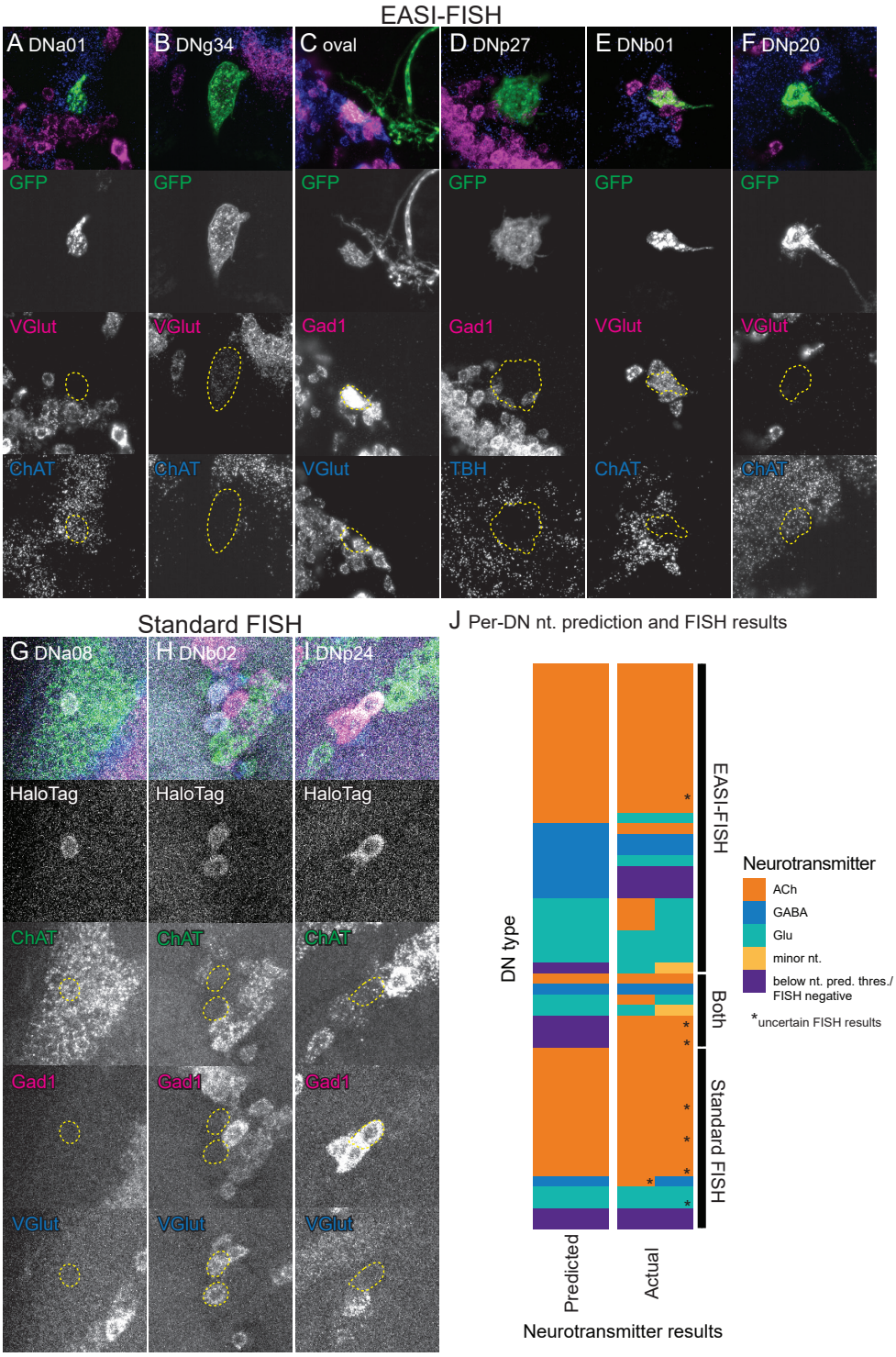

Figure 4—Supplement 1: DN FISH for neurotransmitter markers. To survey neurotransmitter usage in DNs, adult Drosophila brains expressing marker genes in individual DN types were probed using either EASI-FISH (Eddison, 2022; Wang et al., 2021) or a standardized FISH technique (Meissner et al., 2019). Example results for nine DNs are shown here. **A-F**. For EASI-FISH, brains of DN split-Gal4 lines crossed to UAS-CsChrimson-mVenus were probed for the indicated combinations of two neurotransmitter markers, as well as immunostained for GFP. Labeled DN types and their split-Gal4 lines are as follows: **A,** DNa01 (SS00731), **B,** DNg34 (SS58292), **C,** oval (SS93763), **D,** DNp27 (SS00923), **E,** DNb01 (SS02383), **F,** DNp20 (SS01078). **G-I.** For standard FISH, brains of DN split-Gal4 lines crossed to UAS-7xHaloTag::CAAX were probed for ChAT, Gad1 and VGlut, and stained with fluorescent conjugated HaloTag ligand. Labeled DN types and their split-Gal4 lines are as follows: **G,** DNa08 (SS02393), **H,** DNb02 (SS01060), **I,** DNp24 (SS00732). Soma of DNs of interest are outlined in all FISH channels. Maximum intensity projections in all images are from a Z-range in each stack that closely flanks the soma of interest. **J.** Summary of EM neurotransmitter prediction and FISH-determined actual neurotransmitter usage for all DN types tested (y-axis). Multiple colors per row in the actual neurotransmitter usage column indicates cotransmission. (*) indicates uncertain FISH results.

autosegmentation, for affected MNs was required (see Materials & Methods). Overall, we observed that most MNs have their inputs largely confined to a single neuropil, although some MNs arborize more widely (Figure 5C), corroborating light-level neuropil delineations and their likely functional specialization in motor control (Court et al., 2020). Together, MNs densely cover all neuropils except the predominantly sensory neuropils (Ov and mVACs) and the intermediate neuropils.

MNs were organized by morphology into 'groups' that consisted of left-right homologous pairs or populations using the same mirrored NBLAST analysis applied to the DNs (this paper and (Marin et al., 2023), together with exit nerve annotations and connectivity comparisons. In total, we found 737 MNs in MANC, with 362 exiting left side nerves, 362 exiting right side nerves, and 13 that exited through the abdominal trunk nerve (AbNT) near the midline (Figure 5B, E). These numbers were similar to those from the Female Adult Nerve Cord (FANC) dataset, where MNs traced (which excluded AbN2-4 and AbNT MNs) numbered 507—we found 513 for the MNs in the same nerves. We organized these into 321 groups and 14 singletons (that could not be paired). Similar to the DNs, we assigned both a 'type' and 'systematic type' to each MN group in the NeuPrint database. For the leg MNs, we additionally organized the groups into 'serial groups' of homologous neurons in the T1, T2 and T3 segments. All MNs were assigned a 'systematic type' by serial group, group or singleton cell (in descending order of priority), consisting of the 'MN' prefix, followed by a two-letter code denoting the muscle anatomical category they target (neck, nm; wing, wm; haltere, hm; front leg, fl; middle leg, ml; hind leg, hl; abdominal, ad; unknown, xm) and a two-digit number (Figure 5D, E, also see Figure 1E). For 'type' names, MNs were named by prior known names in the literature if identified, and by systematic type otherwise. Lastly, we annotated 'target' and 'subclass' fields for each MN, where target is the exact muscle target name if known, while subclass is their two-letter muscle anatomical category).

Each *Drosophila* MN is identified by the single muscle it innervates. However, the muscles were outside our dataset, which included only the VNC, so we could not directly observe this correspondence in our data. Instead, to match MANC MNs to their target muscles, we relied on matching the morphology of MN dendrites, which reside in the VNC volume, to images of known MNs in the literature. This was accomplished slightly differently for the different motor systems:

Wing and haltere MNs. To determine the target muscle for wing and haltere MNs, we matched the MN dendrite morphology in MANC to light microscopy image volumes of MNs with known muscle targets (Ehrhardt et al., 2023), or for three MNs identified their muscle targets in new or existing split-Gal4 lines (Sterne et al., 2021; Wu et al., 2016) (Figure 6–Supplement 1). These efforts allowed us to match all but one of the 26 MNs innervating wing muscles (Figure 6A, B). A single putative wing MN (MNwm36) with similar morphology to the ps1 MN remains unassigned to any muscle; Azevedo et al. (2022) hypothesizes that it innervates a pleurosternal muscle, likely contributing multiple innervation together with currently known pleurosternal MNs. To determine the MNs of the eight haltere muscles, we used light microscopy data from two papers describing haltere muscles and MN drivers in *Drosophila* (Dickerson et al., 2019; Ehrhardt et al., 2023) We identified seven pairs of haltere MNs, though three of these matches are putative (Figure 6C, D).

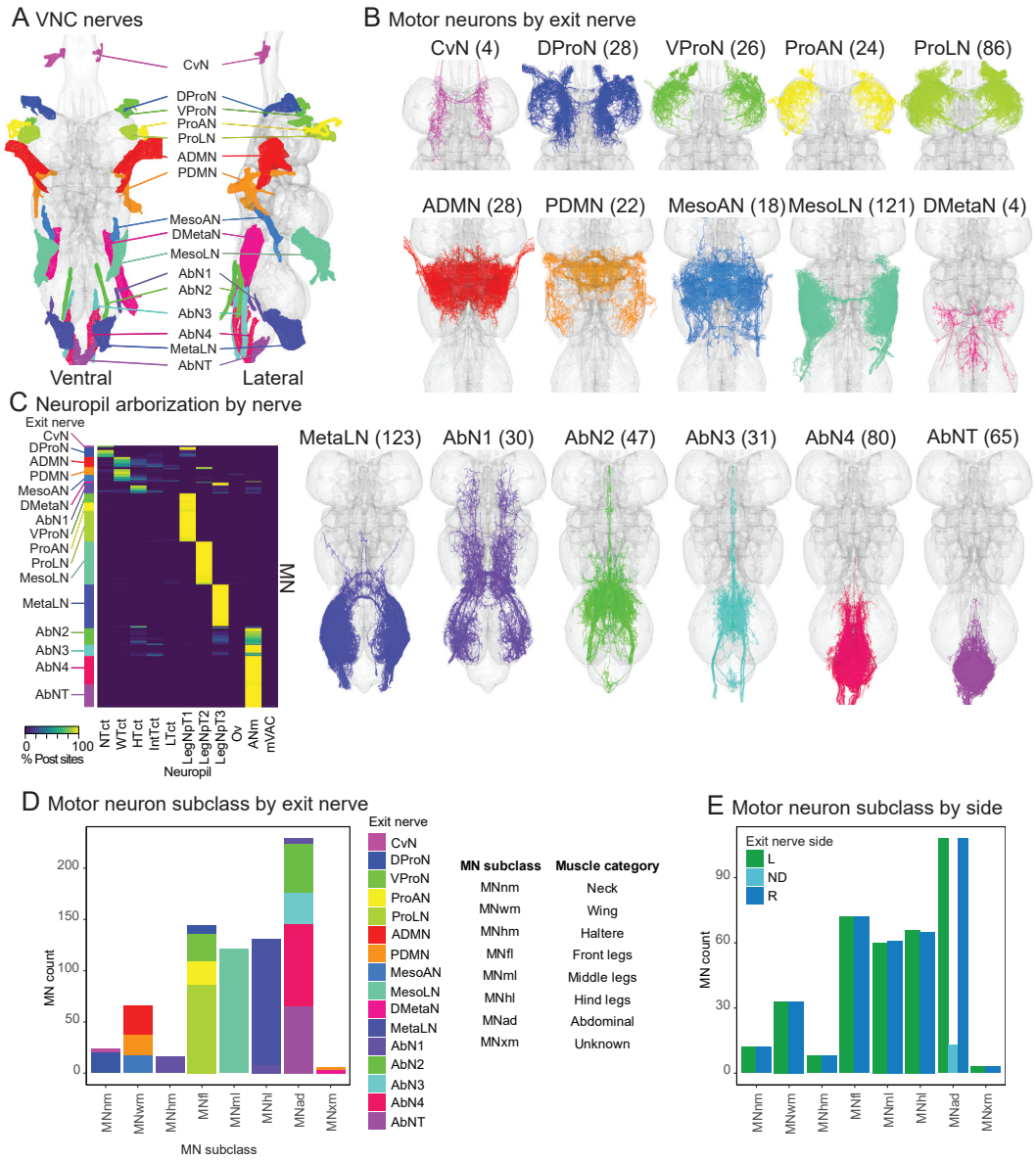

Figure 5: Motor neurons of the Drosophila male VNC. A. VNC nerves containing motor neurons (MNs). Nerve abbreviations are as follows: cervical nerve (CvN), dorsal prothoracic nerve (DProN), ventral prothoracic nerve (VProN), prothoracic accessory nerve (ProAN), prothoracic leg nerve (ProLN), anterior dorsal mesothoracic nerve (ADMN), posterior dorsal mesothoracic nerve (PDMN), mesothoracic accessory nerve (MesoAN), mesothoracic leg nerve (MesoLN), dorsal metathoracic nerve (DMetaN), metathoracic leg nerve (MetaLN), first abdominal nerve (AbN1), second abdominal nerve (AbN2), third abdominal nerve (AbN3), fourth abdominal nerve (AbN4), and abdominal nerve trunk (AbNT). **B.** All MNs found in MANC, classified by exit nerve. Number in parentheses indicates cell count. **C.** MN synaptic input by neuropil. **D.** MN subclass classification by broad anatomical muscle category, compared to exit nerve annotation. **E.** MN count per subclass by exit nerve side: left (L), right (R) or not determined (ND). Exit nerve side was not determined only for a subset of MNs exiting near the midline through the AbNT.

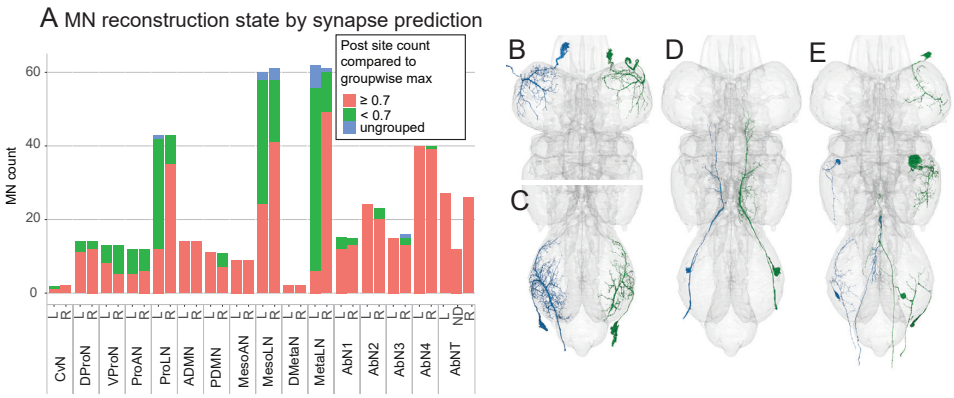

Figure 5—Supplement 1: Reconstruction state of motor neurons in MANC. A. Motor neurons (MNs) per nerve and side, classified by whether they have less than 70% (0.7) of the predicted postsynaptic site counts compared to their groupwise maximum, i.e. the postsynaptic count of the most well-traced member of each MN's morphological group in MANC. This classification flags MNs with likely reconstruction issues. Note that MN groups where all members of the group have reconstruction issues may not be flagged. **B-D.** Example MN groups with one well- and one less-well-reconstructed member: **B.** Sternal rotator anterior MN (group 13300), **C.** Ti extensor MN (group 10347), **D.** MNhm43 (group 17216). **E.** Seven examples (out of 14) of ungrouped MNs where their reconstruction state or that of their morphological match on the opposite side precluded group assignment.

Leg MNs. Less light microscopy data was available for leg MNs, so we used a different strategy, identifying leg MNs and their muscle targets in three main steps. We first examined light microscopy stacks for previously reported neurons (Enriquez et al., 2018) allowing us to assign several MNs of the T1 leg neuropil with relatively low confidences. We next transformed the T1 leg MNs from the Female Adult Nerve Cord (FANC) EM volume (Azevedo et al., 2022) to MANC space and performed an NBLAST comparison between MNs from the two VNC datasets (Costa et al., 2016). With expert visual evaluation, this allowed us to match up all FANC-identified T1 leg MNs to the MANC dataset (Figure 1D, Figure 7). To extend identification of leg MNs even further, we noted that the fly's three pairs of legs, and their muscles, exhibit a high degree of serial homology across segments (Miller, 1950; Soler et al., 2004) that is likely reflected in the morphology and connectivity of the leg MNs. As serially-repeating homologs of other neuron classes were identified across segments in MANC by (Marin et al., 2023), we leveraged this data to identify serial homologs of the T1 leg MNs in the T2 and T3 segments by comparison of MN connectivity with these serial homologs, as well as connectivity with neurons that span across several thoracic segments (mainly DNs, ANs and INs). Overall, in the MANC dataset, we find 396 leg MNs (144 in T1, 121 in T2, 131 in T3). We identified 142 of the 144 T1 MNs and, through serial matching, putatively identified 198 of the 252 leg MNs in the T2 and T3 segments (Figure 7). Thus, we were able to map leg muscle targets to most of the MNs in the three leg neuropils (Figure 7C).

We could not identify serially-repeating homologs (in T2 and T3) for the Tarsus levators and depressor MNs as well as the Tergopleural/Pleural promotor MNs (Figure 7D). For the tarsus targeting MNs, this was mainly due to their reconstruction state in T1 which made them hard to distinguish. For the Tergopleural/Pleural promotor MNs that innervate a muscle in the thorax, we could not find MNs in T2 and T3 that were similar in morphology and connectivity, suggesting that these MNs are either not present or have a different function and morphology (for unmatched leg MNs, see Figure 7–Supplement 1C,D). To compare the leg MNs across the serially repeated leg neuropils, we performed a cosine similarity of the upstream connections of serial MN sets to other serially repeated neurons that were restricted to the leg neuropils (see Marin et al., 2023, for details on restricted INs). The similarity within a muscle target and leg segment is generally consistent across the segments (Figure 7E). The inconsistencies seen in the T3 Tibia flexor and Acc. ti flexors are predominantly due to badly reconstructed and segmented MNs which resulted in a low synapse count.

Other MNs. For the remaining muscle categories (neck and abdominal), the *Drosophila* literature lacks detailed morphological descriptions and high-resolution LM data for their MNs, precluding identification of most MNs. For the neck MNs, light microscopy level identification of neck MNs are not yet available in *Drosophila*, although a comprehensive description of the neck muscle system and MNs is available in the blowfly, *Calliphora erythrocephala* (Strausfeld et al., 1987). In MANC, we identified 12 pairs of likely neck MNs (compared to 10 pairs in *Calliphora*) by their predominant presynaptic input in the NTct and exit through the dorsal prothoracic nerve (DProN). However, due to cross-species differences in MN morphology compared to *Calliphora*, as well as gross similarity between many neck MNs, only 3 of these MNs can be tentatively identified (Supplementary File 2). Abdominal MNs exiting through AbN2-4 and AbNT, while reconstructed and grouped, remain unidentified and will require future identification efforts.

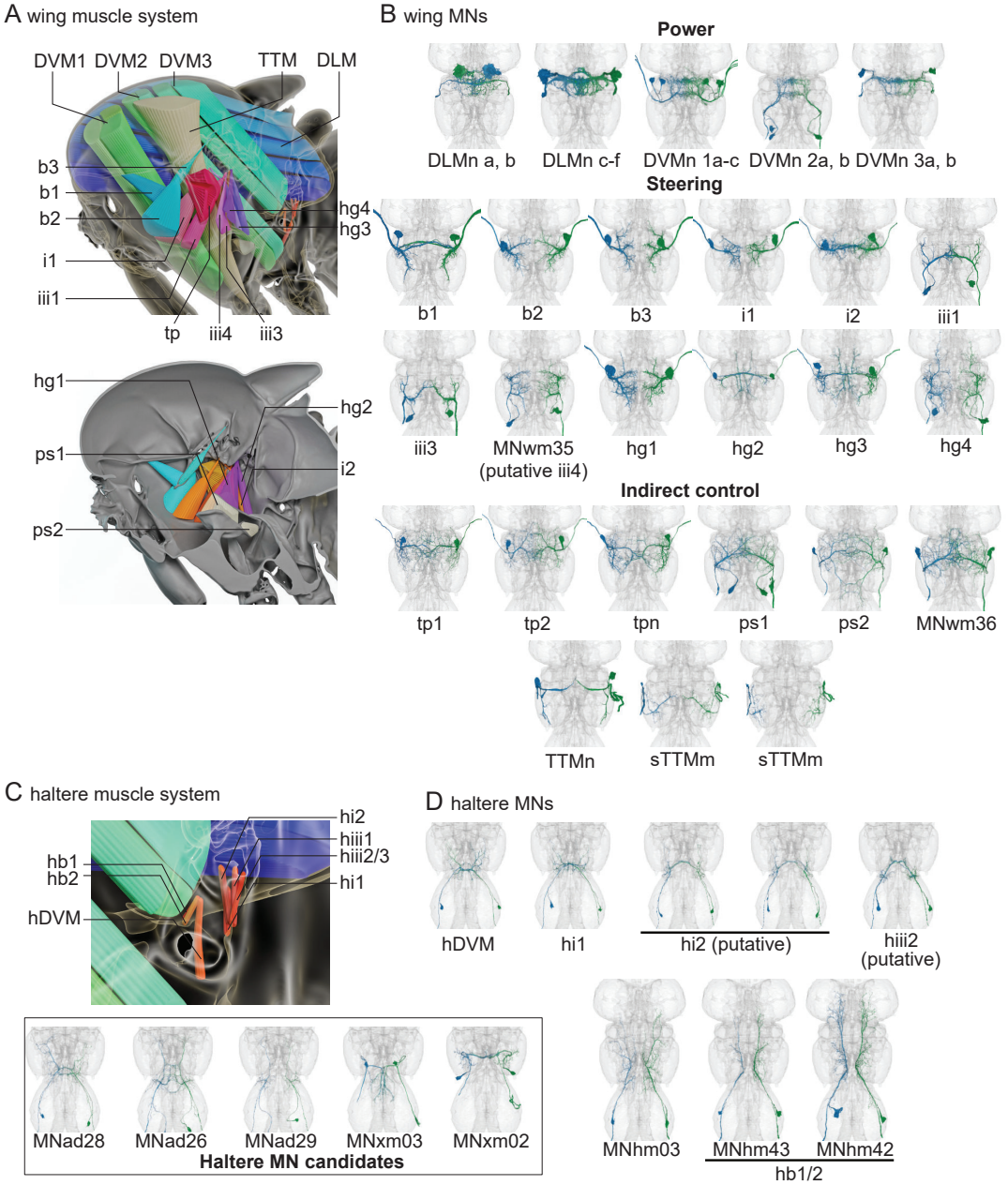

Figure 6: Upper tectular motor neuron identification in MANC. A. Thoracic organization of wing muscles shown from a lateral (top panel) or medial (bottom panel) view. Muscle categories and abbreviations are as follows: power muscles (dorsal longitudinal muscles, DLM; dorsal ventral muscles, DVM1-3), steering muscles (basalar, b1-3; first axillary, i1, i2; third axillary, iii1, iii3, iii4; fourth axillary, hg1-4), and indirect control muscles (tergopleural, tp; pleurosternal, ps1, ps2; tergotrochanteral, TTM). The hg2 muscle in the lateral view, and the power muscles and TTM in the medial view are omitted for clarity. **B.** Identification of wing muscle MNs from light-level data (see Supplementary File 2). The iii4 MN match (MNwm35) is putative, and the muscle target of MNwm36 is unknown. **C.** Organization of haltere muscles. Muscle categories and abbreviations are as follows: power muscle (haltere dorsal ventral muscle, hDVM), and steering muscles (haltere basalar, hb1, hb2; first axillary, hi1, hi2; third axillary, hiii1-3). **D.** Identification of haltere muscle MNs from light-level data. Two candidates for the hi2 MN with similar morphology and connectivity are present in MANC. MNhm43 and MNhm42 innervate the hb1 and hb2 muscles, however the exact target of each MN is not yet known. While additional putative haltere MNs are not easily determined in EM as both haltere MNs and abdominal MNs exit the AbN1 nerve, three potential haltere MNs are subsetted by their arborization in the haltere neuropil and exit through AbN1, and two potential haltere MNs by exit through the haltere nerve, DMetaN).

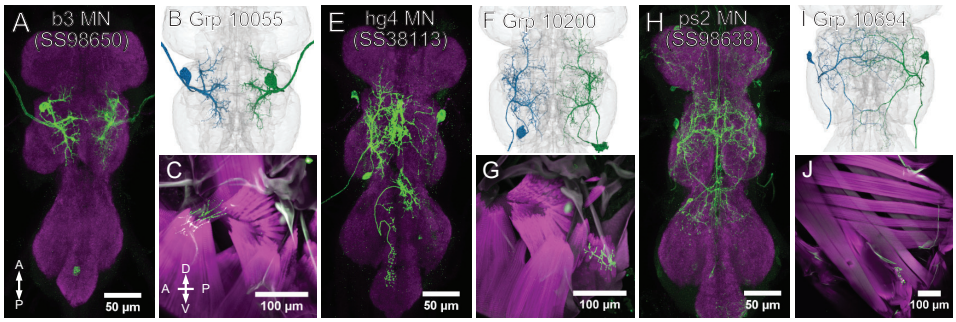

Figure 6—Supplement 1: Wing MN drivers and their muscle targets determined in this paper. A. VNC expression pattern (green) of the split-Gal4 line SS98650 (VT058382-AD; VT042734-DBD) compared to its MN match in EM (**B**). **C.** b3 muscle innervation (green) in a longitudinal section of the thorax in SS98650. **E.** VNC expression pattern of SS38113 (Sterne et al., 2021) compared to its MN match in EM (**F**). Expression in wing MN is stochastic in this line, and its muscle target was not previously identified. **G.** hg4 muscle innervation a longitudinal section of the thorax in SS38113. **H.** VNC expression pattern of SS98638 (VT026026-AD; VT064565-DBD) compared to its MN match in EM (**I**). **J.** ps2 muscle innervation in a longitudinal section of the thorax in SS98650. All VNCs are counterstained for mAb nc82 (magenta), while all muscles are counterstained with phalloidin (magenta).

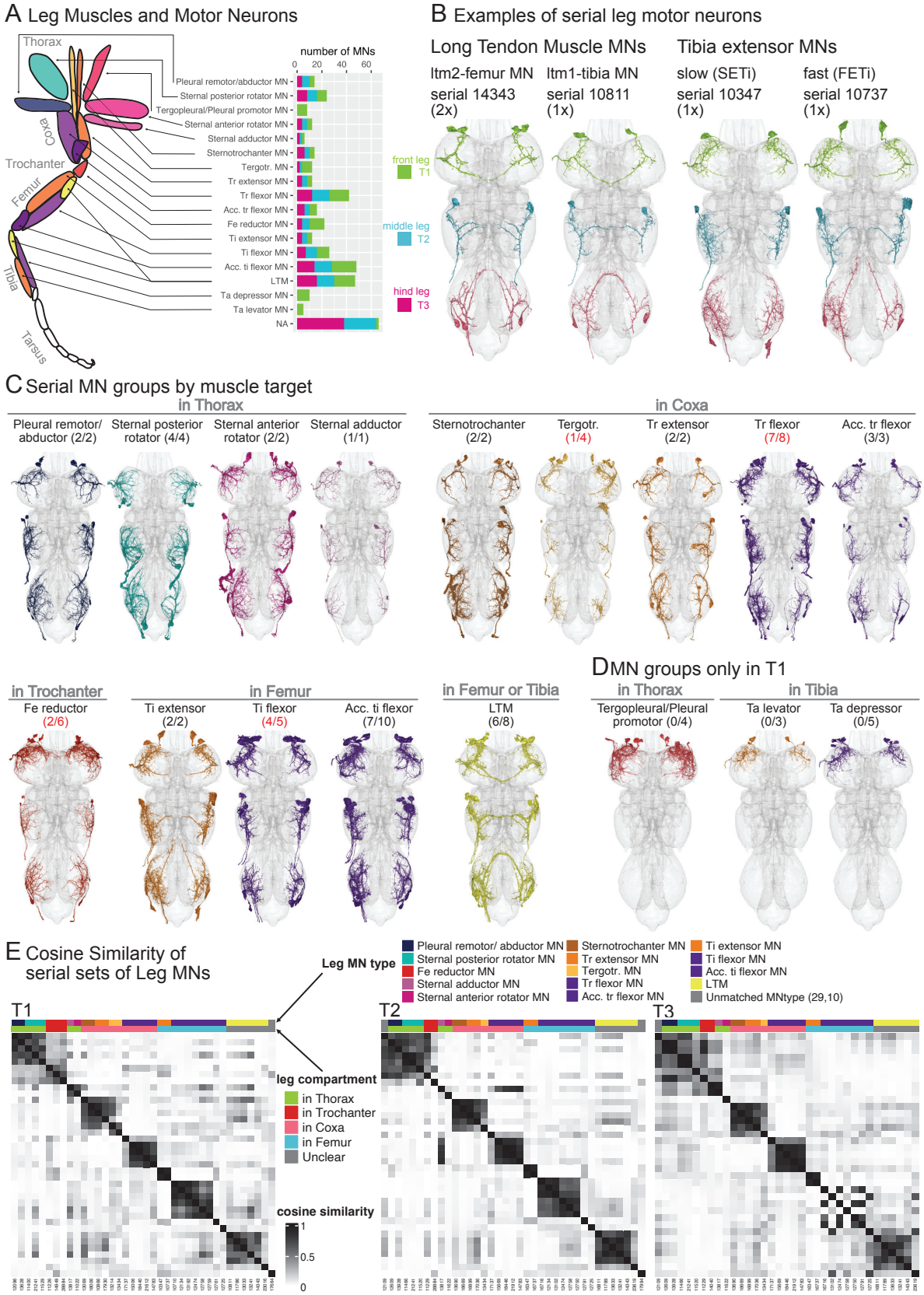

Figure 7: Serial leg motor neurons. *(cont.)*

Figure 7: *(cont.)* **A.** Diagram of a prothoracic leg showing the position of muscle groups innervated by motor neurons (MNs), some of which attach across the thorax, and others of which are intrinsic to the coxa, trochanter, femur, or tibia leg segments. Adapted from (Brierley et al., 2012). On the right the number of MNs that could be assigned a muscle target split into soma neuromere (T1, T2, T3). **B.** Example of two serial MN sets that innervate the long tendon muscles (LTM) and two serial MN sets that innervate the tibia extensor muscles, one for slow and one for fast tibia extension. **C.** All MNs that are in a serial set listed by their muscle target. In brackets the number of serial sets found / number of neurons in T1 pairs. Colors by the muscle they innervate as shown in the cartoon in A. **D.** For three of the muscle targets we were not able to find corresponding neurons in T2 and T3 leg neuropils. Thus only the T1 leg neuropils have muscle target assignments. **E.** Cosine similarity of all leg MNs by their connections to serial local neurons in T1, T2 and T3 leg neuropils. MNs are organized by muscle targets and leg compartment, shown in corresponding coloured bars. All MN targets in T1 were assigned by careful matching to the FANC dataset (Azevedo et al., 2022), while all MN targets in T2 and T3 were assigned by serial sets (see Materials and Methods).

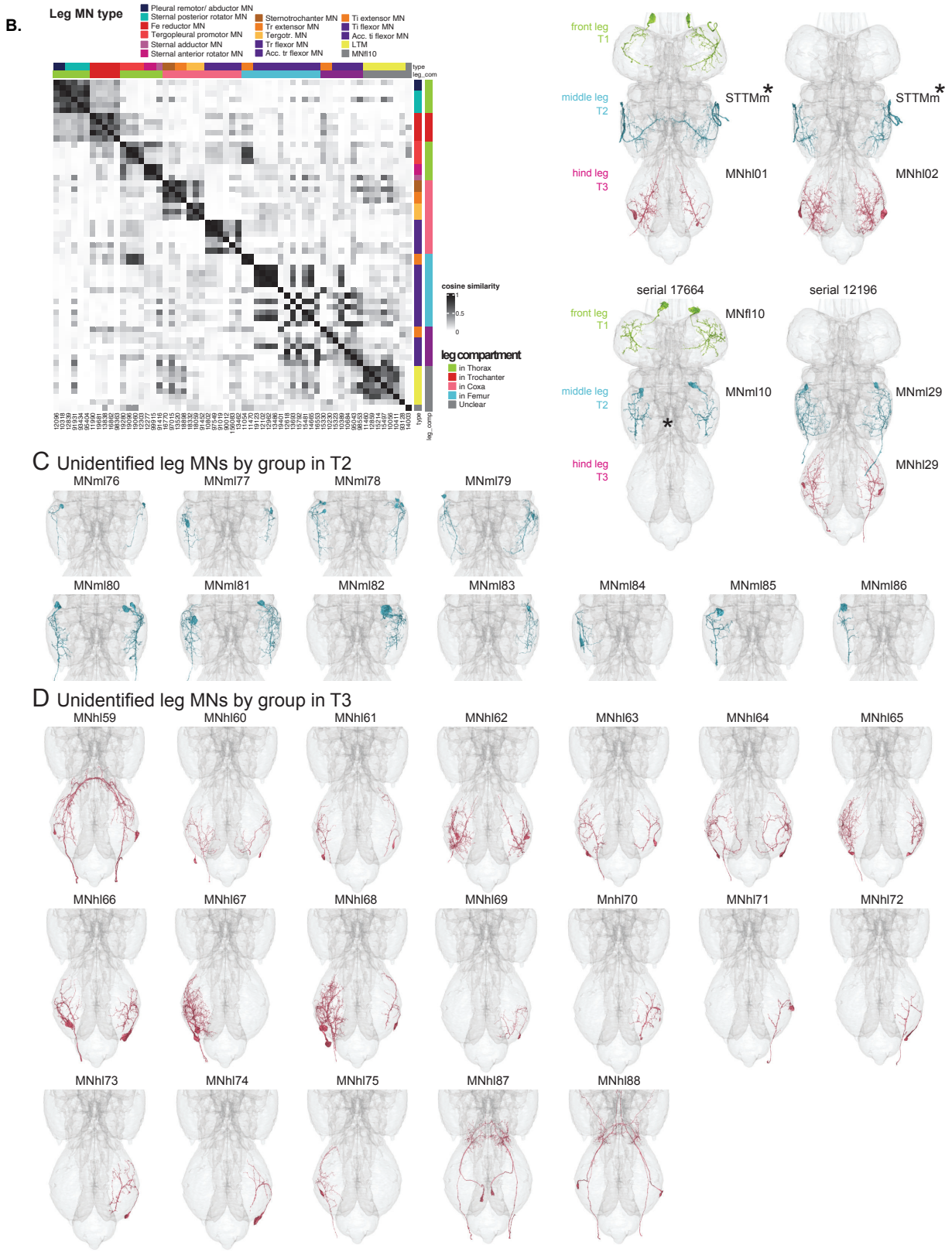

Figure 7—Supplement 1: Leg MNs not identified. A. Cosine similarity of all leg MN groups by their connections to serial local neurons in T1, T2 and T3 leg neuropils. MNs are organized by muscle targets and leg compartment, shown in corresponding coloured bars. All MN targets in T1 were assigned by careful matching to the FANC dataset (Azevedo et al., 2022, see Materials and Methods). **B.** Four serial MN sets that could not be assigned to the same muscle target across segments. The first two examples each include a T2 pair that has been matched to the literature type STTMm (marked with *). By connectivity and morphology they have a serial pair in T3 (and in T1 a MN assigned to the Tergotr. MN). **C.** All MNs by group in T2 that we were unable to assign a serial set. **D.** All MNs by group in T3 that we were unable to assign a serial set.

Overall, the 737 MANC MNs were categorized into 170 types, composed from 321 groups and 14 singletons. We were able to identify 169 out of the 321 MN groups by light-level, EM-to-EM or serial homology matching methods. All MN and efferents with their light microscopy matches and accompanying references are listed in Supplementary File 2. Together, these identifications cover the majority of wing, haltere, and leg MNs, as well as several neck MNs, thus laying the groundwork for connectomics analyses of these motor systems.

2.4 DN network analysis

2.4.1 DN to MN connectivity across the VNC

With the DN and MN populations fully identified and annotated, we were next able to examine large-scale organizational features of the networks that connect these inputs and outputs. We first asked whether DNs and MNs were found more commonly as individually-identifiable neurons (as left-right pairs) or as small populations that were difficult to distinguish by morphology or connectivity. The former is implicated in a more “command-like” form of motor control (von Philipsborn et al., 2011; von Reyn et al., 2014; Wang et al., 2020) and the latter in a more distributed representation (Dombrovski et al., 2023; Namiki et al., 2022). Using the terminal-based DN subclasses established in section 2.2, as well as the MN subclasses from section 2.3, we examined the pair versus population demographics across DN and MN categories (Figure 8A). Interestingly, a high proportion of population type DNs (~75-100%) were found among those DN subclasses that broadly innervate the upper tectulum (DNut), or specifically target the neck (DNnt) or haltere (DNht) tectulums within the UTct, as well as among DNs innervating the intermediate tectulum (IntTct). The remaining DN subclasses had higher proportions of pair types (~50-100%). Notably, a greater proportion of population DNs (~50%) are found in the DNs innervating only the T1 LegNp (DNfl) compared to those innervating all leg neuropils (~10%, DNxl).

Population-type DNs likely enable population coding of information across individual cell activity (van Hemmen and Schwartz, 2008), allowing finer-grained representation of information sent from the brain compared to pair-type DNs. The preponderance of these DN types in the UTct, IntTct and T1 LegNp thus likely points towards the need for higher precision muscle control in the associated neck, wing, haltere and T1 leg motor systems. Differences in potential control precision between VNC regions can be further illustrated by the ratio of DNs to MNs targeting each neuropil. For example: In leg neuropils there are 404 DNs:396 leg MNs by neuron count, a ratio of about 1:1. In contrast, in the upper tectulum there are 381 DNs:106 MNs, a ratio of close to 4:1. More DNs per MN could indicate finer control of MN action. The differences in pair versus population demographics between wing and leg DN inputs was not reflected at the level of MN outputs, where population types were fewer (<30%) and similar across wing and leg MNs (Figure 8A), indicating that a transformation of population-coded descending information into discrete muscle activation signals occurs in the premotor networks between DNs and MNs.

Next, we asked whether particular DNs or MNs were more closely connected with intrinsic neurons derived from specific developmental hemilineages, which are thought to define

functional units that make up VNC premotor networks associated with specific actions (Harris et al., 2015; Shepherd et al., 2019). The hemilineage identity of MANC intrinsic neurons was determined in Marin et al., (2023). We found that individual DN and MN subclasses have direct downstream and upstream partners, respectively, that are relatively hemilineage-restricted (Figure 8B), with high correspondence between the hemilineages connected to individual DN and MN subclasses that are expected to be functionally related. For example, both upper tectulum DNs (DNut) and wing MNs (MNwm) have significant connectivity with hemilineages 6A, 7B, 2A, 19B, 12A and 3B. We find that the hemilineage activation phenotypes documented in a previous optogenetic activation study (Harris et al., 2015) were largely consistent with expected broad motor roles of individual DN and MN categories (Figure 8B, bottom). A few notable exceptions are observed, such as the association of NTct, UTct and IntTct DNs, and neck, wing and haltere MNs, with hemilineages 6A and 6B, whose activation largely causes uncoordinated leg movements. These and similar hemilineages may be more associated with coordination of multiple motor circuits, e.g. both leg and wing circuits, thus complicating interpretations of hemilineage activation phenotypes. For hemilineages with no activation information, their connectivity with DN and MN subclasses allows a reasonable first guess at their motor function.

We next sought to identify which neurons were the strongest DN postsynaptic partners, with likely strong influence on VNC motor circuits. We plotted all neuron groups of the VNC (excluding DNs, MNs and sensory neurons) by the number of DN groups from which they receive input and the number of downstream intrinsic neuron groups they output to at a 1% synapse input threshold (Figure 8C). We color coded neuron groups by the neuropils they received ≥50% input from. Across the VNC, individual neuron groups received input from up to 23 DN groups and provide output to up to ~350 intrinsic neuron groups. Neuron groups categorized as IntTct or LTct received input from more DN groups on average (~5 groups) compared to intrinsic neurons from other regions (~1-2 groups). Neuron groups with a large amount of DN input and/or interneuron output (above the 90th percentile) are further plotted in Figure 8D. Notably, a subset of LTct neurons with high DN input and high output project widely in the VNC, and their role in LTct circuits are further followed up in section 2.7. The top targets of DNs in the UTct and ANm included several MNs, and we thus plotted direct DN input to MNs separately (Figure 8E, F) to examine what fraction of MN input comes directly from DNs. Most neck MNs, a subset of abdominal MNs, and several wing and haltere MNs receive >20% (up to ~60%) of their synaptic input directly from DNs, suggesting that they are under relatively direct control of DNs. Most other MNs receive a relatively low proportion of their input from DNs (MN groupwise mean of 7%), although ~80% of MN groups receive direct input from at least one DN group at a 1% groupwise input threshold, suggesting that control of most MNs derives from VNC intrinsic premotor circuits, but that direct input from brain signals via DNs still exerts some influence.

We have thus far been considering direct connections between DNs and their postsynaptic partners. To more broadly examine indirect connectivity from DNs to MNs, we next applied a Bayesian graph traversal model (based on Marin et al., 2023; Schlegel et al., 2021) to the MANC network. Starting from a set of seed neurons, the model traverses the neurons of the entire VNC and assigns a layer position to each cell by Bayesian probability, where the traversal

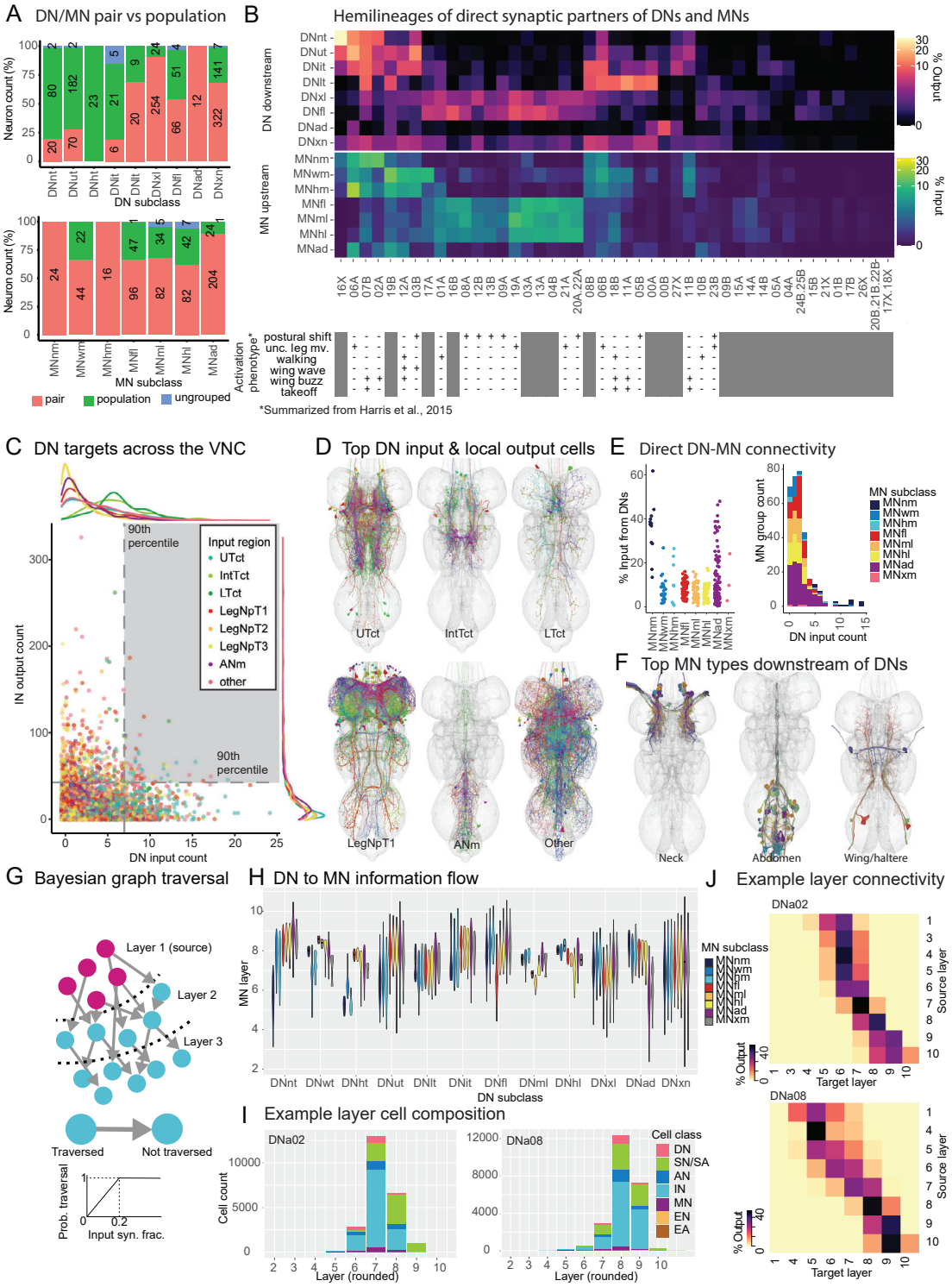

Figure 8: DN to MN connectivity across the VNC. A. Pair vs. population classification for all DN and MN types, by the number of cells per DN or MN morphological group. DN and MN subclasses are defined in Figures 3 and 5. The DN subclasses DNwt, DNml and DNhl, and the MN subclass MNxm are not shown as they consist of few cells (3 groups or less). **B.** Hemilineage composition of DN downstream and MN upstream partners, compared to hemilineage motor activation phenotype as summarized from (Harris et al., 2015). Motor phenotypes are marked "+" if ≥50% of flies display it upon hemilineage activation in Harris et al. (2015). **C.** All VNC intrinsic neuron groups (intrinsic, ascending, efferent and ascending efferent neurons) by their DN input count and local output count (Count of groups at a ≥1% groupwise input threshold). Intrinsic neuron groups are categorized by their primary input neuropil (≥50% postsynapses). **D.** Neuron groups with high DN input and local output (≥90th percentile for both) as defined in (**C**). **E.** Direct DN to MN connectivity, shown by input fraction per MN group contributed by DNs (left), and thresholded DN input count (≥1% groupwise input) per MN group (right). **F.** MNs with high DN input (≥20% total MN group input) from (**E**). **G.** Bayesian graph traversal model for assessing distance from individual DN groups (source layer) to all VNC neurons (target layer). All neurons are assigned a layer based on their synaptic connectivity with neurons in prior layers, where the probability of traversal is scaled by the input fraction contributed by neurons of prior layers. Thus, layer assignments are a nonlinear measure of distance combining path length and synapse connectivity strength. **H.** MN groupwise layer mean for all DN groups by Bayesian graph traversal runs starting with individual DN groups as the source layer. **I.** Example per-layer cell class composition of Bayesian graph traversal runs for DNa02 and DNa08. **J.** Example layer-to-layer connectivity of Bayesian graph traversal runs for DNa02 and DNa08, shown up to 10 layers. Layers without neurons are omitted.

probability for each node is determined by linearly scaling the input synapse connectivity between the node and all nodes of prior layers, up to a maximum of 20% (corresponding to a synapse input fraction of 1, Figure 8G). The layer position is thus a relative nonlinear measure of distance from the source neurons that quantitatively combines path length and synapse connectivity strength, although layer position assignments do not correspond directly to path length. We observed that DN subclasses generally have closer layer positions to MN subclasses that are putatively expected to receive control by those same neuropils. For example, the layer distance from haltere tectulum DNs (DNht) to MNs in the neck, wing, and haltere neuropils (MNnm, MNwm, MNhm) are about half the distance as that from DNht to leg MNs (MNfl, MNml, MNhl) (Figure 8H). In addition, MNs of the neck and abdominal subclasses have the lowest mean layer score from upstream DNs, suggesting that neck and abdominal MNs are more directly controlled by DNs than other MN subclasses, in agreement with our direct connectivity analysis (Figure 8E). This indicates that there is likely segregation of premotor circuits by function, e.g. flight, which requires control of neck, wings, and halteres together, that also corresponds to anatomical separation of the MNs by neuropil. Examples of layer cell class composition and layer-to-layer connectivity for two DN types (DNa02 and DNa08) are shown in Figure 8I, J. For both DNs, neuron layer assignment is relatively sparse and specific in initial layers–these cells are likely strong downstream partners of these DNs–while later layers (around layers 7-8) 'fan out' to reach most of the connectome. Layer-to-layer connectivity shows that each layer commonly has output to itself and the next layer, consistent with flow of information from one layer to the next. This trend is only noticeably different for the initial few layers and last 1-2 layers, possibly due to the paucity of cells assigned to those layers.

2.4.2 Community structure of VNC networks

Our analyses above indicate that, although some motor control is accomplished by direct connectivity of specifically-targeted DN terminals synapsing onto MNs for a particular limb, most paths from DNs to MNs are indirect, involving multiple layers of intrinsic neurons between DN and MN. To gain further insight into the structure of these intrinsic premotor circuits (here comprised of all cells except DNs, sensory inputs and MNs), we investigated whether connectivity in this network was uniform, or whether subsets of intrinsic neurons tended to synapse more strongly with each other, forming separable connectivity clusters, or communities. To quantify community structure, we applied a commonly used graph community detection method called the Infomap algorithm. Infomap is a community detection method that partitions a network's nodes by information flow, namely by minimizing the description length of the movements of a random walker within the network, as described by the map equation (Rosvall et al., 2009; Rosvall and Bergstrom, 2011, 2008; Smiljanić et al., 2021). We applied Infomap community detection to a directed graph of all VNC intrinsic neurons using synapse weights as edge weights. We used regularization using a Bayesian prior network to account for missing connections and multi-level clustering within the Infomap algorithm to allow splitting into nested communities; however, multi-level clustering showed that the two-level solution was optimal (i.e. splitting the VNC cells once into a non-nested set of communities).

The Infomap algorithm partitioned the VNC into 37 communities (Figure 9A) (excluding ~10 with no VNC synaptic input or output), of which 18 consist of 50 cells or more (Figure 9B, neuron community assignments in Supplementary File 3). The connectivity of these communities with each other are shown in Figure 9A, C. Labels for putative motor functions were assigned by community neuropil arborization (Figure 9D) and connectivity with DN and MN subclasses (Figure 9E, F). Notably, we observe one community per leg neuropil that largely corresponds to local leg networks, five communities covering the upper tectulum, and three in the ANm. We also observe three communities that each include neurons from multiple intermediate regions of the VNC and one in the mVACs, which all have low direct MN output. To probe the correspondence of Infomap communities with possible motor control functions, we further examined the connectivity of these communities with DNs and MNs by subclass (Figure 9E, F). Overall, most Infomap communities have relatively specific connectivity with DN and MN subclasses which suggests that each community may be a premotor network for a specific motor role. For example, communities 8, 9, and 10 receive input from upper tectulum DNs (DNut) and provide output to wing motor neurons (MNwm). Similarly, Communities 5 and 6 receive input from front leg DNs (DNfl) and output to front leg motor neurons (MNfl). Interestingly, in support of its hypothesized role in coordination of wing-leg behaviors, lower tectulum DNs (DNlt) target communities 7, 8, and 14—community 7 is notable as the largest VNC community (~1800 cells) and is the top non-self input to the majority of other communities (Figure 9C), and community 14 has no connectivity to MNs but itself outputs to communities labeled for both wing and leg functions. This raises the possibility that this community plays a key role in controlling or coordinating motor output across the VNC via control of other communities. Indeed, lower tectulum DNs that have been implicated in escape takeoff behavior (which requires leg-wing coordination) preferentially target this community, and are followed up on in section 2.7.

Our community analysis looked at the macrostructure of the VNC network, but what about the microstructure? Recurrent connectivity may plausibly play roles in local modulation of VNC circuits and generation of the patterned motor signals required for rhythmic motor actions. To probe the degree of recurrence present in VNC circuits, we quantified the proportion of all triad motifs in different neuropils of the intrinsic VNC network (Figure 9F). A neuron was defined to be within a neuropil if ≥50% of its input and output resided in the neuropil. For comparison, we performed the same triad motif analysis on brain regions from the Hemibrain connectome (Scheffer et al., 2020) with known high recurrence such as the mushroom body and central complex, or expected low recurrence such as the ventrolateral neuropils. We found that the entire VNC in general, as well as the UTct and all six leg neuropils have a lower proportion of cyclic triad motifs than the mushroom body and central complex, and comparable levels to the ventrolateral neuropils (Figure 9G), suggesting that VNC circuits generally operate in a more feedforward manner. Yet, the relatively small set of LTct-and IntTct-restricted cells have higher cyclic triad motifs at a similar frequency to the mushroom bodies and central complex, perhaps suggesting that neurons in these particular areas are higher order circuits that utilize recurrence to carry out more complex motor functions. LTct circuits are further discussed in section 2.7. These results are corroborated by a different analysis in which we looked at all-to-all neuron shortest cycle length (Figure 9H). This analysis showed that short-length recurrence occurs with

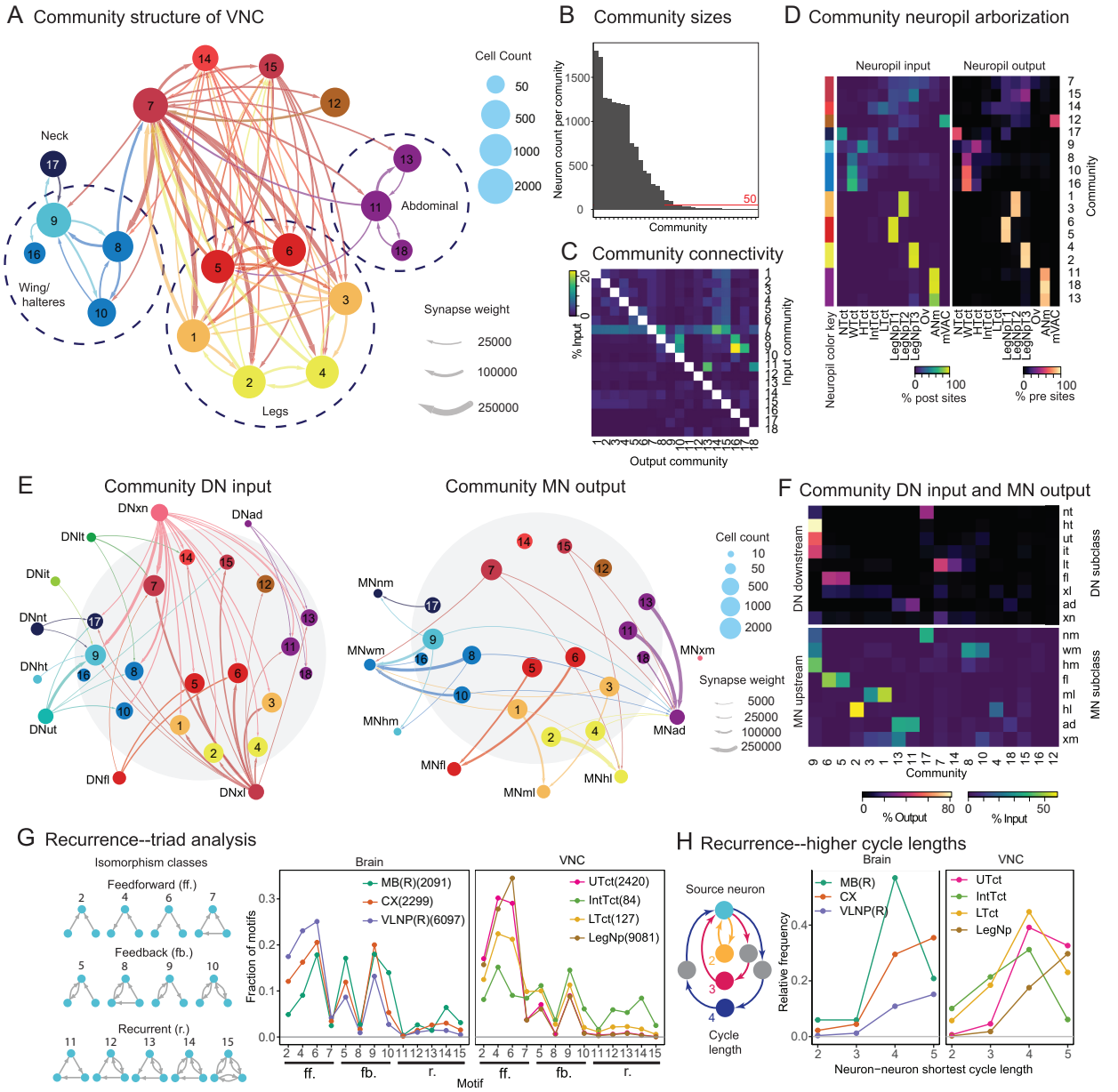

Figure 9: Structure of VNC networks. A. Community structure of VNC intrinsic neuron networks (all neurons excluding descending, sensory and motor) partitioned by the Infomap algorithm (Rosvall et al., 2009; Rosvall and Bergstrom, 2011, 2008; Smiljanić et al., 2021), a method which carries out graph community detection by information flow. Communities are numbered arbitrarily, and communities of at least 50 cells are shown on graph and colored by their constituent neurons' primary input and output neuropils (see C). Edges between communities are thresholded at ≥25000 synapses. Dotted circles and their labels indicate putative broad motor function based on neuropil arborization and connectivity with MN subclasses (see C & D). **B.** Neuron count of Infomap communities. Communities on x-axis are rank-ordered by their neuron count. Only communities with 50 or more cells are shown in (A, C-F). **C.** Infomap community-to-community connectivity. **D.** Community neuropil input and output, calculated by the % neuropil input and output of all neurons in the community. **E.** Community DN input and MN output by DN/MN subclass. Connectivity in graphs are thresholded at ≥5000 synapses. Light shaded area in graphs correspond to Infomap communities as shown in (A). The DN subclasses DNwt, DNml and DNhl consist of only a single DN group each and are not shown. **F.** Heatmaps of community DN input and MN output. **G.** Recurrence in VNC networks as evaluated by triad census, compared to brain neuropils with high recurrence (mushroom body, MB, and central complex, CX) and low recurrence (right ventrolateral neuropils, VLNP(R)). Triad motifs are classified by their isomorphism class into feedforward, feedback and recurrent categories. Synaptic connectivity between neurons are thresholded at ≥0.1% input. Neurons per neuropil are subsetted by having ≥50% input and output in the target neuropil, and further excluding DNs, sensory and MNs. **H.** Recurrence in VNC networks as evaluated by shortest cycle length between all combinations of neurons in a neuropil at a synapse threshold of ≥0.1% input. Neurons per neuropil are subsetted by having ≥50% input and output in the target neuropil, and further excluding DNs, sensory and MNs.

lower frequency in UTct and LegNp circuits and higher frequency in IntTct and LTct local circuits, at rates comparable to the mushroom body and central complex. Interestingly, LTct restricted neurons are included in the Infomap communities (e.g. 7 and 14) without direct links to MNs that we hypothesized to be higher level premotor circuits, whereas IntTct restricted neurons are largely part of community 9, which contributes to wing and haltere motor control. This suggests that similar microstructure of connectivity (i.e. recurrent motifs between individual neurons) may play different roles at different macrostructural levels of the network (lower vs. higher-level control of motor output)--recurrence may plausibly play roles in coordination or rhythmic control of wing and haltere muscles in the IntTct, and coordination of different motor systems or even computations determining behavioral output in the LTct.

In summary, DNs and MNs provide and receive input from their direct synaptic partners in a hemilineage-guided manner, with some MN subclasses (in particular neck and abdominal) receiving high direct input from DNs. By a Bayesian graph traversal model, we help define sets of DNs that target individual MN subclasses, as well as compare relative distances of MN subclasses from DNs. Community structure of VNC interneurons suggests that VNC premotor circuits are organized into communities that are each dedicated to control of specific MN subclasses, as well as several communities that have little direct MN control but instead have strong output to other communities, potentially for higher-order motor control. Finally, by analyses of recurrence, larger VNC regions like the UTct and all leg neuropils likely operate in a relatively feedforward manner, but the small circuits consisting of IntTct and LTct restricted cells instead have more recurrent motifs. This microstructure in these regions may aid in their respective motor roles, i.e. as effectors of motor output vs control and coordination of motor systems. In the following three sections we take a closer look at the microstructure of connectivity within different subcircuits of the VNC: the wing circuits contained in dorsal communities, the leg circuits, contained in ventral communities, and the potential higher order circuits of the intermediate neuropil.

2.5 Organizational logic of DNs onto wing circuits

2.5.1 Descending neurons and networks underlying wing motor control

In the fly, the wing motor system is crucial to behaviors such as flight (Dickinson and Tu, 1997), aggression (Kravitz and Fernandez, 2015; Zwarts et al., 2012) and courtship (Greenspan and Ferveur, 2000; Yamamoto and Koganezawa, 2013). The VNC houses premotor circuits that govern the control of the wing motor system and patterning of its motor output during these diverse behaviors (Harris et al., 2015; Yu et al., 2010). The MANC connectome allows us comprehensive access to their synaptic connectivity to begin dissecting the architecture of wing motor circuits and their control by descending signals. Here, we first broadly survey the direct and indirect connectivity of DNs to the wing MNs, and specifically focus on describing circuit connectivity and structure in relation to potential roles in flight. Wing control circuits in relation to courtship in MANC are discussed in detail in Lillvis et al. (2023).

As previously discussed, *Drosophila's* wing muscle system consists of three classes of muscle: the indirect power (PMs), steering (SMs) and indirect control muscles (ICMs) (Dickinson and Tu, 1997). The asynchronous PMs act to generate power for wing vibrations–the dorsal longitudinal muscles (DLMs) and dorsal ventral muscles (DVMs) function antagonistically, each taking turn to contract while stretch-activating the other to vibrate the thorax (Dickinson and Tu, 1997). These thoracic vibrations are thought to be transmitted to the wings through a clutch and gearbox mechanism formed by wing hinge elements, which functions to couple or isolate the wing from thoracic vibrations and further modulate wingbeat amplitude (Deora et al., 2015; Miyan et al., 1985; Miyan and Ewing, 1988; Nalbach, 1989). The wing hinge is in turn controlled by the relatively small SMs, which fire either tonically or phasically during flight in a manner phase-locked to the wingbeat cycle (Fayyazuddin and Dickinson, 1999, 1996; Trimarchi and Murphey, 1997) to accomplish steering (Deora et al., 2017; Dickinson and Tu, 1997) (also see Figure 6A). The mechanics of the wing hinge is complicated and a comprehensive model of how SMs control flight maneuvers remains elusive. However, activation patterns of SMs during turning in flight have been well-studied (seeTable 1). Lastly, the action of two of the three ICM categories–the pleurosternal (ps) and tergopleural (tp) muscles—are less well understood but are thought to function during flight to control thoracic stiffness and resonant properties, thereby indirectly modulating wingbeat amplitude (Dickinson and Tu, 1997). The tergotrochanteral muscle (TTM) functions in flight initiation during escape and is quiescent during flight (Dickinson and Tu, 1997), and thus its control is separately addressed in section 2.7.

To examine DNs that likely contribute to wing motor control, we first narrowed down DN types that provided a groupwise contribution of at least 10% and 100 presynaptic sites (raw count) to the WTct. The full set of WTct DNs is shown in Figure 10A, with example individual morphologies of several WTct DNs implicated in wing-related behaviors shown in Figure 10B and followed up on in the next sections. Of the WTct DNs, only a single pair of DNs (DNa08) has presynaptic sites restricted to only the WTct, while most other DNs that innervate the WTct also innervate the NTct and HTct (Figure 10C), suggesting that descending motor signals often simultaneously control neck, wing and haltere motor systems. Similarly, neurons that are directly downstream (≥1% groupwise input) of these DNs largely target the WTct and HTct, with smaller sets targeting other neuropils (Figure 10C). Both WTct DNs and their direct downstream cells target mainly intrinsic neurons (INs), with MNs being the next strongest targets (Figure 10C). To further probe the top targets of WTct DNs, we examined downstream interneuron targets of WTct DNs by the group-to-group number of 'strong' DN inputs (≥1% synaptic input and ≥50 raw synapse weight, groupwise) they receive, as well as the Infomap community assignments established in section 2.4 (Figure 10D). Indeed, the communities that receive the largest number of WTct DN input groups are expected to be associated with wing and haltere motor control–i.e. communities 8, 9, 10 and 16–with individual neuron groups receiving input from up to 11 DN groups (examples neurons with high DN input in Figure 10E). Next, to further examine finer details of community structure and their relation to DN input, we carried out a series of Infomap community detection using individual communities as input graphs and selecting an option to prefer modular solutions (as the two-level clustering from section 2.3 is the 'optimal' solution). This method divided up communities 8, 9 and 10 into further subcommunities (Figure 10F), and WTct DNs could be hierarchically clustered by their input to subcommunities to yield

five clusters. Wing-related communities appear specialized in their wing motor functions, with community 8 and 9 targeting steering MNs, community 10 targeting power MNs, and communities 8 and 10 further targeting indirect control MNs. The breakdown of subcommunity connectivity with wing and haltere MNs is shown in Figure 10–supplement 1.

Lastly, we sought to define at the DN type level the combinations of wing MNs and haltere MNs (also implicated in flight control) that each DN controls. To do this, we plotted direct connectivity from WTct DNs to MNs via groupwise input fractions, and indirect connectivity via a measure of indirect connectivity strength. Briefly, the metric of indirect connectivity strength (Li et al., 2020) is calculated by multiplying the input fractions for all cells forming a pathway between a source and target cell for a given path length, and summing them across all pathways of same length between source and target cells (accomplished by matrix multiplication of adjacency matrices). To compare indirect connectivity strength across multiple path lengths, the raw values per path length per source neuron are further normalized by their non-zero mean, and the largest normalized value among all path lengths (in practice up to 5) is taken as the indirect connectivity strength. For direct connectivity, roughly 30% of WTct DNs provide substantial (≥1% groupwise input) input to one or more wing or haltere MNs (Figure 10G), most commonly with single DN groups dedicated to steering MNs or a mixture of power MNs and indirect control MNs, although DNa08 is and exception that controls both the steering b3 MN and the power MNs. These trends are similar for indirect connectivity strength between WTct DNs and MNs (Figure 10H), with several DNs providing more widespread input across MN muscle categories. Thus, WTct DNs are generally specialized in the MN categories and intrinsic neuron communities they target, which begins to give us clues into their role in wing-related behaviors.

2.5.2 Laterized descending control of steering muscles mediated by the wing contralateral haltere interneurons

Flies are exceptionally nimble during flight, capable of executing aerial maneuvers involving minute wing kinematic changes (Dickinson and Muijres, 2016) to change their trajectory in the air. The steering muscles (SMs) are key to such maneuvers, and left-right asymmetric activation of up to nine of these muscles has been documented during flight turns (Figure 11A, Table 1). Prior work identified a DN (temporarily named AX) whose activity correlated with rapid, saccadic turning maneuvers in flight in response to visual motion and is thus a candidate command neuron for flight saccades(Schnell et al., 2017). While this DN's identity in MANC has yet to be determined, its rough morphology is similar to both DNa04 and DNa05, which are part of a set of DNs containing at least 5 other members with similar VNC morphology (see Figure 10B). Both DNa04 and DNa05 are cholinergic DNs that receive input from the posterior slope in the brain, an area implicated in wide-field motion responses, and DNa04 further receives input from the central complex which encodes fly heading direction (Hulse et al., 2021; Namiki et al., 2018). We thus set out to investigate the connectivity downstream of DNa04, DNa05 and similar DNs to determine their potential role in wing motor control and steering.

To examine MN control by these DNs, we first plotted their most direct pathways to wing and haltere MNs (Figure 11B). Indeed, multiple steering MNs are found downstream of these DNs, notably b1, b2, b3, i1 and iii3, as well as the hb1 and hb2 haltere MNs (MNhm42 and 43), which

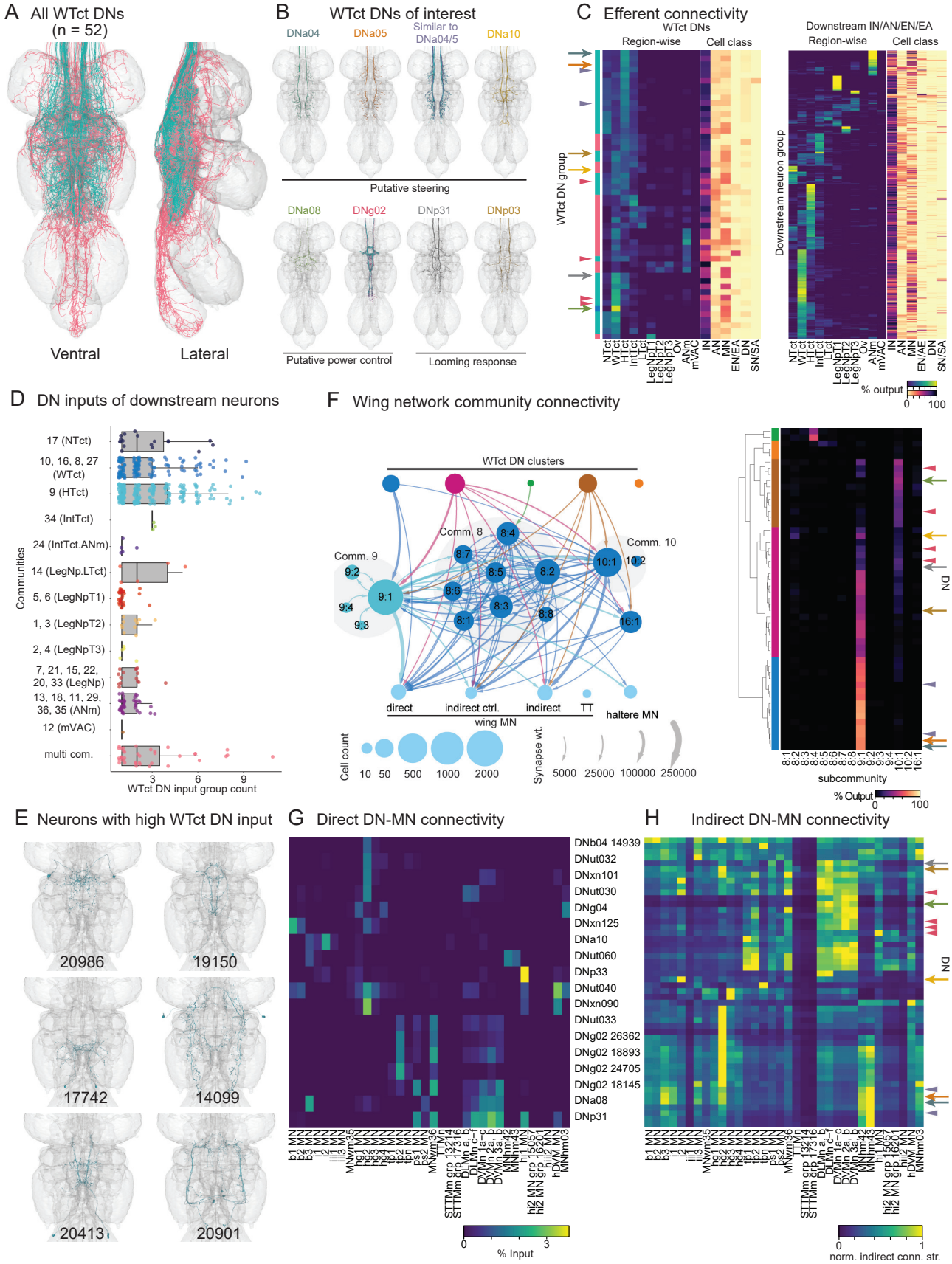

Figure 10: Overview of wing DNs and wing networks. A. DN groups with ≥10% output (groupwise mean) and ≥100 presynaptic sites (groupwise sum) in the wing tectulum (WTct). DNs are categorized and colored by their subclass as defined in Figure 3. **B.** WTct DNs of interest that may be implicated in flight motor control. **C.** Neuropil-wise and cell class-wise efferent connectivity of WTct DNs (left) and their direct downstream targets that receive ≥1% groupwise input from WTct DNs (right). In this and subsequent heatmaps, DNs of interest from (A) are shown with arrows (DN pairs) or arrowheads (DN populations) with same color as DN labels in (A). *(cont.)*

Figure 10: *(cont.)* **D.** DN input count (number of WTct DN groups providing ≥1% groupwise input) of WTct DN downstream intrinsic neuron groups (IN/AN/EN/EA), classified by top input/output neuropil of their VNC Infomap communities (see Figure 9). Groups in the "multi com." category have individual neurons assigned to different communities. **E.** Example morphologies of top WTct DN target groups from (C). **F.** Community structure of wing-related Infomap communities and their connectivity with WTct DNs and wing/haltere MNs. Subcommunities were defined by a second round of Infomap community detection on cells of each community. DN grouping is defined by hierarchical clustering of individual WTct DN groups' output to subcommunities (right heatmap). Edges on graph are thresholded at ≥2000 synapses. **G.** Direct connectivity from WTct DNs to wing and haltere MNs. DN groups shown have ≥1% input to at least 1 MN group. **H.** Indirect WTct DN-MN connectivity by normalized indirect connectivity strength (see materials and methods). DN groups shown have ≥5 normalized indirect connectivity strength values to a MN group. Normalized indirect connectivity strength is then rescaled to a maximum of 1 row-wise (DN groupwise).

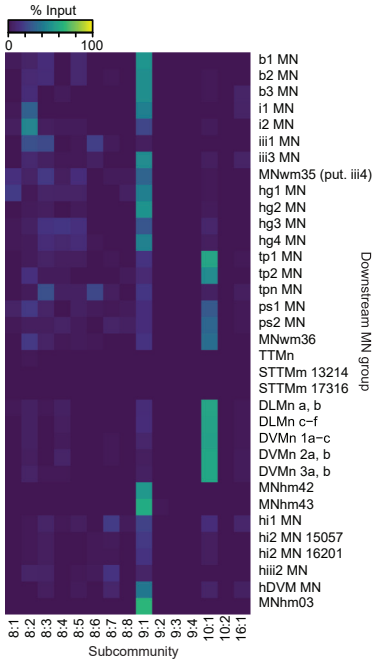

Figure 10—Supplement 1: Connectivity of wing network Infomap subcommunities to MNs. Synaptic input fractions contributed by individual subcommunities to wing and haltere MNs of a group.

are the haltere homologs of the basalar wing MNs. Despite similar VNC morphology, notable differences are observed in connectivity between these DNs–they may roughly be split into two sets, namely one (DNa04, DNa05, DNut037, DNut038, DNut060) with direct connectivity to wing contralateral haltere interneurons (w-cHINs, morphology recognized from Trimarchi and Murphey, 1997), and one (DNa09, DNxn123) with no connectivity to w-cHINs but that have greater connectivity to haltere MNs, which may indirectly affect steering (Dickerson et al., 2019).

The w-cHINs are excellent candidates as intermediaries for DNs to carry out steering during flight, as they have been documented to contribute lateralized electrical input to at least the b1 MN (Trimarchi and Murphey, 1997). Thus, we further looked into their connectivity and possible functions in wing motor control. In MANC, we observe five groups of large w-cHINs consisting of 14 cell pairs, all of which receive substantial DN input (also see Figure 11H). Visual examination in the EM volume indicates physical contact between the w-cHINs and several MNs, suggesting that the five w-cHIN groups may each provide electrical synaptic input to distinct sets of MNs. Electrical synapses are too small to be resolved using our current EM method. However, where they occur the cell membranes of the two cells they connect run in close parallel contact to each other. Thus to unbiasedly evaluate physical contact of w-cHINs with wing MNs to form hypotheses for putative electrical connections, we retrieved EM-derived 3D models of the w-cHINs and all wing MNs and quantified the area of contact between w-cHINs and steering MNs (Figure 11C, D). This method suggests that two w-cHIN groups may have electrical connectivity with the b1 MN, two groups may have electrical connectivity with both the b1 and b2 MNs, and one group may have electrical connectivity with the iii3 MN. In all cases, the w-cHINs connect to contralateral steering MNs (relative to w-cHIN dendrites), insert at the base of the MN dendritic tree, and are thus highly suited to drive steering MN activity while bypassing the MN dendritic integration process (Figure 11D).

How might DNs use w-cHINs and their synaptic partners for steering? To examine this, we looked at the example of DNa04. We plotted the ipsilateral and contralateral pathways of DNa04 to steering MNs through w-cHINs and other cells (Figure 11E, also see Figure 1G). Assuming that w-cHIN electrical connectivity is excitatory, upon activation of a DNa04 cell on one side, we would expect that w-cHINs will mediate a contralateral increase in activity in the b1, b2 and iii3 MNs. At the same time, we expect an ipsilateral increase in b3 and i1 MN activity through direct DNa04 input, as well as disinhibition of the same MNs via a two-synaptic hop connection through two putative GABAergic INs. Separately, the contralateral b3 and i1 MNs are expected to be inhibited through two paths involving 3 INs. All in all, the pattern of ipsilateral-contralateral MN activation suggests an effect of turning towards the ipsilateral side of DNa04 activation, although not all steering MNs associated with turning are in this pathway (notably hg MNs do not receive substantial input from DNa04, at least at shorter path lengths). Thus, DNa04 is indeed likely to play a steering role during flight.

In investigating the connectivity of w-cHINs, we also observed substantial chemical synaptic input to all w-cHINs from haltere campaniform sensilla as well as lesser input from wing base campaniform sensilla, corroborating connectivity previously identified in the literature (Dickerson, 2020; Trimarchi and Murphey, 1997) (Figure 11F). During flight, haltere campaniform sensilla send oscillatory signals that encode the inertial forces acting on the

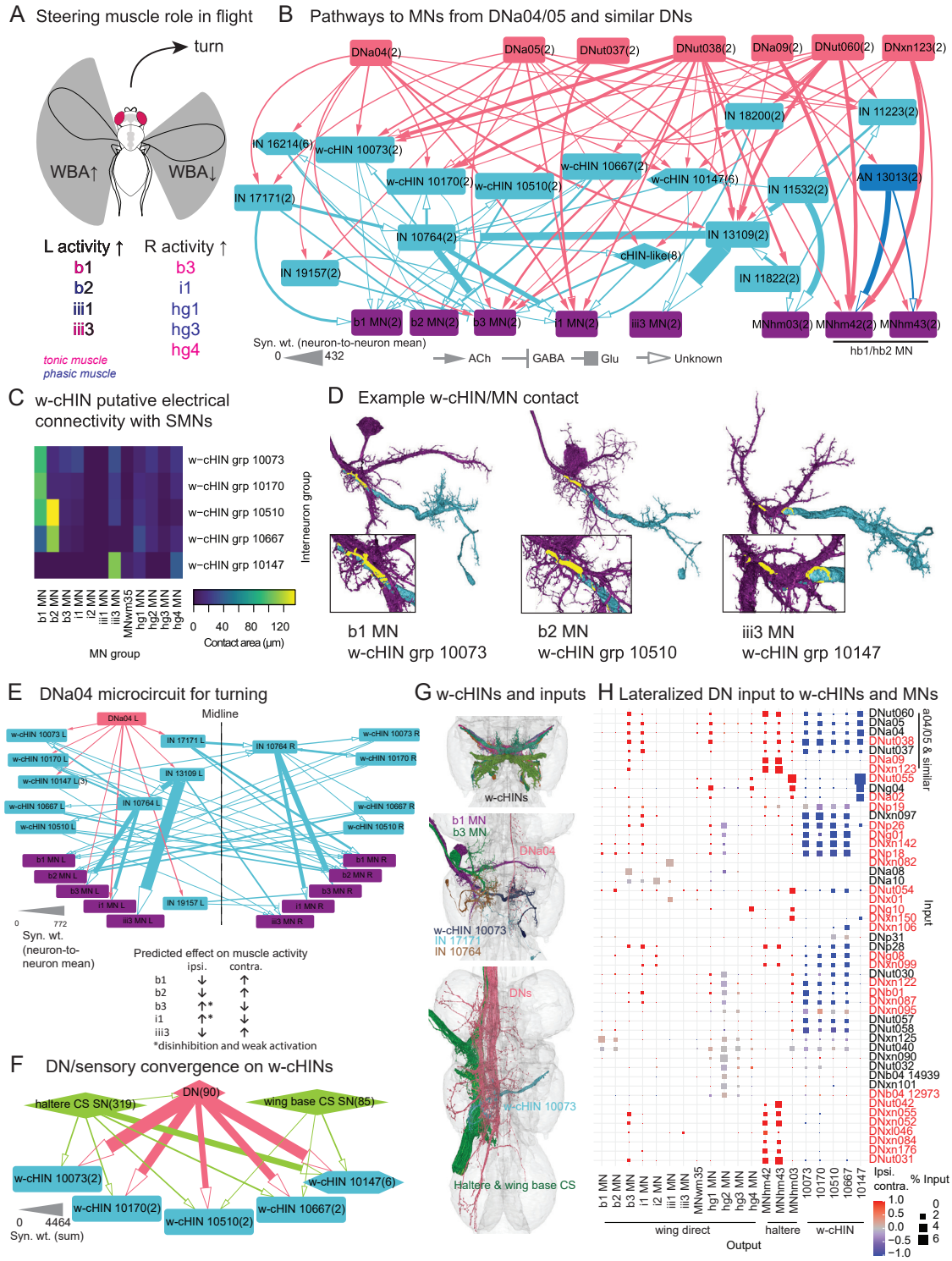

Figure 11: Putative flight steering circuits through DNa04/05 and w-cHINs. A. Modulation of fly wingbeat amplitude (WBA) and steering muscle (SM) activity during turning in flight. SM activity is simplified from Lindsay et al., 2017 (also see Table 1). **B.** Pathways of DNa04, DNa05 and other DNs with similar VNC morphology to steering MNs (SMNs) and haltere MNs. Five- or 6-digit number (if shown) indicates group annotation, while number in parentheses indicates cell count per node. Synapse weight (neuron-to-neuron mean) is thresholded at ≥20, except for connectivity of wing contralateral haltere interneurons (w-cHINs) to MNs which may involve electrical synapses (see C). **C.** Mean surface contact area of single w-cHINs of a group to all MNs of a group, suggestive of electrical synaptic connectivity. Contact area is calculated using 3D neuron meshes derived from EM segmentation; for each MN/w-cHIN pair, meshes are expanded by 0.1 µm, and the intersection surface area is calculated. **D.** Examples of w-cHIN contact with MNs, with intersection area(yellow) shown through the neuron meshes. *(cont.)*

Figure 11: *(cont.)* **E.** Lateralized pathway from DNa04 to steering MNs through w-cHINs and associated cells as a candidate steering microcircuit, and predicted effect on steering MN lateralized control. For clarity, the right side DNa04, w-cHIN group 10147, and IN groups 17171, 13109 and 19157, are omitted. While neurotransmitter prediction for IN groups 17171, 13109 and 10764 are below threshold (<0.7; open arrowheads on edges), their hemilineages suggest that 13109 (6A) and 10764 (19A) are GABAergic, while 17171 (18B) is cholinergic (Lacin et al., 2019). Side annotation is neck side for DNs, output nerve side for MNs, and soma side for others. Synapse weight (neuron-to-neuron mean) is thresholded at ≥20, except for connectivity from w-cHINs to MNs. **F.** Convergence of DN and sensory input onto w-cHINs. All DNs contributing ≥1% groupwise input to a w-cHIN group are shown as a single node, while sensory neurons grouped by anatomical origin contributing ≥1% input to w-cHIN groups are shown. **G.** Morphology of w-cHINs (top, colored by group), pathway of DNa04 to contralateral b1 and b3 MNs through w-cHIN group 10073 and IN groups 17171 and 10764 (middle), and convergence of SNs and DNs onto w-cHINs (bottom). **H.** Direct lateralized DN input to steering MNs, haltere MNs (from A) and w-cHINs, for DNs providing groupwise input of ≥1% to any. Ipsilateral-contralateral index is calculated by ipsilateral connectivity minus contralateral, divided by their sum. w-cHIN side is considered to be their output side, contralateral to dendrites. DN labels colored red are not within the WTct DN set defined in Figure 10.

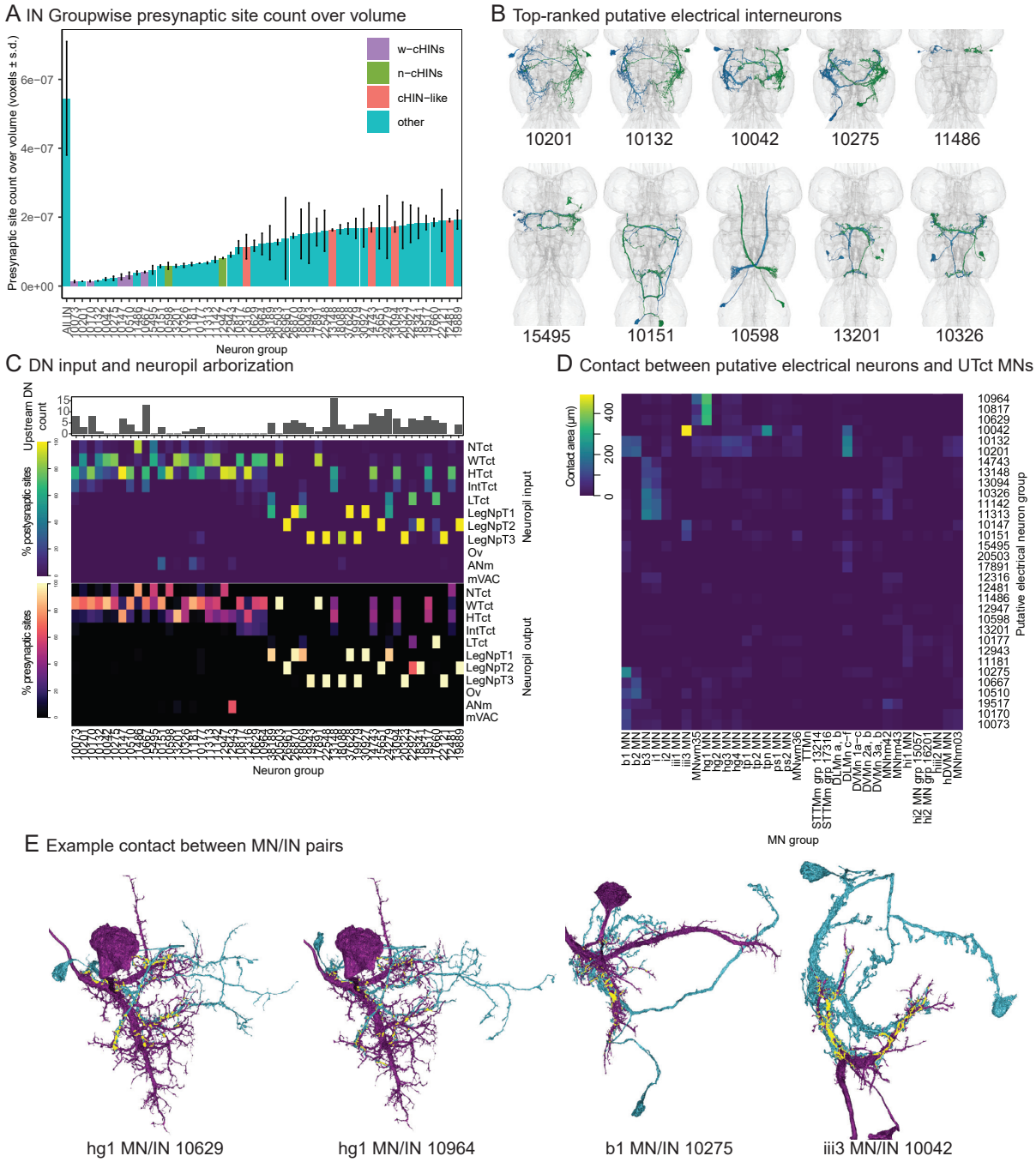

Figure 11—Supplement 1: Putative electrical interneurons in the Upper Tectulum. A. Top 50 intrinsic neuron groups in MANC rank-ordered by low presynaptic site count per neuron volume (groupwise mean), which is suggestive of non-chemical synaptic transmission such as electrical synaptic connectivity. The mean of all VNC intrinsic neurons is also shown. Within the top 50, groups with dense core vesicles (which suggests extrasynaptic neurotransmitter release) or significant reconstruction issues were manually evaluated and excluded (see Supplementary File 4). **B.** Morphology of top 10 rank-ordered putative electrical interneuron groups besides the w-cHINs shown in Figure 11. **C.** Direct DN input count (at ≥1% groupwise input), and neuropil input and output of the top 50 putative electrical interneuron groups. **D.** Mean surface contact area between putative electrical interneurons and all wing and haltere MNs of a group. Contact area was determined by expanding each interneuron and MN by 0.1 µm and calculating the surface area of intersection meshes between every interneuron-MN pair. **E.** Example interneuron-MN pairs with high contact area as determined in (D). Intersection area is shown in yellow on top of the neurons. All views shown in this figure are ventral.

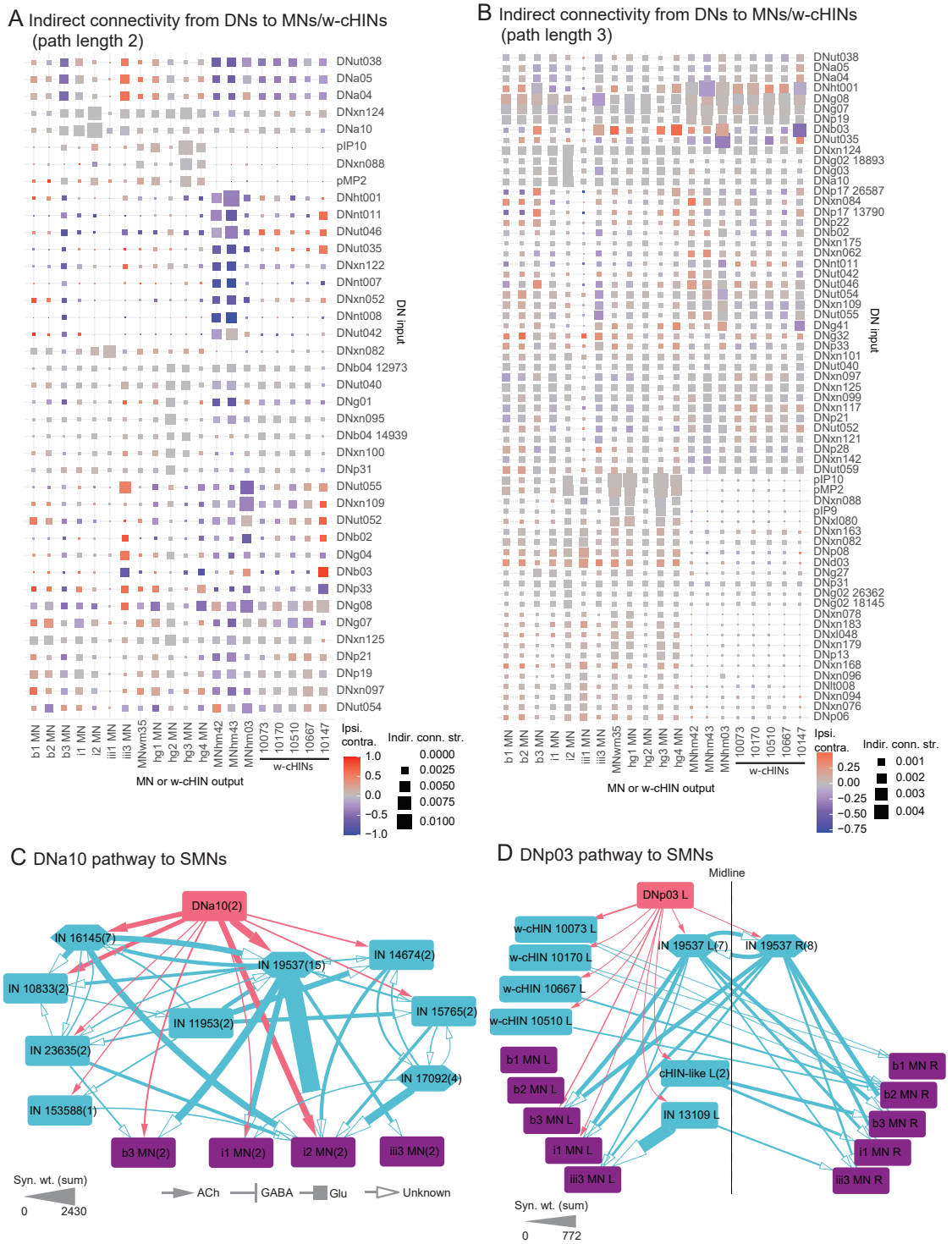

Figure 11—supplement 2: Additional connectivity of DNs controlling steering MNs. A-B. Lateralized indirect connectivity of DNs to steering MNs, haltere MNs and w-cHINs, for path length of 2 (**B**) and 3 (**C**). Un-normalized indirect connectivity strength is used, as a comparison between path lengths is not carried out. Ipsilateral-contralateral index is calculated by ipsilateral connectivity minus contralateral, divided by their sum. For this calculation, w-cHIN side is considered to be their output side, contralateral to dendrites. Only DNs above an arbitrary cutoff value for indirect connectivity strength with MNs/w-cHINs are shown. **C.** Highly bilateral pathway of DNa10 to steering MNs. Synapse weight (group sum) is thresholded at ≥100. **D.** Lateralized path of DNp03 to steering MNs through w-cHINs and other cells. For clarity, only the left DNp03 and interneurons are shown, except for IN group 19537, a bilateral population cell type. Synapse weight (group sum) is thresholded at ≥20. Side annotations are neck input side for DNs, output nerve side for MNs, and soma side for others.

haltere as it moves in antiphase to the wing, and in separate sensory neuron subsets, signals encoding angular changes to the fly from the action of Coriolis forces on the haltere (Heide, 1983; Pringle and Gray, 1948). Oscillatory input from haltere campaniform sensilla is critical for determining the phase-locked timing of SM firing relative to the wingbeat cycle (Fayyazuddin and Dickinson, 1999, 1996; Trimarchi and Murphey, 1997), as the asynchronously-contracting nature of PMs does not allow the fly to determine its phase in the wingbeat cycle from power MN circuit activity alone. The observed convergence of DN and sensory input onto w-cHINs and steering MNs thus suggests a relatively direct method of controlling steering: in tonically active muscles such as b1 and iii3, oscillatory haltere sensory input is the primary driver of wing MN firing, and subthreshold DN input to w-cHINs serves to alter the timing of MN firing in the wingbeat cycle, either causing phase advance from excitatory DN input or phase delay from inhibitory DN input. For phasic MNs such as b2, haltere input to w-cHINs or w-chIN input to the b2 MN is likely subthreshold, and the combined activity of descending and haltere input allows the driving of the MN to threshold while maintaining accurate timing relative to the wingbeat cycle. This connectivity is thus consistent with prior observations of phase tuning to wingbeat as well as phase changes during flight maneuvers in the basalar muscles and other SMs (Egelhaaf, 1989; Götz, 1983; Heide, 1983, 1975; Heide and Götz, 1996). Given that the b1 and b2 muscles both exert similar effects on the wing in isolation, i.e. pulling the basalar apophysis in the anterior direction to move the wing forward (Nachtigall and Wilson, 1967), the shared circuitry through w-cHINs may allow recruitment of variable number of muscles by the same descending steering signals, with smaller magnitude turns only requiring phase shifting of the tonic b1 muscle, while larger magnitude turns further requiring recruitment of the phasic b2 muscle. This wiring also explains the observation that firing of the b2 muscle is almost always concomitant with phase advance of b1 muscle firing, while the reverse is not always true (Tu and Dickinson, 1996).

To further define DNs that may play a role in steering during flight, we examined direct and indirect DN input to steering MNs and w-cHINs by direct input fractions (Figure 11H) and indirect connectivity strength (Figure 11-Supplement 2A, B). As lateralization of steering MN control is key for steering, we also calculated an ipsilateral-contralateral index for both direct and indirect DN-MN connectivity (ipsilateral minus contralateral connectivity over their sum. Overall, both direct and indirect DN input to the SMs provide a mix of bilateral and unilateral connectivity that may allow the muscle combinatorial control underlying the range of aerial maneuvers available to the fly. DNs that have lateralized SM control such as DNa04 and DNa05 likely control turning maneuvers involving yaw and roll, whereas other DNs, such as DNa10 (which also receives input from navigation-related brain areas), provide bilateral input to SMs (Figure 11–Supplement 2A, C), and thus may be involved in wing maneuvers involving bilateral muscle control, such as in changes of thrust, lift, or pitch. The w-cHINs are sites of convergence of direct, highly lateralized input from many DNs, further indicating their likely importance in steering during flight, although they are not the only lateralized pathways from DN to steering MNs.

Interestingly, many DNs that do not appear in our initial WTct DN list (Figure 10A) are found upstream of wing MNs and w-cHINs (red labels on y-axis in Figure 11H). Of note, the cholinergic DNa02 is thought to control turning during walking (Rayshubskiy et al., 2020) and has strong connectivity to leg circuits (see section 2.6), yet also has indirect connectivity with the iii3 MN

through a w-cHIN. Why a walking DN has connectivity with a wing MN is unknown, and indeed DNa02 activation in landed flies does not result in wing motion (Cande et al., 2018). It is possible that DNa02's role in flight is gated by haltere sensory input required to drive the w-cHINs and the iii3 MN, allowing this DN to perform a dual role in steering during walking and flight depending on the behavioral state of the fly–the highly specific connectivity with only the iii3 MN suggests a much more restricted flight role that is perhaps limited to only slow turning, as activation of the iii3 muscle is predictive of slow but not fast increases in wing amplitude (Lindsay et al., 2017).

Visual observation of the EM volume suggests that, in addition to the w-cHINs (and the related neck-cHINs), there are additional groups of putatively electrical neurons that also have large axon diameter and few chemical synapses, including many in the upper tectulum. Trained annotators labeled these neurons 'putative electrical' in the neuprint 'transmission' field, while known electrical neurons from the literature are labeled 'electrical' when identifiable (Marin et al., 2023, this work). To further systematically discover putative electrical INs, we rank-ordered all IN groups of the VNC by mean presynaptic site count over neuron volume (low to high) to find neurons which may carry out neurotransmission through non-chemical synaptic means (Figure 11–Supplement 1A, B). These top neuron groups were manually examined to rule out alternative explanations for low chemical synapse count including significant reconstruction issues or the presence of dense core vesicles (Figure 11–supplement 1A, B, Supplementary File 4). The top-ranking groups largely ramify in the upper tectulum, with some ramifying in leg neuropils (Figure 11–supplement 1C). In addition, many are direct targets of DNs, suggesting that some may play roles in wing control similar to w-cHINs (Figure 11–supplement 1C). To evaluate if any of these cells play a role in electrical wing or haltere motor control, we calculated the physical contact area with wing and haltere MNs for neuron groups within the top 50 that also ramify in tectular regions (Figure 11–supplement 1D, E). Indeed, many putative electrical cells also come into contact with wing MNs, chiefly steering MNs such as the b1, b2, b3, i1, iii3, and hg1 MNs . Together, these observations suggest that electrical connectivity is a widespread mechanism of wing and upper tectular motor control, and many are part of pathways linking DNs to MNs. Indeed, as the high frequency of wing beats during flight (~200 Hz in *Drosophila*) demands rapid and repeated activation of many wing MNs, electrical synapses are well-suited for control of wing MNs without the synaptic fatigue issues associated with chemical neurotransmission. However, as electrical synapses cannot be directly observed at the MANC EM resolution, these putative electrical neurons await experimental confirmation.

Overall, descending and sensory input converges onto w-cHINs, making them highly suited to carry out a role in steering through subsequent electrical input to the b1, b2 and iii3 MNs. Descending input such as those from DNa04 and DNa05 to w-cHINs, combined with oscillatory sensory input from halteres, likely allows a flight maneuver signal to be converted into accurately timed muscle activations relative to the wingbeat cycle. Besides the w-cHINs, other putative electrical INs are prevalent in the upper tectulum and perhaps serve similar roles in wing motor control.

2.5.3 Wing power output is likely driven by diffuse excitatory connectivity

In flies, power generation for the high frequency wingbeats necessary for flight are driven by action of the PMs–namely the dorsal lateral muscles (DLMs) and dorsal ventral muscles (DVMs), two sets of asynchronous, stretch-activated muscles which function antagonistically to each other (Also see Figure 6A). In this system, the power MNs do not have direct control over PM spike timing, and thus the timing of wingbeats. Instead, power MN spiking (~5Hz) is over an order of magnitude lower than the *Drosophila* wingbeat frequency (~200Hz, Figure 12A; (Gordon and Dickinson, 2006), and is thought to play a permissive role to enable PM contraction, as well as control calcium availability in PMs to modulate their power output (Gordon and Dickinson, 2006; Lehmann et al., 2013; Wang et al., 2011).

To begin examining power MN function in MANC in relation to descending control, we examined the upstream connectivity of power MNs, particularly in relation to connectivity from DNs of interest that are directly or indirectly upstream of power MNs such as DNa08, DNa10, DNp31, DNg02 and DNp03, and may thus play a role in wing power control. Strikingly, when considering population-wise input, all power MNs receive heavy shared input from a population of ~21 pairs of wing upper tectular intrinsic neurons ('Tect IN', Figure 12B-D) that were categorized into 11 groups by variations in morphology. While each individual Tect IN contributes relatively low input to power MNs (mean of 22 synapses per Tect IN with each power MN), together they comprise 7-23% of total input to each power MN. These cells also have input or output with many other top contributors of input to the power MNs, and receive input from most DNs that are upstream of power MNs, at least at shorter path lengths (Figure 12B). In addition, the Tect INs target the mesVUM-MJ/T2VUM1, an efferent neuron that likely provides modulatory octopaminergic input to the DLMs (Ehrhardt et al., 2023; Schlurmann and Hausen, 2003). DNs and other cells associated with Tect INs commonly have input to the ps1 MN and the likely ps-related MNwm36, suggesting that control of thorax rigidity/tension by the ps muscles is intimately tied to control of wing power output. The Tect IN pathway is one of three routes from DNs to power MNs. Two other pathways are taken to power MNs by the courtship song DNs (pIP10 and pMP2) and the putative navigation-related DNa10, respectively–these routes also have some indirect connectivity with the Tect IN pathway (Figure 12–supplement 1B, C).

Prior work has observed that the power MNs exhibit slow out-of-phase spiking during flight, with a loose order enforced on the MNs of the fibers of each PM motor unit (Harcombe and Wyman, 1978, 1977; Tanouye and Wyman, 1981; Wyman, 1966), which is a hypothesized mechanism to convert a discrete flight signal, such as from DNs, into more smoothly graded power changes. The out-of-phase firing of power MNs led experimenters (Harcombe and Wyman, 1977) to suggest that each power MN may summate many small excitatory postsynaptic potentials from a common source over time to independently reach their spiking threshold, as opposed to single strong excitation sources which would lead to synchronous spiking. The large population of Tect INs is an excellent candidate to carry out such a function–they are likely cholinergic (excitatory) by their 19B hemilineage (Lacin et al., 2019), and their input from DNs may serve to activate 'diffuse' activity within the population, which is then contributed to the power MNs via relatively small individual synapse counts. Furthermore, 7% of Tect IN connectivity is contributed by weak intra-population recurrent connectivity (Figure 12–supplement 1A), likely leading to

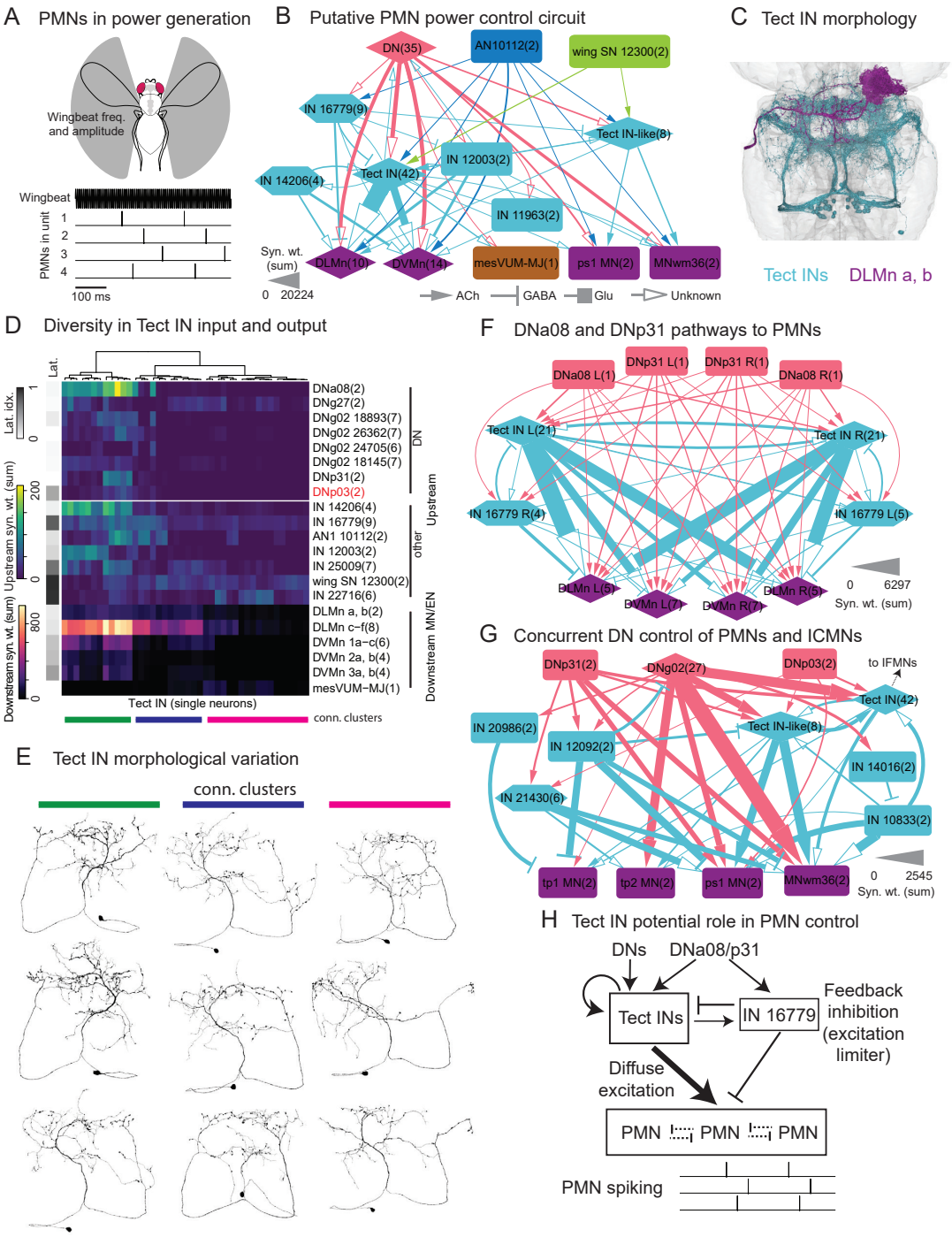

Figure 12: Putative power muscle control circuit in flight. A. Power generation by the power muscles (PM) in flight drives wingbeats. Drosophila wingbeats are over an order of magnitude slower than firing of power MNs (PMNs), and power MNs within the same motor unit fire in a loose, staggered pattern, likely to smooth out power muscle calcium changes and power generation. Wingbeat and power MN traces artistically rendered from prior descriptions (Harcombe and Wyman, 1978, 1977; Tanouye and Wyman, 1981; Wyman, 1966). **B.** Upstream connectivity of the power MNs (dorsal lateral, DLMns and dorsal ventral, DVMns). The bulk of upstream connectivity of the power MNs is contributed by 42 tectular intrinsic neurons (Tect INs), with many DNs (here subsetted by ≥1% groupwise connectivity with Tect IN groups) and several other neuron types showing connectivity to Tect INs. Upstream connectivity to the power MNs are also associated with inputs to the ps1 and MNwm36 wing MNs, and the mesVUM-MJ which targets the dorsal lateral muscles. Edges are thresholded at ≥100 synapses. **C.** Morphology of the Tect IN population, shown together with a single DLMn. *(cont.)*

Figure 12: *(cont.)* **D.** Connectivity of the Tect INs (individual neurons on x-axis) with upstream DNs and other cells, and downstream MNs/efferents (collapsed by group). Laterality index is the mean of the difference between side-separated connectivity normalized by their sum. The Tect INs show variation in the combinations and strength of their upstream and downstream connectivity, which is partially reflected in their morphological variation (see E). Neuron groups shown on y-axis are a selection from the top input or output neurons groups connected to Tect INs, except DNp03 (red label) which contributes weaker input but is of behavioral interest. Dendrogram shows hierarchical clustering of Tect INs by the subset of upstream and downstream connectivity shown here. **E.** Morphological variation in Tect INs. **F.** Lateralized connectivity of DNa08 and DNp31 with Tect INs, IN group 16779 and power MNs, forming a motif where the same DNs appear to excite and inhibit power MNs. Side annotation is neck side for DNs, nerve side for MNs, and soma side for others. **G.** Connectivity of three example power MN-associated DNs (DNp31, DNg02 and DNp03) with indirect control MNs. **H.** Schematic of putative power MN control circuit. In flight, DN input controls Tect IN activity, which then excites power MNs through 'diffuse' connectivity (individually small synaptic connections, but collectively strong at the population level). DNa08 and DNp31 further excites IN 16779, which may form an inhibition-stabilized with Tect INs to limit runaway excitation. power MNs sum 'diffuse' excitation from Tect INs to individually reach their spiking threshold, and weak electrical connectivity between power MNs further enforce an inhibition-like connectivity between them, such that power MNs spike in a slow, staggered manner to smooth out power muscle calcium changes.

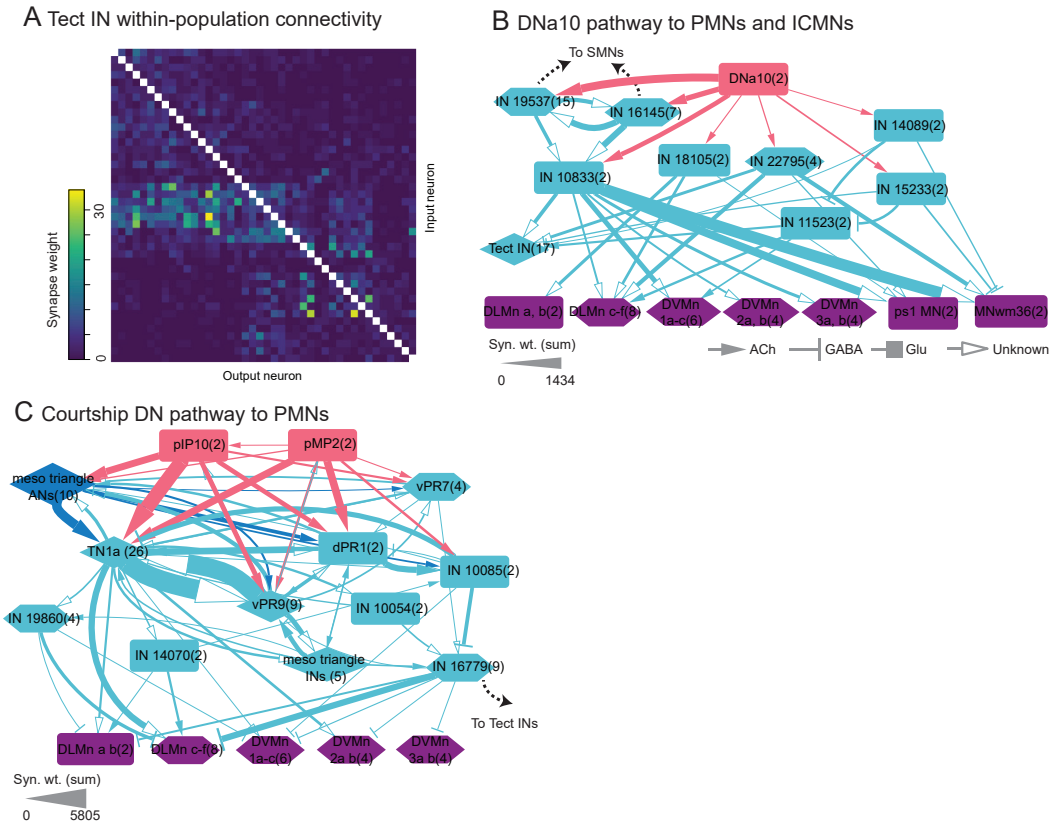

Figure 12–Supplement 1: Additional connectivity from DNs to power motor neurons. A. Tect IN connectivity within the population. Tect INs provide weak recurrent input to each other, with a subset that contributes more input to others. Order of neurons and dendrogram on both axes is the same as for x-axis in Figure 12D. **B.** Pathways of DNa10 connectivity to power and indirect control MNs. IN groups 16145 and 19537 also have connectivity to steering MNs (SMNs), see Figure 11–supplement 1. Tect IN connectivity to power MNs not shown for clarity. **C.** Pathways of the courtship DNs pIP10 and pMP2 to power MNs. IN group 16779 has connectivity with Tect INs (see Figure 12F). Identification of the TN1a, dPR1 and vPR9 cell types in MANC by (Lillvis et al., 2023). Synapse weights of all graphs are thresholded at ≥100.

self-reinforcing activation and signal amplification of DN input. Out-of-phase firing of the power MNs are likely then further promoted by weak electrical connectivity between the power MNs themselves, which through experimental and modeling studies are thought to lead to a limited possible set of DLMn spiking orders (Hürkey et al., 2022). The minimal circuit elements described here may be sufficient to drive the CPG-like control of out-of-phase power MN spiking, as well as provide a means of modulating power MN spike rate through which other neurons or circuits act.

Interestingly, the Tect INs are not a homogenous population. Rather, they include a range of connectivity strengths with their top upstream and downstream partners (Figure 12D) as well as a range of morphologies (Figure 12E). By hierarchical clustering of Tect INs connectivity (with only the top upstream and downstream partners), Tect INs may be divided into 3 clusters, and we observe that DN input to Tect INs is largely concentrated within a single Tect IN cluster (except for DNg27 input), with the same cluster having higher output to power MNs (although all clusters have power MN output). The other clusters have higher input from a single wing SN pair (group 12300), as well as IN group 22716, which receives input from wing SNs—these cells represent the main route of sensory input to Tect INs. In addition, a degree of left-right asymmetry of calcium activity in PMs has been observed during flight and is thought to modulate PM power output to support turning (Lehmann et al., 2013). To examine if lateralization of Tect IN inputs and outputs may play a role in asymmetric power modulation in PMs, we calculated a lateralization score for Tect IN connectivity ranging from fully bilateral (score of zero) versus fully lateralized (score of one, Figure 12D, left bar). Overall, Tect IN connectivity to power MNs are weakly lateralized, suggesting that lateralized Tect IN activation likely generally activates excitatory drive to all power MNs but potentially still causes weakly-lateralized power changes. However, direct DN input to Tect INs are almost fully bilateral, except for connectivity from DNp03; although its connectivity is weaker than other DNs, this putative looming responsive DN (Namiki et al., 2018) also has connections to w-cHINs and steering MNs (Figure 11–supplement 1D), which together may support concurrent turning with increase in wing power during flight that perhaps aids in evasive maneuvers. Of other lateralized upstream partners, the sensory paths from wing SN group 12300 and IN group 22716 are highly lateralized, suggesting that wing sensory input may trigger partially lateralized power MN activity through Tect INs. Lastly, connectivity from IN group 16779 to Tect INs is also highly lateralized and is followed up in the next paragraph.

Of Tect IN inputs, IN 16779 is unusual in that it is likely inhibitory (GABAergic) by its 6B hemilineage (Harris et al., 2015) and neurotransmitter prediction. It has reciprocal connectivity with Tect INs, and is a target of two cholinergic DNs, DNa08 and DNp31, which provide input to Tect INs and are also the strongest direct DN inputs to power MNs (Figure 12F). DNa08 is likely implicated in navigation as it receives input from the lateral accessory lobe and posterior slope in the brain (Namiki et al., 2018), while DNp31 is likely implicated in responses to salient visual stimuli as it receives input from lobula columnar neuron types LC22/LPLC4 and LPLC3 (Namiki et al., 2018). Together, these neurons form an unusual motif where the same descending input appears to both excite and inhibit power MNs (Figure 12F, H). While the actual function of this motif is unknown, one intriguing possibility is that the recurrent excitatory and inhibitory connections in the Tect INs and IN 16779 form an inhibition-stabilized network, where a stable

level of excitatory activity can be maintained in the excitatory subnetwork with feedback inhibition from the inhibitory subnetwork serving to prevent runaway excitation (Sadeh and Clopath, 2021). Such networks are notable for the paradoxical observation that excitation to the inhibitory neurons decreases the steady-state activity for both the inhibitory and excitatory neuron populations (Sadeh and Clopath, 2021)–the input from DNa08 and DNp31 to the Tect INs and IN 16779 may thus serve to shift the steady-state activity of the network by decreasing IN 16779 activity and counteracting the corresponding decrease in Tect IN activity. Alternatively, short-duration DN input to both Tect IN and IN 16779 may serve to transiently increase Tect IN activity with delayed feedforward inhibition from IN 16779, causing momentary changes in wing power output. In addition, several DNs (DNp31, DNg02 and DNp03 examples in Figure 12G) as well as Tect INs themselves take pathways to indirect control MNs–namely to the tergopleural and pleurosternal MNs which may control thoracic stiffness or tension. While the roles of the ICMs in flight have not received as much investigation as other muscle categories, it appears that concurrent control of PMs and ICMs are important for the function of DNs such as the DNg02s which modulate wingbeat amplitude in flight (Namiki et al., 2022; Palmer et al., 2022).

In summary, we observe that the power MN upstream network is largely shared among all power MNs and is highly bilateral. The Tect INs provide diffuse excitatory connectivity to the power MNs, potentially facilitating staggered firing of power MNs and control of power MN power output, and is also the main, but not only, target of descending control to the power MNs. Descending input often targets Tect INs and power MNs directly, and two excitatory DNs (DNa08 and DNp31) target both the WTct INs and the potentially inhibitory IN 16779 which we hypothesize to form an inhibition-stabilized network with Tect INs (Figure 12G). Thus, wing premotor networks are partitioned into distinct circuits that control power and steering, an organization reflective of the functional specialization of each wing muscle type and also clearly present at the DN level. In addition, the pathways from courtship DNs to wing MNs appear largely distinct from pathways from flight-related DNs. Excitatory and inhibitory connections feature in the circuits upstream of both power and steering MNs, but appear to play different roles, at least in the pathways we explored in detail–these connections are commonly lateralized in steering circuits to allow left-right asymmetrical control of steering MNs, while for the power MN circuit, inhibition appears to function mainly as a means of excitation control. Lastly, circuits controlling indirect control MNs appear mixed with circuits controlling steering or power, suggesting that indirect control muscles may play a supporting role to the function of steering or power muscles.

2.6 Organizational logic of DNs onto leg circuits

We next turn our attention to premotor circuits of the leg motor system. The six legs of the fly are primarily used together for walking. Rhythmic motor output produces alternating leg movements termed stance (the power phase when legs are in contact with the ground) and swing, that together allow the animal to move efficiently. Flies display a range of walking gaits in which different patterns of inter-limb coordination are observed. Although these motor patterns must respond to changing environmental conditions (Büschges et al., 2011), flies have been shown to walk normally without proprioceptive feedback, suggesting that inter- and intra-leg

coordination is not dependent on sensory feedback loops from the legs (Mendes et al., 2013). While headless flies have been shown to generate locomotion patterns, the movements are often uncoordinated, possibly due to the lack of input from descending neurons (Gao et al., 2013; Mendes et al., 2013).

In the following sections, we carry out an initial analysis of leg motor circuits, with a focus on those involved in walking. We first identify a repeated premotor-MN circuit that is consistent among all three pairs of legs; we refer to this as the 'standard leg connectome'. We then describe the neurons upstream of this circuit which interconnect different leg neuropils; these are likely responsible for inter-leg coupling. Finally, we identify DNs providing input to leg neuropils and examine how they modulate this leg circuit.

2.6.1 The leg premotor circuit is serially repeated across segments

To identify neurons that might contribute to premotor walking circuits, we first examined neurons upstream of the leg MNs (defined in Figure 7). Unlike the upper tectulum motor systems, leg anatomy and its muscular organization is segmentally repeated across the fly's three thoracic segments, which is also reflected at the leg MN level and their upstream circuits. We found that over 75% of leg MN presynaptic partners are intrinsic neurons restricted to a single leg neuropil (Figure 13A). Nearly 50% of these restricted neurons (totalling about 1200 per leg neuropil) have been serially matched across the six neuropils (Figure 13B) (Marin et al., 2023). Our Infomap community detection (Figure 9) also found six very similar communities, each consisting of ~1200 neurons mostly restricted to single leg neuropils. Together this suggests that each set of leg muscles within a hemisegment is driven by a locally restricted circuit that controls and coordinates leg muscles; inter-leg coordination presumably depends on the much smaller set of neurons with inter-neuropil connectivity.

This modular and repeated organization means that we can use serial homology between leg neuropils to simplify the representation and analysis of leg circuits. Furthermore, this helped us to overcome some inconsistencies in the reconstruction state of leg MNs. The standard leg connectome is therefore defined as the serially repeated units common to all legs including the presynaptic neurons directly upstream of serially identified leg MNs (Figure 13C). For this analysis, we grouped the serial MNs by their leg muscle target as shown in Figure 7. The premotor circuit is large and complex even when considering only the strongest connections between presynaptic neurons and serial leg MNs (using a threshold of 40 input synapses to each MN group averaged across each leg) (Figure 13C). This standard leg connectome was very similar across legs, but there were small deviations between T1, T2, and T3 legs, as shown in Figure 13–Supplement 1.

Neurotransmitter predictions in the dataset assist greatly in interpreting the circuit logic within this standard leg connectome (Figure 13D). For example, there are five GABAergic restricted neuron sets that strongly inhibit MNs innervating the thorax muscles responsible for the rotation of the leg. One of these GABAergic IN sets (serial set 10652) inhibits the Sternal anterior rotator MNs that rotate the leg forwards during the swing phase of forwards walking. The other four GABAergic sets (IR_11029, IR_10679, IR_10144, IR_10236) target the opposing MNs (Pleural

remotor/abductor and Sternal posterior rotator MNs), active in the stance phase that propel the body forwards (Figure 14D, left panel). These strong inhibitory input neurons are characteristic of most leg MNs; furthermore, the interneurons also receive strong inhibitory input themselves, suggesting that inhibition and disinhibition are key motifs in leg premotor circuits.

We also find glutamatergic interactions. Although we cannot be certain of their sign, existing evidence is consistent with inhibitory function of glutamatergic synapses in the CNS (Liu and Wilson, 2013; Marin et al., 2023). There are two glutamatergic INs (IR_10586, IR_11340) upstream of the Tibia extensor MNs and two upstream of the Tibia flexor MNs (IR_10062, CR_10852), and these two sets also target each other, likely forming a reciprocally inhibitory microcircuit (Figure 13D, central panel).

The GABAergic and glutamatergic circuit motifs that we have just described involve neurons targeting the same jointed segment of each leg. However each step when walking requires coordinated movement between the different segments of each leg. We do observe circuit motifs including INs targeting MN for muscles in different leg segments. These include a set of three GABAergic (IR_10108, IR_10215, IR_10233) and three cholinergic (BR_10715, IR_10274, IR_11751) IN serial sets that interact upstream of the Trochanter flexor and the Tibia extensor (Figure 13D, right hand panel). While each MN group has an upstream IN partner that can specifically activate or inactivate them, they also share a GABAergic and a cholinergic IN set (IR_10215 and IR_10274), suggesting that there are movements in which both muscles must be simultaneously active or inactive, at least for a short period. Nevertheless, most of the premotor circuit is separated by leg compartments. The Femur reductor MNs are an exception, sharing glutamatergic INs and one GABAergic IN sets with the Pleural remotor/abductor and Sternal posterior rotator MNs (Figure 13E) suggesting a simultaneous inactivation. However, these neurons do not share the same cholinergic activation. Since the flexor and accessory flexor muscles have a similar basic action on the legs joints, it is not surprising to see that there are many similarities in their connectivity (Figure 13F).

Our first impressions of the circuits contained within the standard leg connectome can be summarized as follows. First, there is strong direct inhibitory input onto leg MNs. Layered on top of this are strong inhibitory and excitatory interneurons from additional leg-specific interneurons, which we expect to be functionally disinhibitory or inhibitory with respect to the MNs. Some inhibitory interneurons show reciprocal inhibitory patterns e.g. to control antagonistic motor neurons / muscles. However, other interneurons instead show a layered inhibitory organization in which some neurons can control others: this could potentially generate sequential activation of different muscles during the walking cycle. The overall impression is of a high degree of circuit complexity associated within each individual leg neuropil. The extensive inhibitory interactions could easily define circuits with oscillatory activity. Together this suggests that much of the pattern generating activity of pre-motor circuits could operate at the level of a single leg.

2.6.2 Inter-leg coordination is not purely inhibitory

Six-legged insects, such as the fly, primarily walk with a tripod gait, in which two sets of three legs alternate a stance (contacting ground) and a swing (non-contact moving forward or

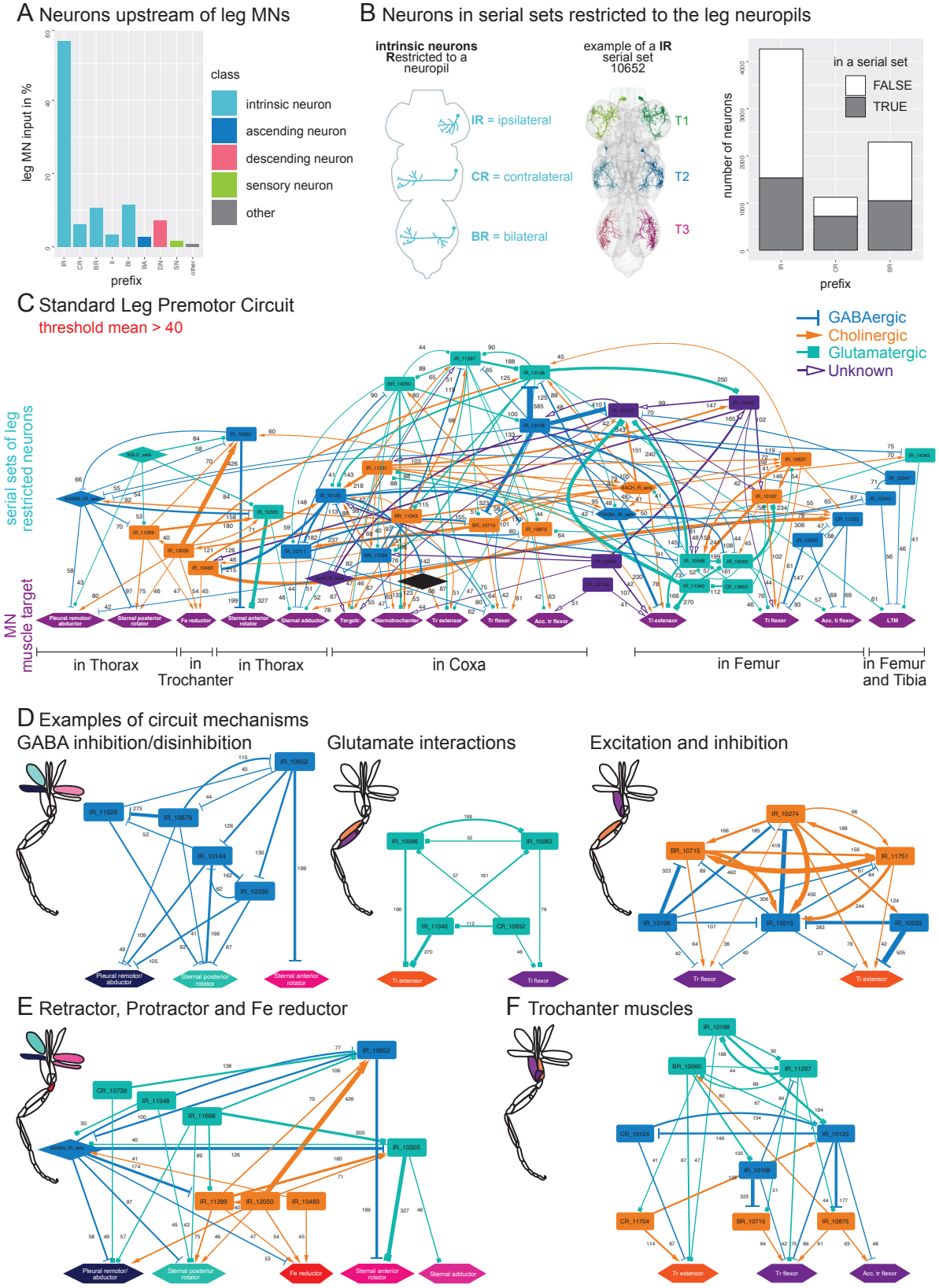

Figure 13: Standard Leg Connectome. *(cont.)*

Figure 13: *(cont.)* Leg premotor circuit local to all three leg neuropils. **A.** Input to leg MNs in percent. Colour indicates the class of input neuron and the x-axis additionally splits up the intrinsic neurons into subclass (prefix). **B.** Over 75% of input onto leg MNs comes from intrinsic neurons restricted to the leg neuropils. Schematic illustrates the distinction between the three types of restricted neurons: IR, CR, BR. Next to it an example of a IR serial set (10652) colored by leg neuropil. On the right the number of neurons in the VNC with those prefixes. Color indicated if the neuron is sorted into a serial set. **C.** Premotor circuit of all Leg MNs that are in serial sets. All connections between serial leg restricted neurons and MNs are shown (weight > 40), collapsed by serial set (see Figure 13—Supplement 1 for differences between leg circuits). Color of intrinsic neurons indicates the neurotransmitter prediction. Squares are single serial sets, hexagons are grouped serial sets. **D.** Examples taken from C to show a GABA, Glutamate and GABA/Cholinergic mechanism of controlling the leg MNs. **E.** Interconnection between the MNs in the Thorax with the Fe reductor. **F.** Major serial sets controlling the trochanter MNs. MNs in D,E and F are shown in the colour of the leg muscle they control, schematic.

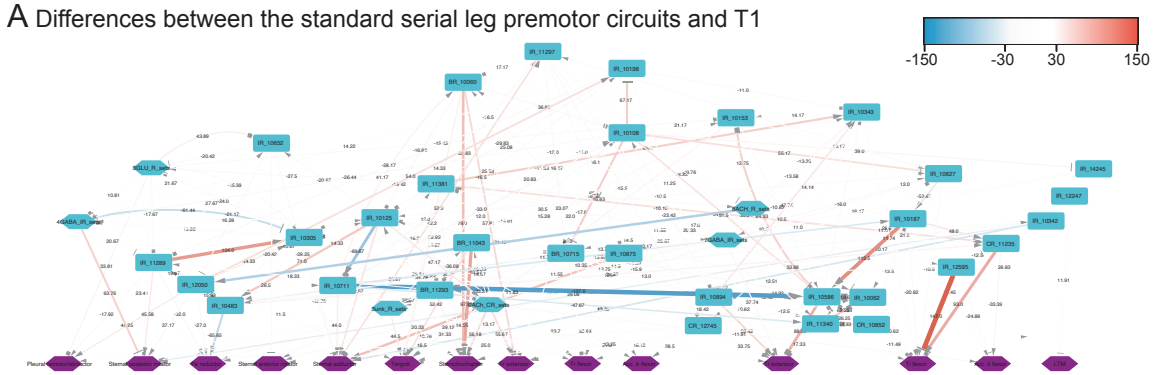

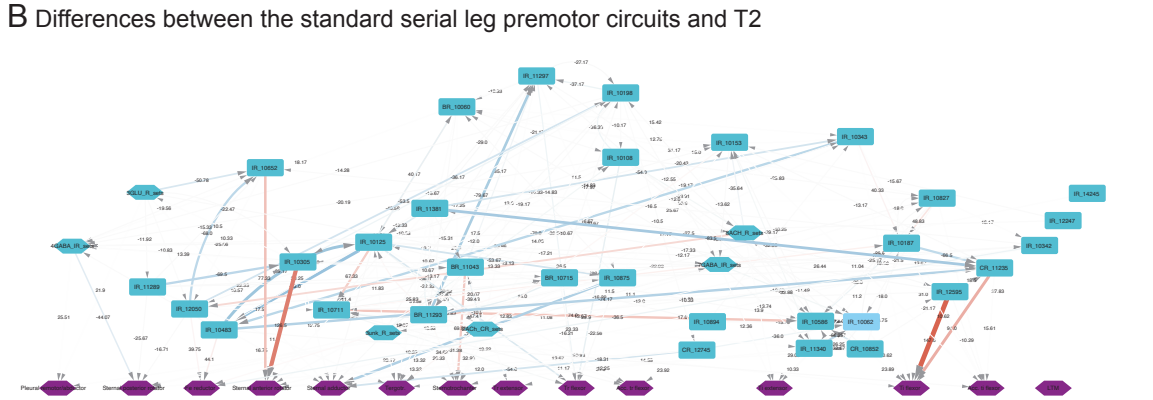

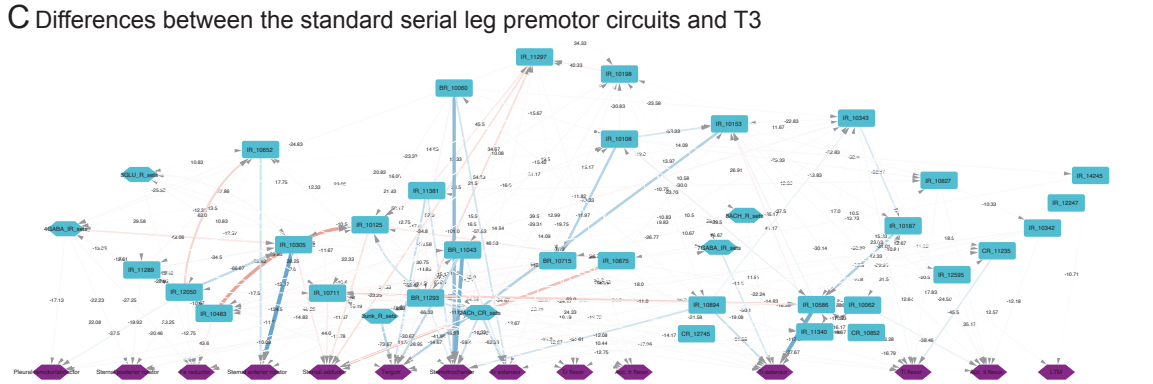

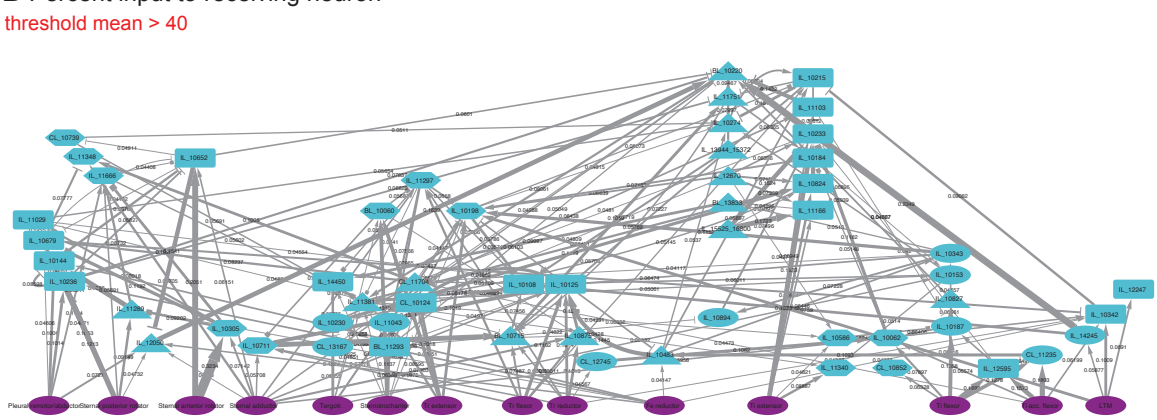

Figure 13—Supplement 1: Differences in the Standard Leg Connectome across segments. Difference between the mean connection of the serial set and T1, T2 or T3 specific connections in **A, B, C** accordingly. Weight difference is color-coded, with red indicating stronger connections and blue meaning weaker connections compared to the mean connection of the serial set. Intrinsic serial sets are in light blue, motor neuron serial sets by muscle target in purple. Squares are single serial sets, hexagons are grouped sets.

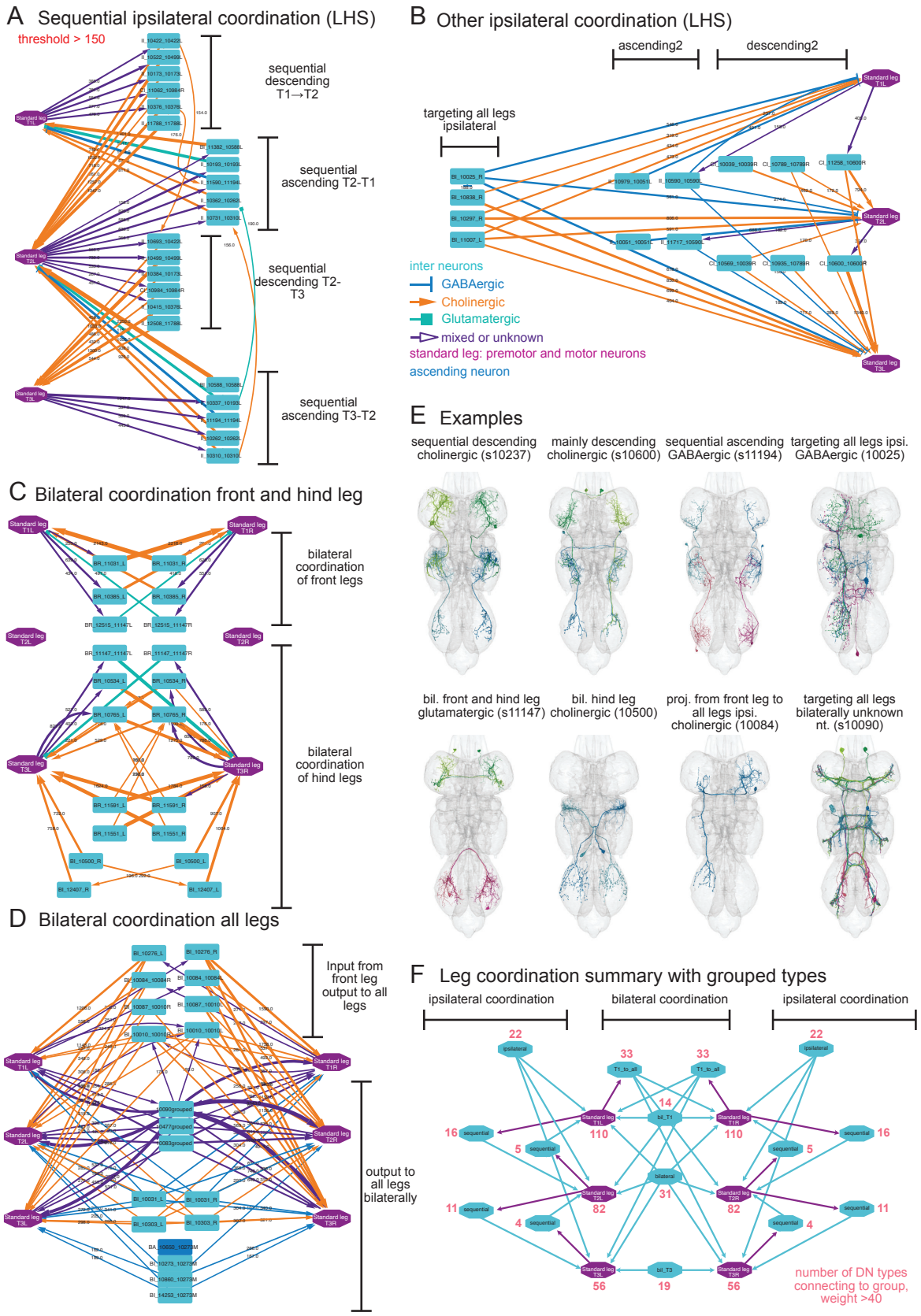

Figure 13—Supplement 2: Coordination of leg premotor circuits. Grouped intrinsic neurons upstream of the standard leg premotor circuit with effective connectivity (see Materials and Methods). **A.** Serially repeating intrinsic neurons that ascend or descend a segment with their axonic projections. **B.** Ipsilaterally connecting intrinsic neurons, targeting several leg premotor circuits. **C.** Intrinsic neurons connecting T1 leg or T3 legs bilaterally. **D.** Intrinsic neurons projecting from T1 on one side to all leg premotor circuits on the other side and neurons that project to all leg premotor circuits. **E.** Examples of intrinsic neurons in the different groups shown in A-E. **F.** Summary of the groups and their connection to the standard leg premotor circuits of the six legs. Numbers indicate the number of DN types that connect to these groups with weight >40.

backwards) phase. Each set forms a passively stable ‘triangle’ to support the animal during stance and thus consists of two ipsilateral legs and a contralateral leg (i.e. left front, right middle, and left hind). Thus, walking requires coordination between different legs, both across thoracic segments and left/right hemispheres.

To investigate how motor actions are coordinated between different legs, we next looked at inputs to the standard leg connectome, focusing on neurons that are not restricted to a single leg neuropil. To do this, we conducted an effective connectivity analysis including both direct and indirect (multi-hop) connections for all the serial MNs and serial INs in the standard leg connectome (see Materials and Methods for details). We grouped the INs by their subclass (see Marin et al., 2023). This distinguishes neurons arborizing on one side of the VNC (subclasses II and CI) that likely contribute to ipsilateral leg coordination from INs that may mediate coordination of the two hemispheres (bilateral subclasses BI and BR). For ipsilateral coordination, we further distinguished between INs forming two different patterns of neuropil arborization, namely those that were sequentially projecting from a leg neuropil in one thoracic segment to a leg neuropil in an anterior or posterior segment (‘sequential’) and those that ipsilaterally targeted leg neuropils in all three segments (‘ipsi’). We observed that the neurons with the *sequential* serial motif had all been annotated in serial sets of four neurons that connect legs 1 and 2 or legs 2 and 3 (Marin et al., 2023). Six sequential groups receive inputs from a variety of neurons from the standard leg connectome in T1 or T2 and then project their axons posteriorly to the next segment, T2 or T3 (Figure 13—Supplement 2, panels A and E). Five sequential sets do the opposite, projecting anteriorly from T2 or T3 to T1 or T2 (Figure 13—Supplement 2, panels A and E). The morphology and connectivity of these sequential neurons strongly suggests that they coordinate legs across segments. However five out of five groups projecting posteriorly and three of five groups projecting anteriorly are cholinergic in contrast to previous predictions of inhibitory interconnections (DeAngelis et al., 2020; Grillner and Kozlov, 2021; Hiraoka, 2021).

In addition to these sequential neurons, we also found one GABAergic and three cholinergic neurons that target all three leg connectomes equally and could potentially be involved in amplifying or attenuating signal to the premotor circuits in response to input they receive in other regions of the VNC (see 10025 example that received inputs form different areas of the tectulum in Figure 13—Supplement 2E). We expected to see bilateral connections between the left and right standard leg connectomes for each segment. However, while T2 leg bilateral INs exist, they did not appear in our analysis even when specifically looking just upstream of the T2 standard leg neurons. We conclude that coordination between the two front legs or between the two hind legs is likely to be more important for the direct premotor circuits (Figure 13C).

While two of the bilateral pairs in T1 and T3 are serial sets (see example 11147, Figure 13—Supplementary Figure 2E) there are several specific T3 bilateral neurons that get input in other areas of the VNC such as the Ov (see example 10500). Interestingly, we found a handful of neurons that receive input from the T1 leg circuit and then project to all leg circuits on the opposite side. We speculate that these might be involved in either turning or providing left-right coordination (Figure 13—Supplementary Figure 2D top). Additionally we observe a group of

neurons that output strongly to all leg neuropils, which are predominantly GABAergic or of unknown neurotransmitter (Figure 13—Supplementary Figure 2D,E).

This analysis of the interconnections between the circuits associated with each individual leg, gives a framework for how the six legs of the fly might be coordinated (Figure 13—Supplementary Figure 2F). Many different circuit configurations for a central pattern generator to coordinate walking in *Drosophila* have been proposed, but the neurons that could generate this rhythmic pattern of activity have not been identified (Agrawal et al., 2020). Our analysis identifies a relatively small number of strong candidate cell types controlling inter-leg coordination that should be the target of future experiments.

2.6.3 Descending neurons input to both the intra and inter leg circuits

To evaluate how descending input from the brain DNs modulate premotor leg circuits we identified the DNs that provideinput to the different components of our standard leg circuit (numbers in Figure 13—Supplementary Figure 2F). We systematically typed DNs by the neuropil they target (see cell typing section) (Figure 14). We observe that direct connectivity between leg DNs (DNfl, DNml, DNxl) and leg MNs is rare and often weak. While in some cases this is due to badly reconstructed leg MNs in the dataset, we see that even well-reconstructed leg MNs are usually targeted by DNs via at least one IN. Therefore, we calculated effective connectivity to find the strongest path from each leg DN to all leg MNs (by target muscle) and the number of layers between them (see Materials and Methods, Figure 14–Supplement 1-4).

DNg12 is the only neuron identified within the DNfl subclass. It is involved in anterior grooming, including front leg rubbing and ventral head sweeps (Guo et al., 2022). We looked to see if other DNs have similar or clearly distinct MN effective connectivity. While most of the DNfl neurons exclusively target MNs in the T1 leg segment, some, including DNfl012 and DNfl016, also target MNs in T2 and T3 (Figure 14–Supplement 1). DNfl008 has similar leg MN targets as DNg12 with an even stronger normalized connectivity score. DNfl040 is one of the few bilaterally projecting DNfl neurons that additionally targets MNs on the contralateral side.

The biggest subclass of leg DNs are those that innervate several leg neuropils, DNxl. The DNxl effective connectivity is more diverse than the DNfl subclass (Figure 14–Supplement 2). We picked out some representative examples of DNxl that were either targeting different muscle groups in different leg segments (DNxl111), targeting specifically the Tibia flexor muscle (DNp10), targeting different thorax muscles in T2 and T3 (DNg38), targeting similar MNs and with similar morphology (DNxl134 and DNxl040), or having a strong Trochanter extensor connection to T2 and T3 leg MNs (Figure 14–Supplement 3). We also looked at DNxn neurons that had a strong effective connectivity to leg MNs (Figure 14–Supplement 4A), which target some of the leg MNs but as well as other MNs in the VNC (Figure 14–Supplement 4C).This group includes two LTct-targeting DNs, DNp07 and DNp11, that drive behaviors requiring simultaneous movement of both the wings and legs (Ache et al. 2019; Dombrovski et al. 2023). In section 2.7 we discuss circuits in the LTct that may contribute to this inter-neuropil coordination.

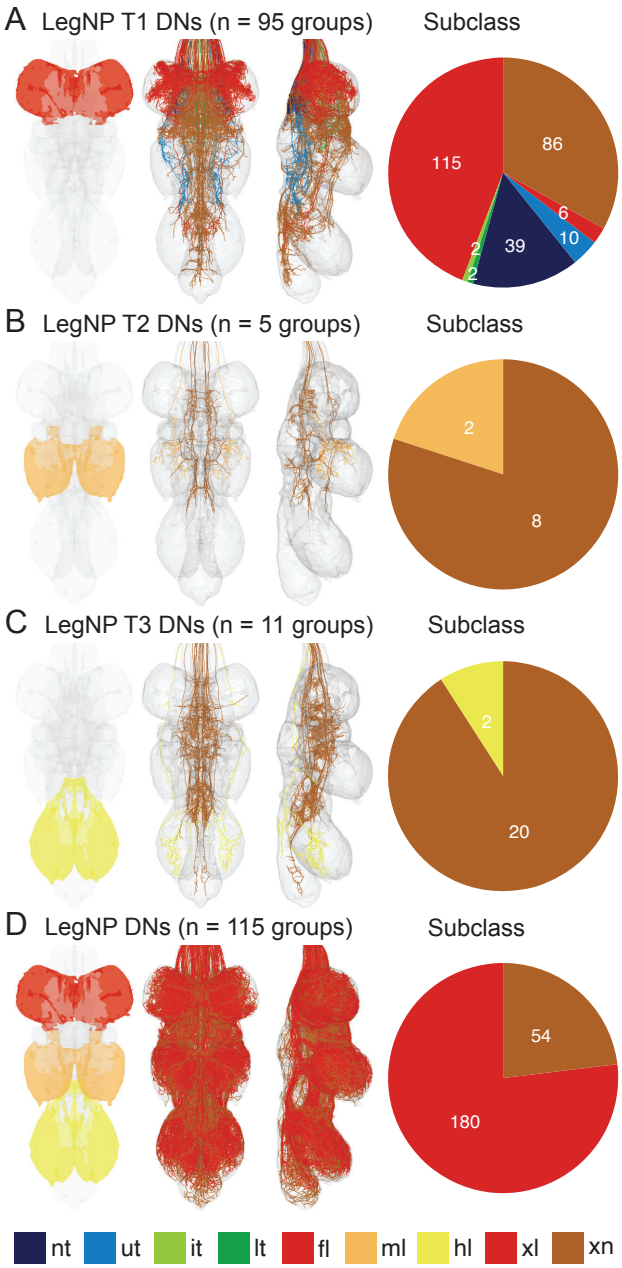

Figure 14: Descending neurons innervating the leg neuropils. DNs that innervate the different leg neuropils with at least 10% of their presynaptic budget and 100 presynaptic sites (group total for both). Their morphology is shown in a ventral and lateral view color coded by their subclass. The number of groups fulfilling the criteria is indicated in brackets and pie charts on the right show subclass (legend at the bottom) composition of the DNs for each innervation type. **A.** DNs innervating LegNP T1 indicated by red area mesh in VNC cartoon on the left. **B.** DNs innervating LegNP T2 indicated by orange area mesh in VNC cartoon on the left. **C.** DNs innervating LegNP T3 indicated by orange area mesh in VNC cartoon on the left. For A, B and C DNs that also dedicated more than 10% of their output budget to the respective other LegNPs are excluded. **D.** DNs that innervate all three thoracic leg neuropils fulfilling the above criteria for each LegNP.

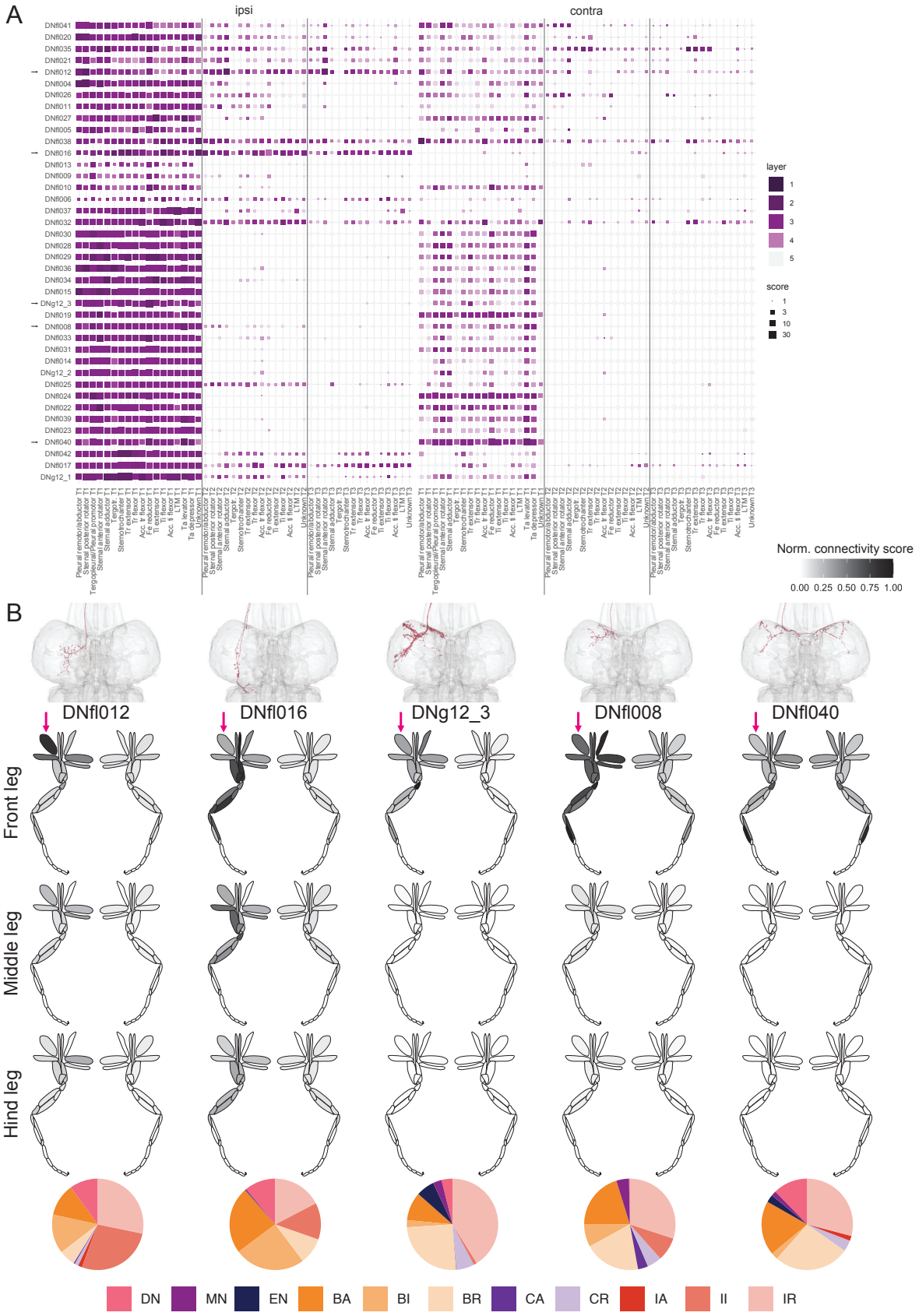

Figure 14—Supplement 1: Effective connectivity of DNfl subclass neurons. A. The effective connectivity of DN types to the leg MN muscle targets ipsilateral and contralateral to the root side of the DN. The MNs are separated by the three segments T1-T3. The shade of magenta encodes for the layer in which the DN targets the MN (1-5), while the size of the square reflects the connectivity score, which reflects the strength of the connection (see Materials and Methods for details). **B.** Examples indicated with an arrow in the top row shows the morphology of the DN. The pink arrow indicates the root side of the DN. Underneath are schematics of the 6 leg muscles with the normalized connectivity score to the different muscles highlighted in shades of grey. The bottom row shows the percent direct output to neuron classes and subclasses in the form of prefixes (Marin et al., 2023).

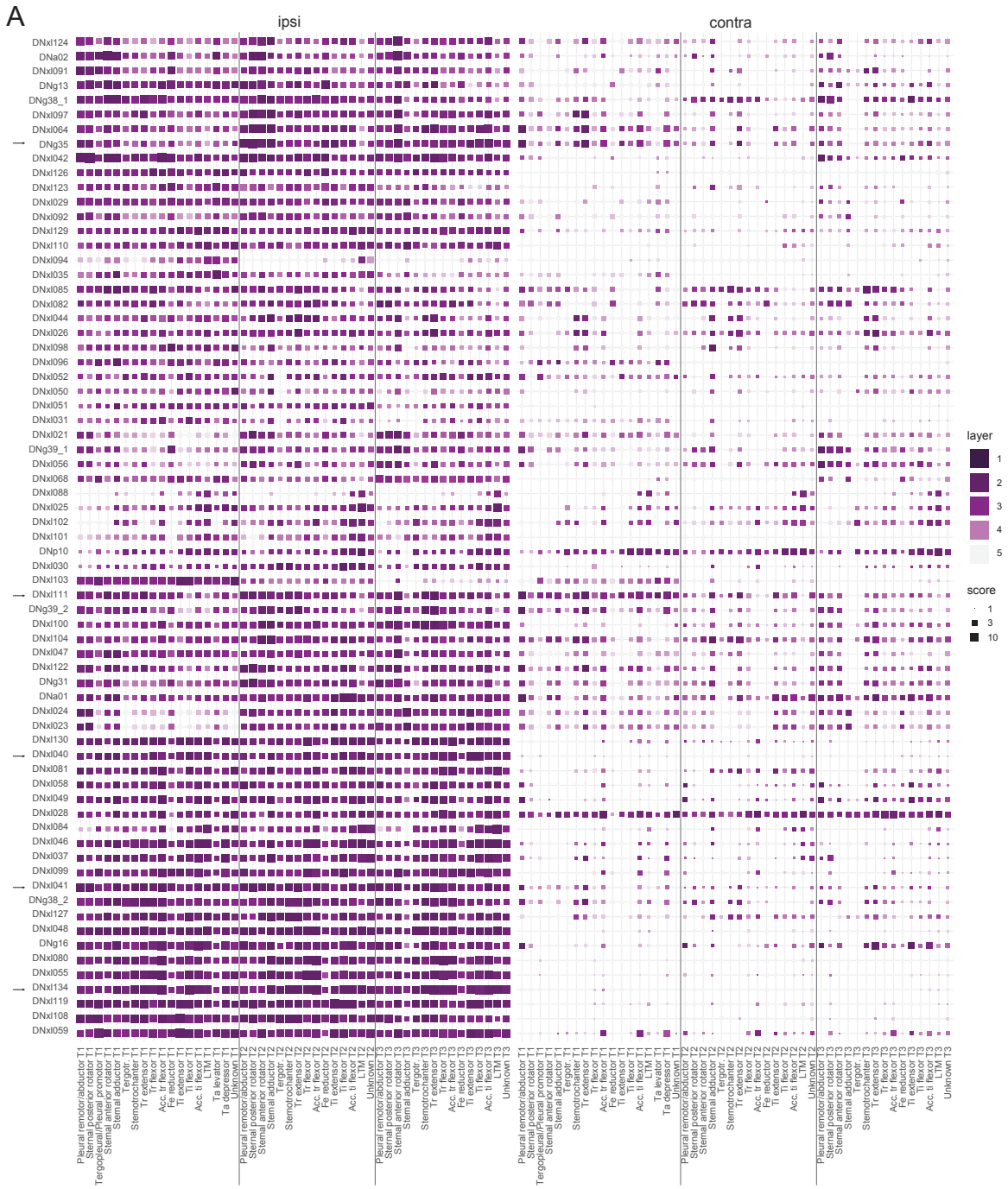

Figure 14—Supplement 2: Effective connectivity of DNxl subclass neurons. A. The effective connectivity of DN types to the leg MN muscle targets ipsilateral and contralateral to the root side of the DN. The MNs are separated by the three segments T1-T3. The shade of magenta encodes for the layer in which the DN targets the MN (1-5), while the size of the square reflects the connectivity score, which reflects the strength of the connection (see Materials and Methods for details).

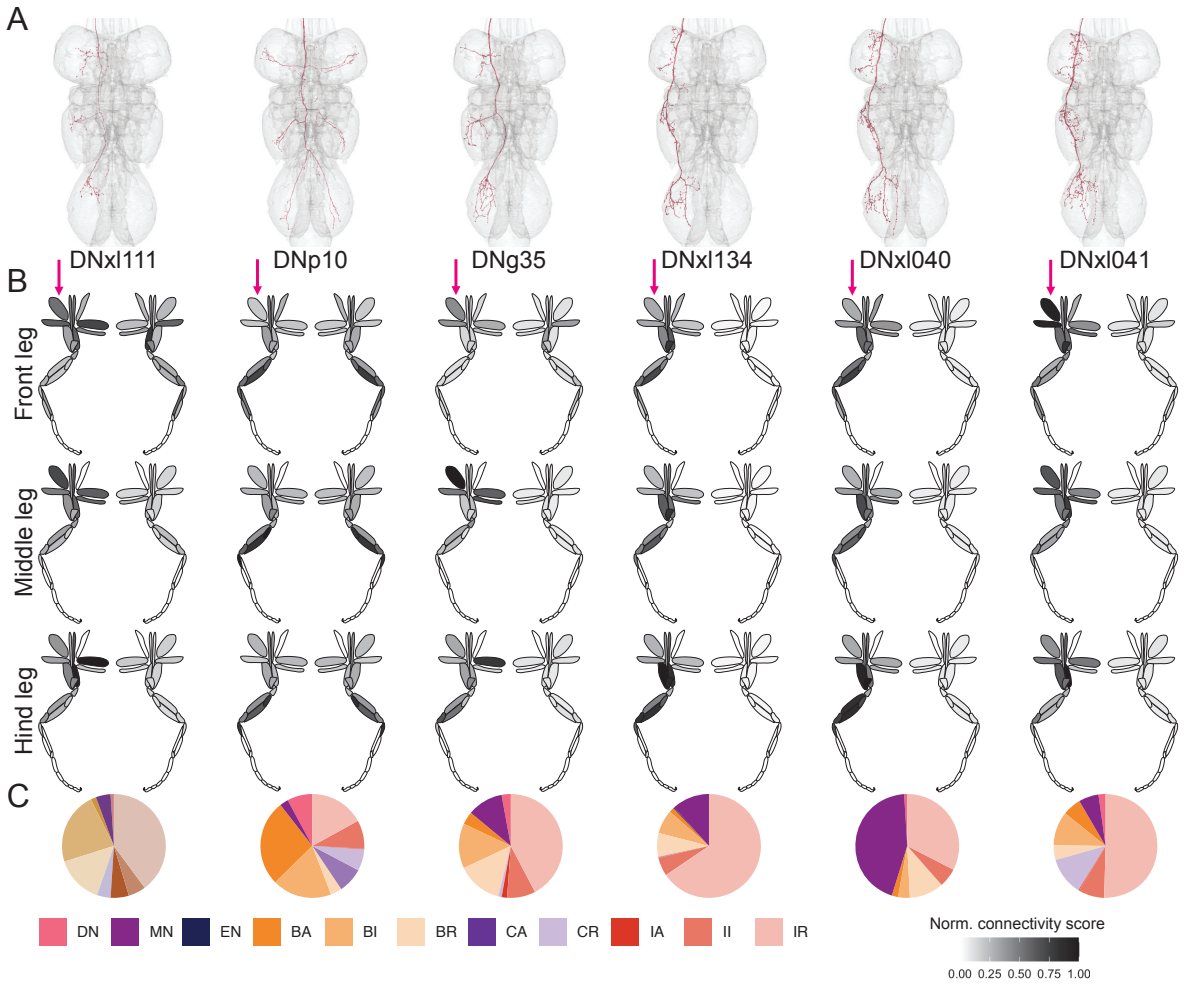

Figure 14—Supplement 3: Examples of DNxl subclass neurons. Examples indicated with an arrow in Figure 14—Supplement 2. **A.** Morphology of the DNxl neurons. The pink arrow indicates the root side of the DN. **B.** Schematics of the six leg muscles with the normalized connectivity score to the different muscles highlighted in shades of grey. **C.** The percent direct output to neuron classes and subclasses in the form of prefixes (Marin et al., 2023).

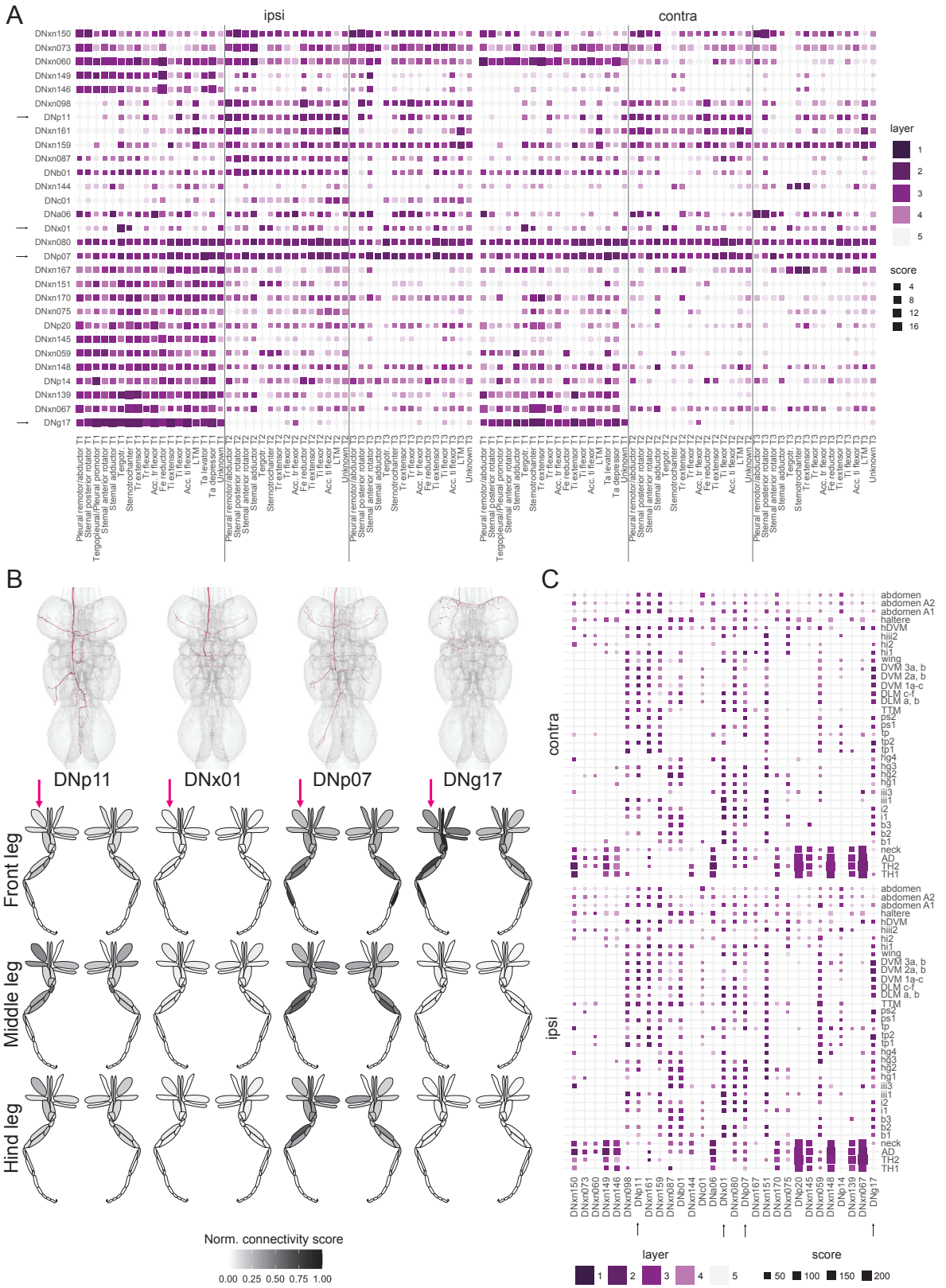

Figure 14—Supplement 4: Effective connectivity of DNxn subclass neurons. A. The effective connectivity of DN types to the leg MN muscle targets ipsilateral and contralateral to the root side of the DN. Only those DNxn neurons were chosen that had the highest effective connectivity scores to leg MNs. The MNs are separated by the three segments T1-T3. The shade of magenta encodes for the layer in which the DN targets the MN (1-5), while the size of the square reflects the connectivity score, which reflects the strength of the connection (see Materials and Methods for details). **B.** Examples indicated with an arrow in A. The top row shows the morphology of the DN. The pink arrow indicates the root side of the DN. Underneath are schematics of the 6 leg muscles with the normalized connectivity score to the different muscles highlighted in shades of grey. **C.** DNxn neurons innervate several neuropils. The effective connectivity to other MNs targets are shown, separated by ipsilateral and contralateral.

By first analyzing circuits containing DNs with known behaviors, we are able to make predictions for the function of previously uncharacterized DNs. In the following two sections, we specifically looked for DNs similar to the identified Moonwalker DN (MDN), known for backwards walking (Bidaye et al., 2014; Guo et al., 2022) and DNa02, known for turning during walking (Rayshubskiy et al., 2020).

2.6.4 Turning DNs

DNa02 has been described to increase locomotor activity when activated bilaterally (Cande et al., 2018). However there is also strong evidence that lateralised activity drives flies to turn towards the activated side during walking (Rayshubskiy et al., 2020). We used effective connectivity to identify leg DNs with similar MN connectivity patterns (Figure 14 Supplement 2). Of previously characterized neurons, we found that DNg13 showed a highly similar effective connectivity fingerprint. Matching both of these DN type to light-level images from previous literature, allowed us to visualize their morphology in the brain (Namiki et al., 2018; Rayshubskiy et al., 2020) (Figure 15A). They have similar dendritic morphology in the brain, both receiving input from the lateral accessory lobe (LAL), an integration center of multimodal inputs from higher brain areas associated with steering (Namiki and Kanzaki, 2016; Scheffer et al., 2020). However, intriguingly, while DNa02 descends into the VNC on the ipsilateral side, DNg13 crosses in the brain and innervates the contralateral hemisphere in the VNC (Figure 15A). In the published literature, DNg13 is suggested to be involved in reaching movements (Cande et al., 2018), but these circuit observations are consistent with both types having a role in turning.

The effective connectivity analysis identifies the MNs and muscle groups in the leg that are most targeted by DNa02 and DNg13 (Figure 15–Supplement A, B) but does not reveal whether these connections are excitatory or inhibitory. Indeed although the axons of both DNs extend into all three leg neuropils, they have very distinct morphologies, suggesting that their first order partners may be different. We first established which groups of neurons in our general leg circuit are targets of these two DNs (Figure 15B) and then identified more complex neuronal circuits (Figure 15C).

The targets of DNa02 and DNg13 include many components of the standard leg connectome, encompassing downstream partners from all three leg neuropils (shown in purple in Figure 15B). However they differ in the groups that they target upstream of the serially repeated standard leg connectomes: DNa02 targets sequential neurons that project up from T2 to T1, while DNg13 targets a sequential neurons that project down from T1 to T2 and from T2 to T3 (illustrated in light blue in Figure 15B). Moreover, DNa02 strongly targets BI_12068, a group of predicted cholinergic neurons with input from T1 on one side and projections to all 3 contralateral leg neuropils; this suggests a role coordinating premotor circuits on the two sides of the VNC (Figure 15D).

A more granular examination of the efferent connectivity of DNa02 and DNg13 reveals clear differences in their connection to MNs in the Thorax and Trochanter (Figure 15C, Figure 15–Supplement 1 A,B). DNa02 (shown on the left) targets two GABAergic serial sets of INs (10144 and 10652) that inhibit the MNs involved in the rotation of the leg during stance and

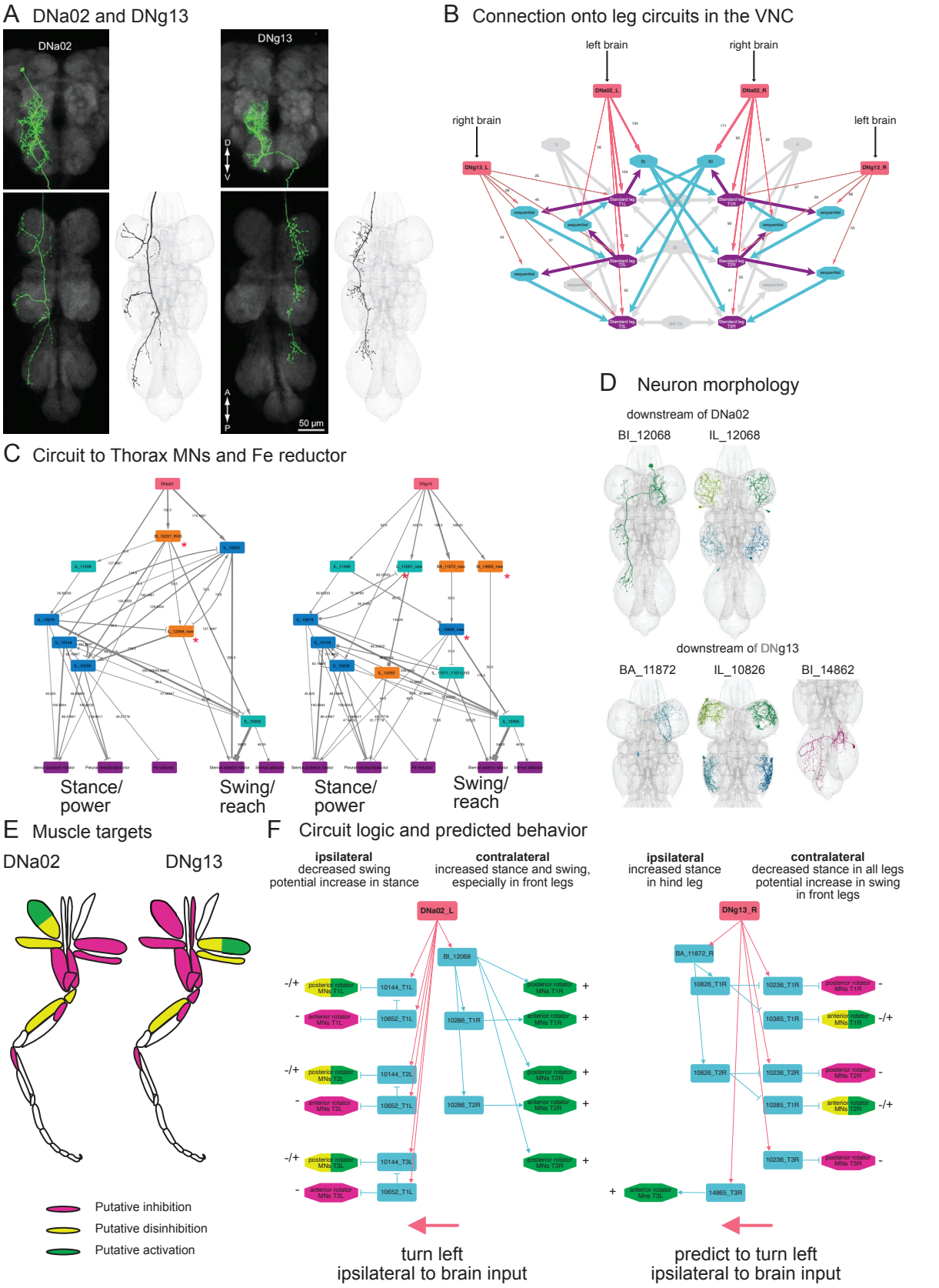

Figure 15: Connectivity of DNa02 and DNg13. A. Light microscopy images of DNa02 and DNg13 from (Namiki et al., 2018) with their MANC axonic match. **B.** connection of DNa02 and DNg13 in MANC into the leg coordination circuit groups from Figure 13. **C.** Leg circuit summarized across leg neuropils and hemispheres for DNa02 and DNg13 separately. Only showing connections onto the thorax and throchanter MNs. Red stars indicate neurons that do not serially repeat in all three segments and are therefore not in the standard leg connectome. **D.** Morphology of neurons downstream of DNg13 or DNa02, marked with * in C. **E.** Leg Muscles targeted, coloured by putative inhibition, activation or disinhibition. **F** Illustration showing the connectivity across segments and hemispheres with the predicted putative inhibition, disinhibition and activation MNs marked on the ipsi and contralateral side in respect to the brain morphology and soma location.

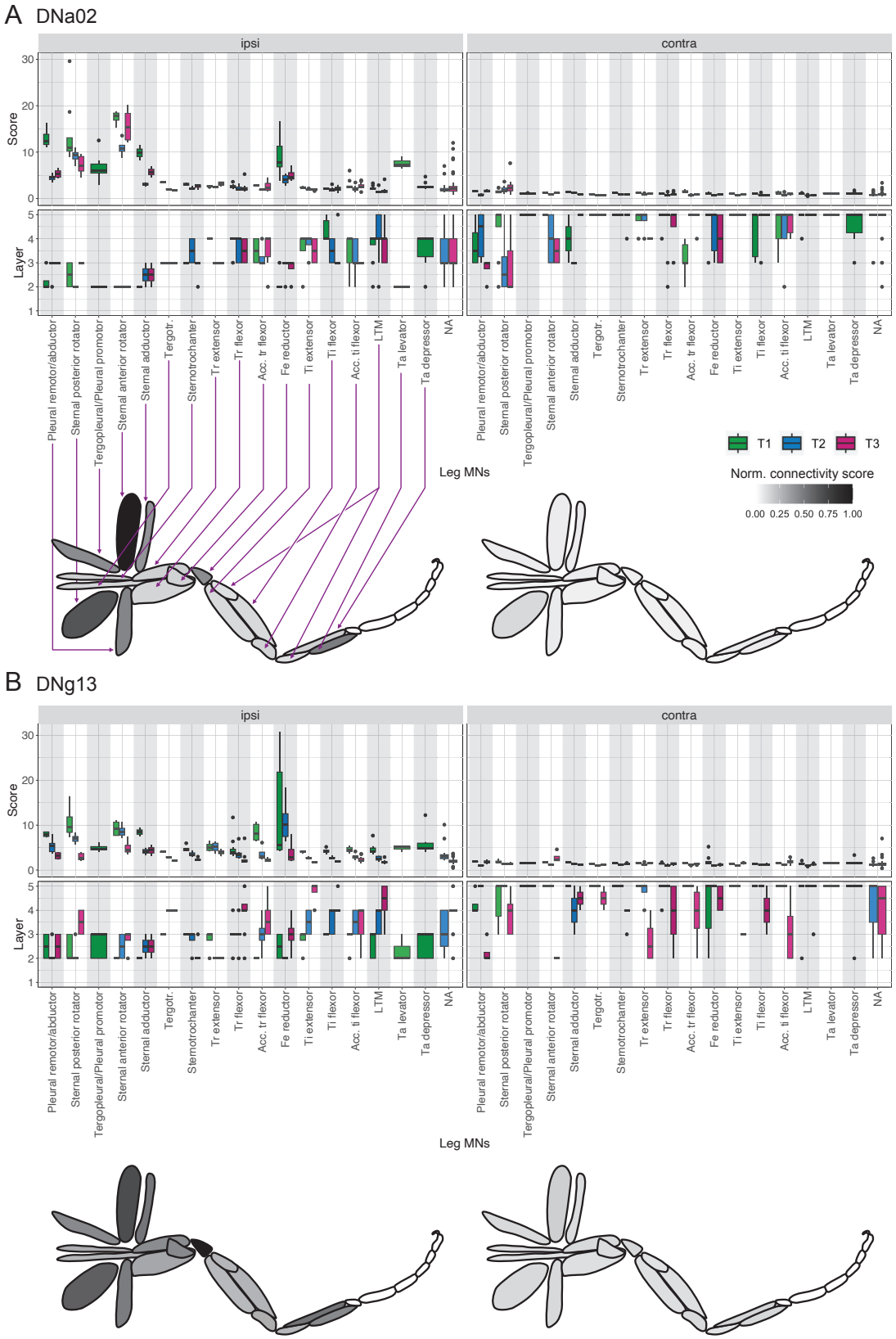

Figure 15—Supplement 1: Effective connectivity of DNa02 and DNg13. Connectivity to ipsi- and contralateral leg MNs for the three neuromeres separately. **A.** DNa02 and **B.** DNg13 connectivity. Connectivity score represents the strongest connection in the network (either direct or via interneurons, four at maximum) based on the normalized matrix product of percent of input to the receiving neuron (top row, see Methods). The layer in which the highest connectivity score was present is shown in the bottom row plots. First layer represents direct DN to MN connectivity, second layer is DN-> IN -> MN, third layer includes two interneurons and so on. Leg muscle cartoons show a normalized score averaged across all three legs for each muscle. Darker color indicates stronger effective connectivity from the DN to MNs controlling the muscle.

swing phase on the ipsilateral side, suggesting a reduction of stride on the ipsilateral side consistent with the previous behavioral study (Rayshubskiy et al., 2020). Through a cholinergic bilaterally interconnecting neuron mentioned above (BI_10297, see Figure 15F), DNa02 directly targets the serial MN set (Sternal posterior rotator MNs) involved in stance and indirectly target the MN set in T1 and T2 (Sternal anterior rotator MNs) involved in swing via one IN, suggesting an increase in the stride especially in the front and middle legs. Interestingly, the BI connects to a GABAergic and a glutamatergic (i.e. predicted inhibitory) set of neurons on the contralateral side; this may coordinate the necessary inhibition of the same MNs. In contrast, DNg13 (shown on the right) targets the stance/power MNs via the inhibitory serial set IL_10228, contralateral to the brain input. A strong connection to the swing/reach MNs occurs via a cholinergic ascending neuron (BA_11872) which potentially disinhibits the MNs through a GABAergic serial set (IL_10826) only observed in T1 and T2. This disinhibition could explain the previously observed reaching when the DN is activated on both sides of the brain (Cande et al., 2018). However, a single DNg13, could contribute to turning during walking by increasing the swing specifically in the front leg and slightly in the middle legs on the contralateral side. We additionally see DNg13 connecting to an excitatory neuron BI_14862 which is only present in the hind legs and projects to the ipsilateral hind leg and abdomen (see Figure 15D for morphology). This contributes to the asymmetric activation of MNs necessary for turning by activating the swing/reaching MNs (Sternal anterior rotator MNs) in the hind legs ipsilaterally (Figure 15F). In summary, we show that while the two DNs target similar MNs, they do so through different circuit patterns likely resulting in opposing muscle activation for the thorax rotator muscles (Figure 15E).

DNa02, as described in (Rayshubskiy et al., 2020), likely elicits ipsilateral turns by reducing stride length on the ipsilateral side and increasing rotational movement on the contralateral side. DNg13 targets the contralateral side, likely decreasing the stance phase in all legs and potentially increasing rotation forwards during the swing phase in the front legs and contralaterally increasing stance in only the hind leg. We would expect this to elicit turns ipsilateral to the brain innervation (Figure 15F). Taken together, these results suggest a simple model in which DNa02 and DNg13 could cooperate to elicit turning, one shortening the stride on the inside of the turn, the other lengthening stride on the outside of the turn.

2.6.5 Walking DNs

DNa01 and two unknown DNs, DNxl023 and DNxl024, target similar muscles in the leg as MDN (Figure 16 A,B). However, this is only true when we consider the leg muscle groups. We see clear differences in the muscle targets of these DNs when looking at front, middle and hind legs and the two hemispheres independently (Figure 16–Supplement 1 and 2). While all of these DNs innervate the leg neuropils with very similar morphology (Figure 16A), they differ in the INs they connect to in the different leg segments. DNa01 has been described in steering (Chen et al., 2018; Rayshubskiy et al., 2020) and in the front leg targets, similar to other leg restricted neurons such as DNa02, which inhibit the posterior rotator muscles in the thorax. However, the other downstream neurons important for DNa02 turning are not shared with DNa01, suggesting as previously reported (Rayshubskiy et al., 2020), a different circuit mechanism that could be combined with DNa02 activity. The two previously unidentified DNs have a strong similarity to MDN in the INs that they target, especially in the Trochanter flexor and Tibia extensor circuits.

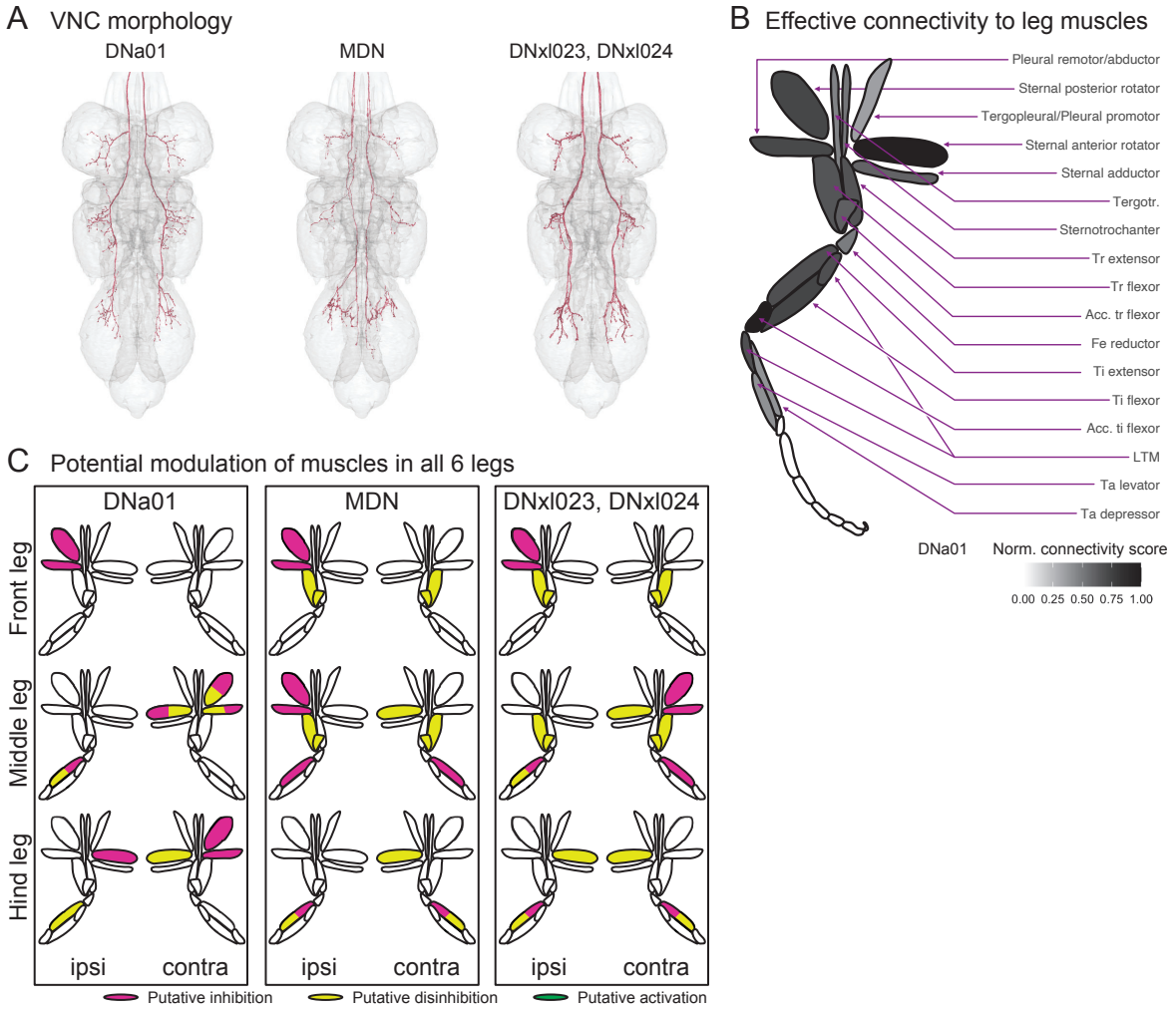

Figure 16: Connectivity of DNa01, MDN and DNxl023, DNxl024. A. Axon morphology of identified DNa01, MDN and two unknown DNs, DNxl023 and DNxl024 that target the three leg neuropils. **B.** In effective connectivity to leg MNs all 4 DN types target the same leg muscles. Example is shown for DNa01, the others can be seen with the exact scores in Figure 16–Supplement 1 and 2. **C.** Predicted modulation of the leg muscles across the 6 legs.

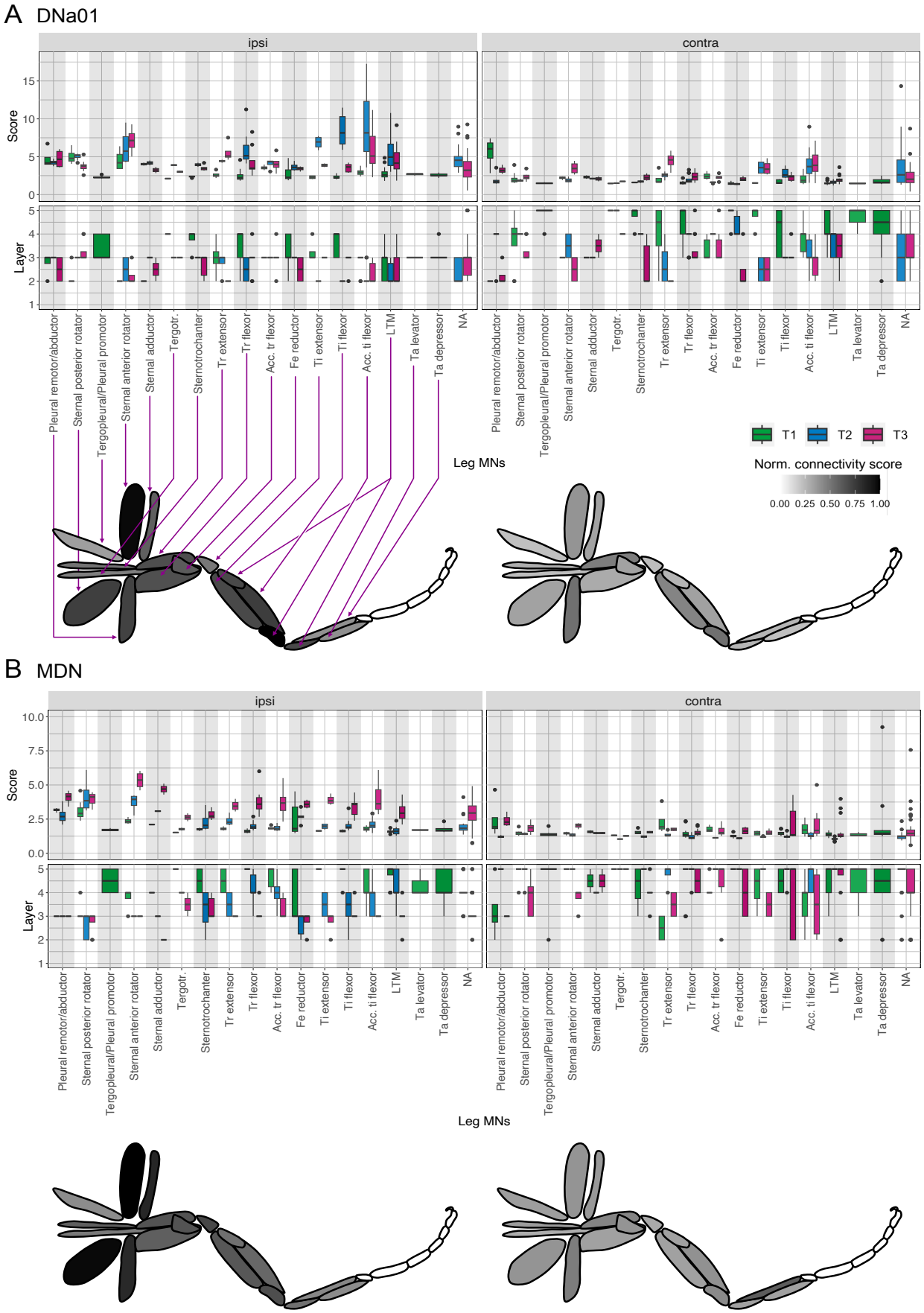

Figure 16—Supplement 1: Effective connectivity of DNa01 and MDN. Connectivity to ipsi- and contralateral leg MNs for the three neuromeres separately. **A.** DNa01 and **B.** MDN connectivity. Connectivity score represents the strongest connection in the network (either direct or via interneurons, four at maximum) based on the normalized matrix product of percent of input to the receiving neuron (top row, see Methods). The layer in which the highest connectivity score was present is shown in the bottom row plots. First layer represents direct DN to MN connectivity, second layer is DN-> IN -> MN, third layer includes two interneurons and so on. Leg muscle cartoons show a normalized score averaged across all three legs for each muscle. Darker color indicates stronger effective connectivity from the DN to MNs controlling the muscle.

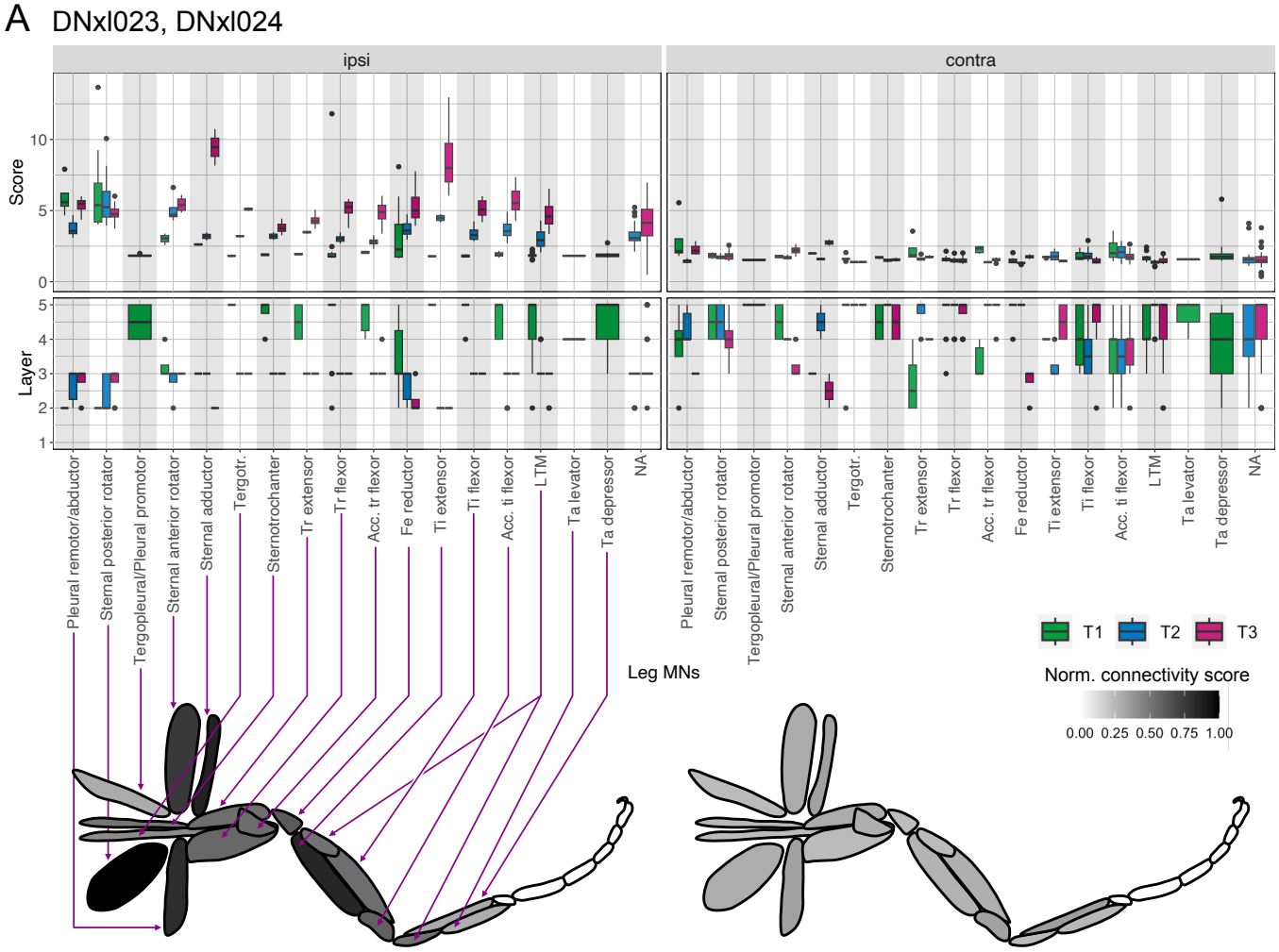

Figure 16—Supplement 2: Effective connectivity of DNxl023 and DNxl024. Connectivity to ipsi- and contralateral leg MNs for the three neuromeres separately. **A.** DNxl023 and DNxl024 joined connectivity. Connectivity score represents the strongest connection in the network (either direct or via interneurons, four at maximum) based on the normalized matrix product of percent of input to the receiving neuron (top row, see Methods). The layer in which the highest connectivity score was present is shown in the bottom row plots. First layer represents direct DN to MN connectivity, second layer is DN-> IN -> MN, third layer includes two interneurons and so on. Leg muscle cartoons show a normalized score averaged across all three legs for each muscle. Darker color indicates stronger effective connectivity from the DN to MNs controlling the muscle.

We find that the strongest connection in the hind legs is through the previously described LBL40 bilateral cholinergic neuron that is one of the top targets of MDN (bodyid: 10994, 11493). This neuron has been described to be sufficient to elicit backwards walking (Feng et al., 2020; Rayshubskiy et al., 2020) and activates the tibia flexor muscles. We were surprised by how strongly MDN also modulates the leg muscles in the middle and front legs. Backwards walking requires a switch of the protractor retractor muscles in the thorax (Rosenbaum et al., 2015). The specific inhibition of the posterior rotator MNs in T1 and T2 could be the basis of that switch. We speculate that a bilateral interconnecting neuron targeted by LBL40 and MDN coordinates this switch.

The connectivity downstream of DNs can be difficult to interpret without first understanding the general leg coordination circuit. Strong connections from a DN to a given MN, even when the target muscle is known, does not automatically predict which behavior activation of that DN will elicit. By first considering the standard circuit logic consistent among the leg premotor circuits and then analyzing how these circuits are interconnected, we have established a basis for interpreting the effect of single DN inputs on motor behavior. The DNa02 and DNg13 example nicely illustrates how we can now use this dataset and its annotations to understand how a known behavior, ipsilateral turning, can be coordinated, and how we can find other DNs that could be involved in the same behavior through a different circuit logic. The DNa01, MDN, DNxl023 and DNxl024 examples show us how targeting the same muscles in different segments can elicit very different behaviors, predicted two new DNs that could be involved in backwards walking, and identified an IN that could be important for the switch from front to backwards walking.

2.7 Organizational logic of DNs onto intermediate neuropil circuits

2.7.1 Organizational logic of lower tectulum circuits

In the sections above we analyzed premotor circuits in the dorsal upper tectulum (UTct) controlling the wing motor system and in the ventral leg neuropil (LegNp) controlling the leg motor system. Intriguingly, our community network analysis implicated the remaining neuropil areas intermediate between these doral and ventral layers (intermediate tectulum, IntTct, and lower tectulum, LTct) as potential areas of higher order processing because they 1) do not contain any MNs, and 2) have more microcircuit motifs with local recurrence compared to other VNC areas. IntTct, which is largely associated with community 9, is tightly interconnected with the UTct communities controlling the wings, halteres, and neck (communities 8, 10, 16, and 17, see Figure 9A). It thus likely serves a higher order control purpose specialized for flight or other actions of the wing motor system. The LTct, however, includes several communities (e.g. 7 and 14), which are distinct from those already discussed in that they provide output to neurons in both the wing and leg motor systems. In particular, the lower tectulum (LTct) is innervated by DNs, INs, and MNs critical for initiating takeoff or landing, suggesting that this region is an important hub for initiating behaviors that require coordinated wing and leg motion (Namiki et al.,

2018) (Figure 17A). In this section we use the MANC data to investigate the connectivity of neurons that innervate the LTct and to identify LTct synaptic pathways linking behaviorally-relevant DNs to their motor effectors.

To begin investigating LTct function and its descending control, we first identified the subset of DNs which strongly targeted the LTct ("LTct DNs", 92 DN groups with ≥10% of their output and ≥100 synapses in the region, Figure 17A). We note that only a minority of LTct DNs exclusively targeted the LTct; most sent additional projections to either the UTct or the leg neuropils (but not both) (Figure 17B). Looking into the cell class composition of DN downstream neurons, LTct DNs make few direct synapses onto MNs. Instead, most LTct DNs output onto INs and ANs (Fig. 17B, C). This synaptic architecture is perhaps surprising, as one might expect that innate, rapid actions such as takeoff or landing sequences would rely upon circuits that minimize synaptic distances between DNs and MNs to increase reliability and decrease latency. And indeed, the best-studied DN-MN pathway in the VNC, the Giant Fiber (GF) circuit that triggers a rapid escape takeoff, resides in the LTct and features direct connections between the GF DN and the tergotrochanter muscle ('jump' muscle') MN (TTMn). We elaborate on this pathway in the following section. However, since our analyses suggested that few of the LTct DNs follow the GF example and initiated motor activity directly, we next examined the connectivity of the network of intrinsic neurons (INs, ANs, and ENs) that are strongly postsynaptic to an LTct DN (≥1% groupwise input and ≥50 synapses) We refer to this set as the LTct DN Downstream neurons. These neurons generally provide most of their output to only 1-2 neuropil regions, although a sizable minority project broadly throughout the VNC (Figure 17B). Furthermore, many of them have significant output to MNs, suggesting that they play a role as downstream motor effectors of LTct DNs (Figure 17B).

We verified these observations by quantifying both the direct and indirect synaptic input from LTct DNs onto downstream MN targets, by groupwise input fractions and normalized indirect connectivity strength (Figure 17C, D). While direct DN-MN connectivity was sparse and relatively weak (only 13/92 LTct DNs provided at least 1% of synaptic input onto any MN; see Figure 17C), the majority of the LTct DNs have indirect impact on a wider range of MNs (Figure 17D). Notably, many LTct DNs provide indirect input to both leg MNs and wing MNs, supporting earlier hypotheses that the LTct is a hub for leg-wing coordination (Figure 17D). Although some DNs had both direct and indirect influences onto the same MN groups (e.g. the GF DN contacts the TTMn both directly and indirectly, and DNp07 contacts tarsal levators both directly and indirectly), overall there was little correspondence between the strongest direct and indirect influences. For example, many LTct DNs provided strong indirect input to the DLMns and DVMns, but none provided direct input to these MNs.

To survey the circuits to which the LTct DNs contribute, we used the results of our earlier Infomap community detection analysis (see section 2.4) to examine the community demographics of LTct DN- Downstream neurons. Notably, communities 7 and 14 were enriched among this population and also tended to contain neurons that received high levels of LTct DN input (Figure 17E, F). These communities (in particular 7) have weaker connectivity with MNs but have strong connectivity with communities that output to leg and wing MNs, consistent with

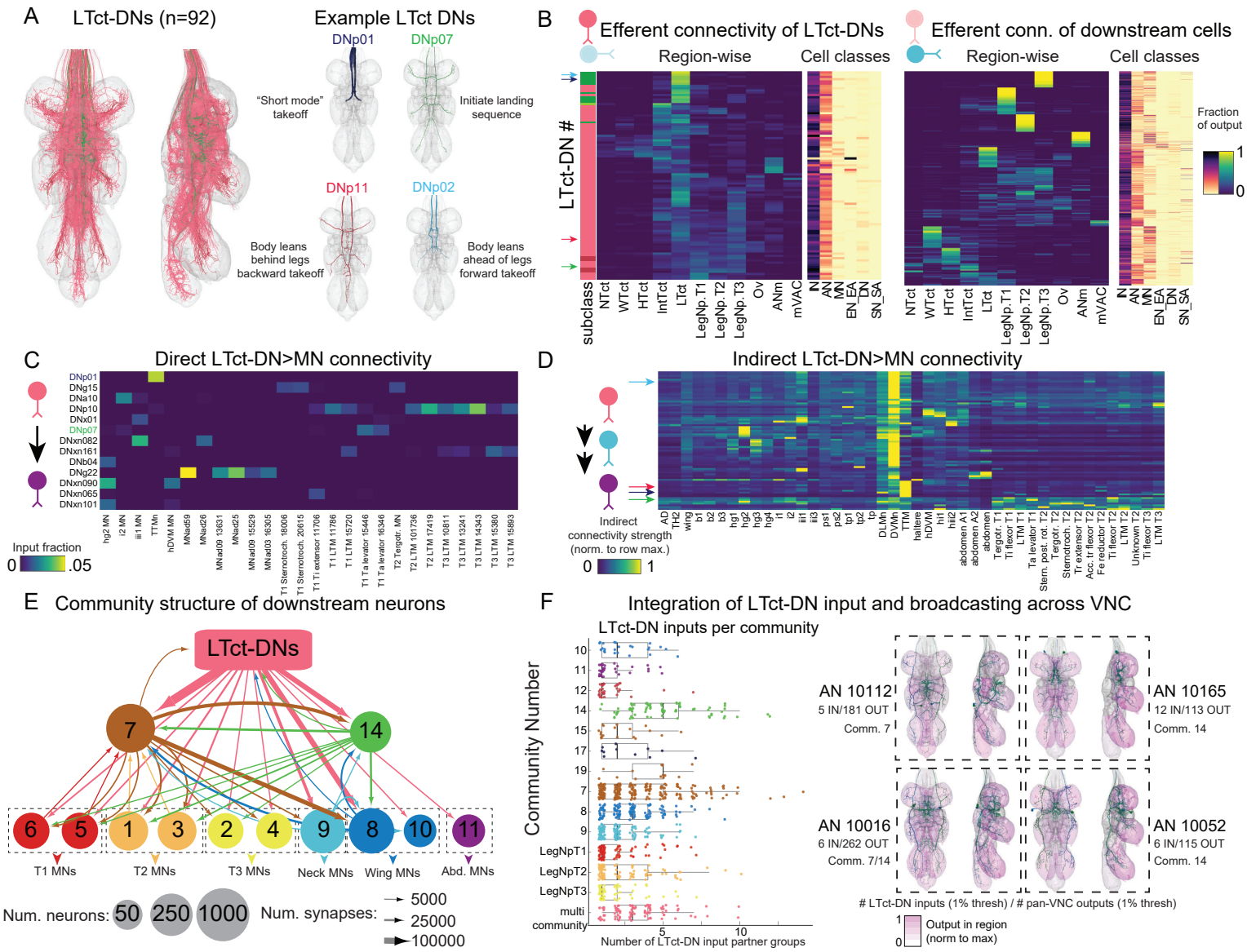

Figure 17: Overview of lower tectulum circuits. A. Left, morphology of the LTct DNs (DN groups with ≥100 synapses and ≥10% of their synaptic output in the lower tectulum). Color corresponds to DN types as in Fig. 3. Right, morphologies of LTct DNs with known behavioral functions. **B.** Left: Efferent connectivity of LTct DNs. Left sidebar, subclass of LTct DNs (e.g. xl, xn, lt), with colors as in A (left panel). Colored arrows left of sidebar indicate rows that correspond to examples in A (right panel). Left heatmap: Proportion of each LTct DN's output in each region of the VNC. Right heatmap: Proportion of LTct DN's output (synapse-wise), onto each downstream cell class (counting only neurons receiving ≥1% of their synaptic input, minimum 50 synapses, from an LTct DN). Right: as on the left side, but each row corresponds to one AN, IN, or EN downstream of an LTct DN ("LTct DN downstream neurons", same connectivity criteria as above). **C.** Heatmap depicting all direct connections between LTct DNs and MNs (groupwise). Any DNs that do not provide ≥1% synaptic input to a MN and any MNs that do not receive ≥1% synaptic input from an LTct DN were excluded. **D.** Heatmap depicting normalized indirect synaptic connectivity (as in Fig. 6G) from each LTct DN onto all MNs within five downstream layers. Any DNs that do not have an indirect connectivity score ≥5 onto any MN and any MNs that do not receive indirect connectivity ≥5 from any LTct DN were excluded. For visualization, all heatmap values are re-normalized based on row-wise maxima. Colored arrows indicate rows corresponding to examples in A. **E** Network diagram depicting connectivity between neurons directly downstream of LTct DNs (same subset as in right panels of B), binned according to the Infomap community they were assigned to (see Fig. 9). Minimum connectivity to display an edge is 5000 synapses, and communities with fewer than 60 LTct DN downstream members are not displayed. **F** Communities 7 and 14 receive high levels of LTct DN input, and contain members that broadcast information across the VNC. Left, Number of LTct DN input partners (neurons providing ≥1% of synaptic input) per downstream neuron, segregated by community assignment on the y-axis. Right, examples of neurons from communities 7 and 14 that receive high levels of LTct DN input (≥1% of input from ≥5 LTct DNs) and project widely throughout the VNC. Regions in diagrams are colored according to the amount of output they receive from the depicted neuron (normalized to the region with the highest output). Text: number of inputs from LTct DNs to each example neuron, number of outputs to all neurons in the VNC (≥1% threshold), community membership.

a role in coordinating behavior across multiple motor systems and neuropils (Figure 17E). Among the LTct DN Downstream cells assigned to communities 7 or 14, we identified many neurons of interest (Figure 17F) that both received high levels of LTct DN input and output broadly throughout the VNC. Several of these neurons are shown in Figure 17F and are followed up on in section 2.7.3. In particular we identified a set of ascending neurons (ANs) with high LTct input and broad output. Taken together, these findings suggest that LTct DN do not rely solely upon direct outputs to neuropils containing wing or leg MNs to coordinate simultaneous leg and wing movements, but instead control them indirectly through multisynaptic motifs such as the broadly-projecting intermediates observed here and the recurrent triad motifs identified in Figure 9G, H.

To examine how the general LTct organization we describe above may guide coordinated behavior, we next focused on a previously hypothesized behavioral role for LTct circuits: coordination of visually-induced escape-related behaviors (Namiki et al., 2018). In the next two sections, we look at LTct circuits specifically connected to DNs implicated in the two known types of escape takeoff: short mode (section 2.7.2) and long mode (section 2.7.3).

2.7.2 LTct circuits modulating Giant Fiber-mediated escape

One of the most important actions a fly must take is to respond to the threat of an approaching predator. When a predator, such as a damselfly, attacks, its image grows rapidly in size on the fly's retina, creating a 'looming stimulus' to which flies react rapidly. These rapid responses can take the form of several behaviors: the fly might turn away from the stimulus, back up, or start walking, or, if the looming signal is fast enough, then most often the fly performs an escape takeoff. Takeoff requires coordination of the T2 legs to extend rapidly in a takeoff jump and the wings to either raise up then perform the first down stroke of flight (in a 'long mode' takeoff) or be pulled down in a 'tuck' against the fly's body (in a 'short mode' takeoff). Functional studies have determined that a single action potential in a pair of large-axon descending neurons called the Giant Fibers (GFs; also known as DNp01) triggers the short mode takeoff 'tuck' and jump. The GFs have non-branching blunt terminals that end in the LTct and provide both chemical and electrical synaptic input onto downstream LTct neurons, including the tergotrochanter muscle motor neuron (TTMn) and the peripherally synapsing interneuron (PSI) (Fig. 19). As mentioned earlier, the TTM is an extrinsic muscle of the leg, which attaches across the thorax parallel to the DVM flight muscles. When stimulated by its single excitatory MN, the TTMn, the TTM rapidly extends the fly's mesothoracic (T2) legs, causing the fly to push off from the ground. In turn, stimulation of the PSI activates downstream MNs controlling the dorsolateral indirect wing power muscles (DLMns), which function as wing depressors. Simultaneous activation of both via the Giant Fiber thus causes the fly to "tuck" its wings and leap into the air. This short-mode takeoff allows flies to get away from a rapidly approaching threat, but the resulting flight is unstable because they do not raise their wings before takeoff (von Reyn et al., 2014; Wyman et al., 1984).The Giant Fiber circuit is one of the best-studied motor networks in the Dipteran VNC, and its downstream and secondary output connectivity is well-documented by previous EM and dye-fill studies (Azevedo et al., 2022; Bacon and Strausfeld, 1986; Kennedy and Broadie, 2018;

King and Wyman, 1980; Sun and Wyman, 1997). We validated this known GF connectivity in MANC and then, in addition, were able to identify further components of the GF circuit, including a set of neurons that make strong, direct inputs to the GF axon within the VNC (Figure 18A, B).

Since a single action potential is sufficient to initiate a short-mode takeoff, yet high-velocity escape disrupts ongoing behavior and requires a large amount of energy, it is presumed that the GF is under strong regulation, for example by presynaptic inhibition. Indeed, we identified upstream circuits of the GF within the VNC that are likely to influence its output by enhancing or curtailing spike propagation along its axon. The GF receives a lot of axo-axonal input in the VNC. Of the 470 DN groups in the MANC volume, the GF is among the 20 which receive 4000 or more synaptic inputs from VNC neurons. We identified a set of neurons that provide especially strong input to the GF (≥1% the GF's synaptic input) and organized them based on their connectivity and morphology. Some of these cells, including groups 12983, 17558, and 22805, synapse onto the terminal of the GF (Figure 18C). Depending on whether these neurons are excitatory or inhibitory (most still have neurotransmitter undetermined by the prediction algorithm, though all high-confidence predictions are GABAergic), these INs might be capable of either blocking or directly triggering a short-mode takeoff. Other neurons synapse at locations distal to the GF terminal. Group 16900, for instance, comprises a group of eight ANs which synapse almost exclusively onto each other as well as the rostral regions of the GF axon; they also receive synaptic input from the GF (Figure 18A-C). Their recurrent co-activation might modulate the propagation of GF spikes.

We also identified circuits that putatively enable descending control of GF activity (Figure 18B). For example, group 18987 contains six cells that collectively receive strong input (≥1% groupwise synaptic input) from ten DNs. These cells output heavily onto the GABAergic IN 12983 that itself targets the GF terminal directly (Figure 18B, C).

We also identified neurons downstream of the GF that, in addition to the TTMn and PSI, may be important for actuating aspects of short-mode takeoffs (Figure 18D). Several of these neurons–GFC1, GFC2, GFC3, and GFC4–were previously identified and shown to be gap-junction coupled to the GF using dye-fill experiments (Kennedy and Broadie, 2018). GFC2 synapses onto the TTMn, the DLMn, and to the ps1 indirect control MN according to previous connectomic analysis (Azevedo et al., 2022). We identified several groups within the MANC dataset with morphologies similar to GFC2 (Figure 18E). The total number of these neurons (11) was close to the total number of GFC2 neurons estimated previously using light microscopy (7 bilateral pairs; (Kennedy and Broadie, 2018). These groups exhibit slight morphological variability and differential downstream connectivity, suggesting that they are not a homogenous population. We labeled the only group that made significant outputs onto the TTMn (as previously observed in Azevedo et al., 2022) "GFC2" and refer to the other groups as "GFC2-like."

We confirmed prior connectome observations that the GFC4 neuron is likely involved in post-takeoff leg flexion (Azevedo et al., 2022) and further observe in MANC that GFC1 and GFC3 might serve similar roles. These neurons each contact tibia flexors in one or more legs

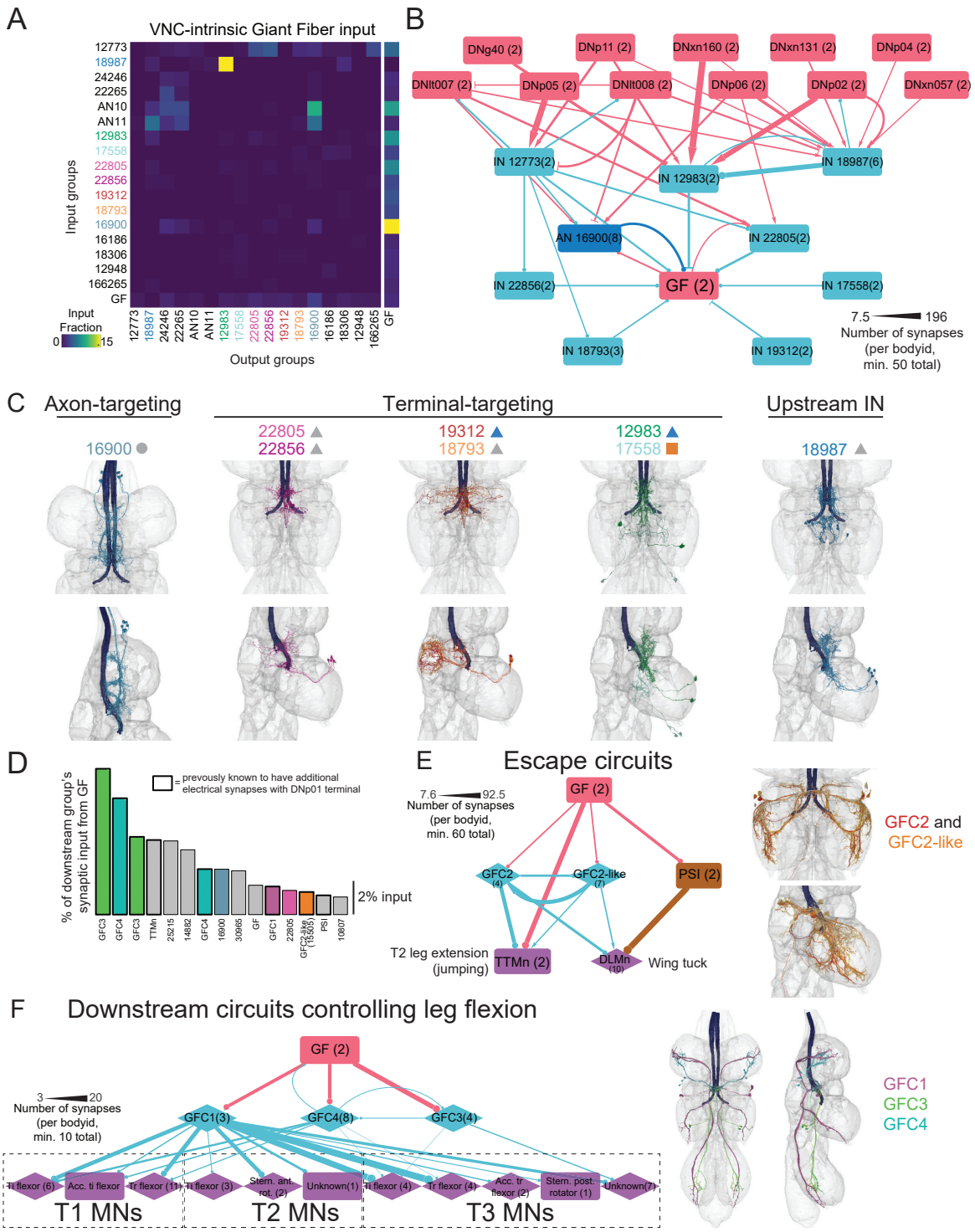

Figure 18: Upstream and downstream circuits of the Giant Fiber in the VNC. A. Heatmap showing synaptic connectivity between the 17 groups that provide at least 1% of the Giant Fiber's VNC-intrinsic synaptic input as well as 18987, a group of important second-order inputs. Connectivity is expressed as the fraction of the postsynaptic cell's total synaptic input (groupwise). **B.** Network diagram depicting connectivity of groups from A as well as their inputs from DNs. **C.** Morphology of GF-targeting ANs and INs. Top row shows morphology from a ventral perspective and bottom row shows morphology from left side of VNC. Left, morphology of the axon-targeting group 16900. Middle, six groups of terminal-targeting INs divided into three types based on morphological criteria. Right, morphology of 18987. The axons of the GF are shown in indigo in each image. Symbols next to neuron names indicate putative neurotransmitter identity: circle corresponds to a cholinergic prediction, triangle to a GABAergic prediction, and square to a Glutamatergic prediction. Grey symbols indicate that neurotransmitter prediction is low confidence (prediction value<0.7). **D.** Major synaptic outputs of the GF. Synaptic output is plotted as the % of the downstream group's synaptic input that is provided by the GF. Only neurons that provide at least 1% of input are shown (min. 30 synapses). Neurons with known electrical connectivity to the GF are shown in dark boxes. **E.** Left, network diagram depicting direct and indirect connectivity between GF and two downstream partners that trigger takeoff behaviors: the TTMns, which trigger jumping, and DLMns, which initiate wing tuck or downstroke. Right, morphologies of the GFC2 and GFC2-like groups. **F.** Left, network diagram depicting connectivity between GF and downstream partners that putatively control post-takeoff leg flexion. All three INs contact tibia flexor MNs and tarsal flexor MNs, although they vary in their other targets and in which neuromeres they project to. Right, morphologies of the GFC1, GFC3, and GFC4 groups.

but vary in their projection pattern, implying that they each control flexion in different sets of leg pairs (Figure 18F). In addition to its strong outputs onto tibia flexors, GFC1 contacts other MN types, such as sternal anterior rotators in T2, that are likely to contribute to proper leg positioning during flight.

Previous work suggested that selection of long-mode vs. short-mode takeoff could be driven purely by a spike-timing mechanism: if a single GF action potential preceded activity in other DNs that evoke long-mode takeoffs, the fly would “tuck and jump” (von Reyn et al., 2014). The MANC data reveal that the GF axon is itself regulated by presynaptic inputs that may initiate, amplify, or prevent spiking, implying that state-based inputs and other descending pathways could also play a role in shaping takeoff action selection (for example, by “vetoing” an earlier GF action potential). If GF action potentials are able to propagate to the terminal, they initiate short-mode takeoffs by activating canonical downstream elements including the PSI and the TTMn. In addition, they activate an intermediate layer of premotor neurons that either amplify these actions (i.e. GFC2, GFC2-like) or coordinate more complex and slower-latency movements (i.e. GFC1, GFC3, GFC4) such as leg flexion after jump.

2.7.3 LTct circuits that may control long-mode takeoffs

Instead of the “short mode” takeoff, flies can respond to looming stimuli by performing a “long-mode” takeoff, in which downstroke and leg extension are preceded by wing raising (Figure 19A) (Card and Dickinson, 2008; Trimarchi and Schneiderman, 1995; von Reyn et al., 2014). While this sequence takes more time to complete, long-mode takeoffs initiate more stable flight. The VNC circuits underlying long-mode takeoffs remain enigmatic, but many of the important downstream motor outputs have been identified (Figure 19A). TTMn and DLMn are likely to be utilized, respectively, for jumps and downstrokes. Wing raising likely involves activation of MNs innervating several muscle groups, including the DVM wing levator muscles, the basalar muscles (which are active prior to flight, possibly to reconfigure the wing hinge), and the tergopleural muscles (which evoke wing raising when driven and are necessary for voluntary takeoffs) (Dickinson and Tu, 1997; O’Sullivan et al., 2018). In contrast to short-mode takeoff, functional evidence suggests that GF activity is dispensable for long-mode takeoffs (Card and Dickinson, 2008; Trimarchi and Schneiderman, 1995; von Reyn et al., 2014). Thus activity in other DNs must be sufficient to produce long-mode takeoffs.

We have previously identified a number of DNs which are likely to contribute to long-mode takeoffs based either on anatomical evidence that they are downstream of neurons important for looming detection or functional evidence that they initiate long-mode takeoffs when optogenetically stimulated (Dombrovski et al., 2023; Peek, 2018; Williamson et al., 2018). This subset of DNs (which includes DNp11, DNp02, DNp04, and DNp06) are all LTct DNs, suggesting that local circuits in the LTct are important for long mode takeoff coordination. We also thus expect that other LTct-targeting DNs, beyond those already identified, may also be involved in coordinating long-mode takeoffs.

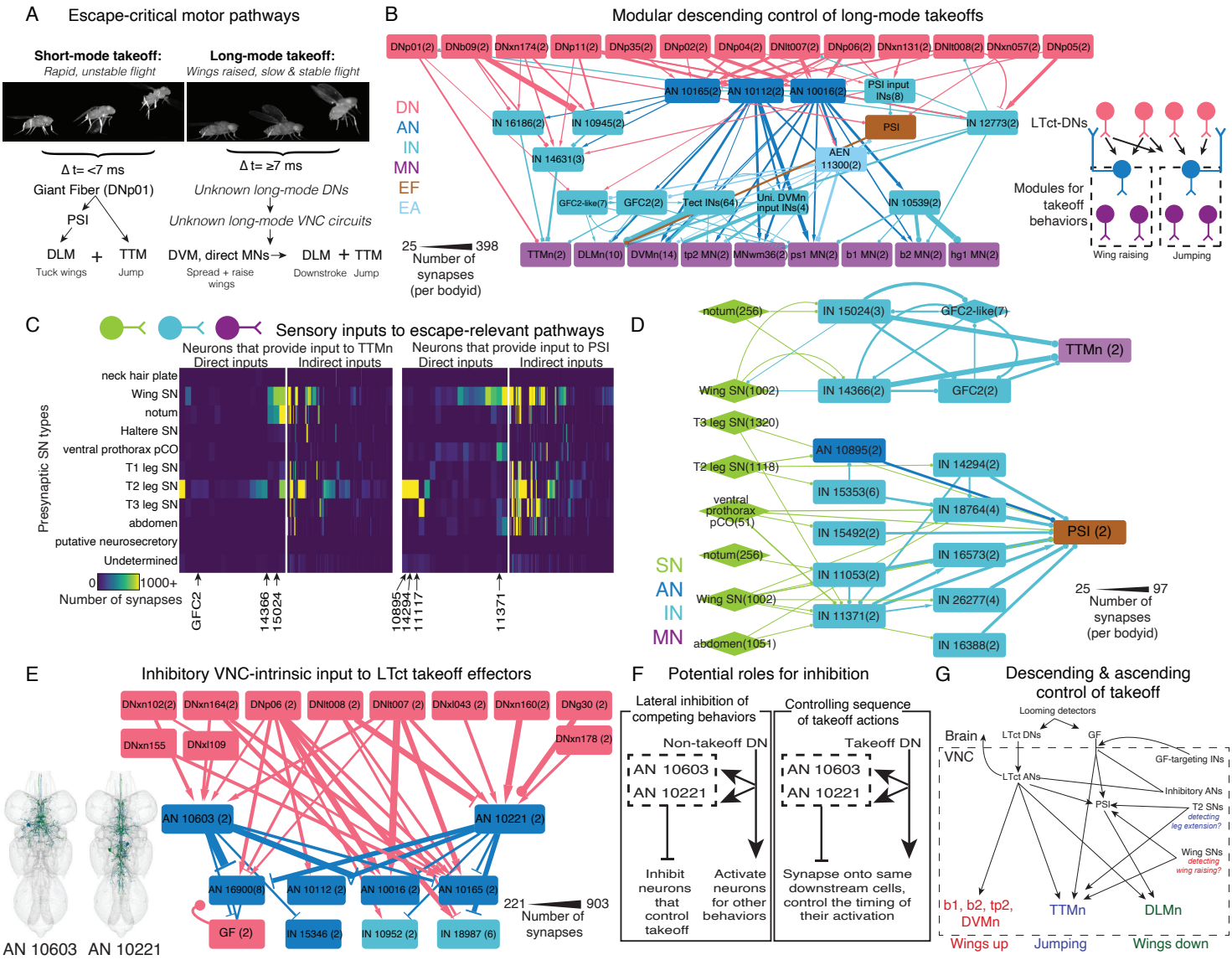

Figure 19: Circuits mediating escape takeoff. A. Schematic of differences between short-mode and long-mode takeoffs, including the characteristic patterns of motor activity, the durations of the behaviors, and the neurons known or hypothesized to be involved in each. **B.** Connectivity diagram depicting strong descending connectivity onto MNs critical for long-mode takeoffs. For clarity, several groups are combined into larger categories based on shared connectivity: the "GFC2-like" node contains groups 14527, 13479, and 15505, the "Uni. DVMn input INs" node contains 17159 and 16088, and the "Descending PSI input INs" node contains 15486, 15492, and 17220. MNs are grouped according to their target muscle. All other nodes contain bodyids with a shared group number. Right inset: model of how LTct DN input converges onto a subset of effectors that are each responsible for initiating particular patterns of behavior. **C.** Connectivity between SNs and escape-relevant INs and MNs. Left, heatmap depicting connectivity from SNs onto neurons directly presynaptic to TTMn (left panel) and neurons 2 hops upstream (right panel). Connectivity is determined by a 1% input and 25 synapse threshold (groupwise). Rows are grouped by subclass, with related subclasses combined based on the body parts in which they originated (e.g. wing CS SNs and wing margin bristle SNs are both included in the "Wing SN" category). Columns from neurons of interest are labeled with arrows. Right, as above but for neurons one or two hops upstream of the PSI. **D.** Diagram showing strong synaptic connectivity between SNs, neurons of interest (including a subset labeled in C), and the TTMn (top) or PSI (bottom). **E.** Connectivity diagram of DNs upstream of AN 10603 and AN 10221 and their strongest postsynaptic targets. In order to be included on this diagram, presynaptic neurons must be DNs that provide at least 1% of synaptic input to either AN 10603 or AN 10221. Post synaptic neurons must receive at least 1% of their input and at least 150 synapses (groupwise) from either AN 10603 or AN 10221. **F.** Diagram depicting two possible models for the functions of AN 10603 and AN 10221. **G.** Diagram demonstrating how actions important for both short-mode and long-mode takeoffs could be coordinated by DNs, local neurons in the VNC, and information from SNs.

How do LTct DNs coordinate activity in these critical escape effectors to initiate long-mode takeoffs? Previously, we observed that the outputs of LTct DNs often converge onto ascending neurons (ANs) assigned to communities 7 or 14 (see above, Figure 17E, F), such as AN 10112, AN 10016, and AN 10165, which themselves provide some of their strongest outputs to DLMns, DVMns, TTMn, and the PSI, as well as several MNs innervating direct control wing muscles (Figure 19B). These three ANs are all predicted to be cholinergic and hence excitatory. This disynaptic circuit motif (DN-AN-MN) thus represents the most direct connectivity between long-mode-associated LTct DNs and MNs implicated in takeoff. While these ANs all receive converging inputs from the takeoff-related DN subset, their outputs are more distinct. This suggests a model in which a population of DNs are each activated by threatening visual stimuli and their outputs in the VNC are integrated by these cells, each of which coordinates a specific part of the motor pattern critical to takeoff. We next looked at the connectivity of these ANs in more detail(Figure 17F, Figure 19B).

AN 10016 provides strong input (≥1% of total synaptic input) to over 250 other neurons in the VNC, including wing MNs (MNwm36, tp2, b2, ps1, DVMn), intrinsic neurons with outputs in single leg neuropils (e.g., groups 12281, 12324, 13334), intrinsic neurons that span multiple leg neuropils (e.g. groups 10273, 11856, 10941), and abdominal MNs. The intrinsic neuron that receives the most input from AN 10016, IN 10539, also projects to multiple wing MNs including hg1, hg3, hg4, b2, iii4, and ps1 MNs. Many of these downstream neurons are involved in escape; for example, tp2, b2, and the DVMs are implicated in the processes of wing raising and flight initiation (Dickinson and Tu, 1997; O'Sullivan et al., 2018). AN 10016 also synapses extensively on 11300, a putatively glutamatergic ascending efferent which outputs to both the PSI and the DLMns. Therefore, one of AN 10016's functions might be to suppress wing depression while directly activating neurons involved in wing raising.

AN 10112 has strong bilateral outputs to wing MNs of multiple classes, including the ps1 MNs, MNwm36, the b2 MNs, and the DVMns and DLMns. In addition, the AN 10112s provide further input to intrinsic neurons which themselves directly contact wing MNs including the Tect INs (see section 2.6), IN 17159, IN 16088, IN 11652, and IN 14460. The strong overlap in connectivity between AN 10112 and the Tect INs implicated in flight control suggests that this AN might be involved in initiating the flight motor system after takeoff.

AN 10165 devotes most of its axonal projections to the leg neuropils (Figure 17F). In the LTct, AN 10165 contacts three intrinsic neuron groups, IN 10945, IN 16186, and IN 14631, which themselves output to the TTMn both directly and indirectly. All of these cells are predicted to use the neurotransmitter glutamate, meaning that postsynaptic cells might be depolarized or hyperpolarized depending on the type of glutamate receptor they express. However, there is good reason to believe that this network has an excitatory influence on TTMn: DNp11 neurons, which are cholinergic and evoke jumping when activated (Dombrovski et al., 2023), make at least 100 synapses onto two of these three neuron groups (representing the most direct connection between DNp11 and TTMn). Several other DNs (DNb09, DNxn174) make strong outputs onto two or more of these neuron groups, and also presumably initiate jumping when activated.

It remains enigmatic how CNS circuits control the timing of the motor sequences critical to long-mode takeoffs. Two models could explain this action sequencing: either 1) sets of DNs are dedicated to triggering distinct VNC circuits that govern each of these actions and are activated sequentially in the brain, or 2) “long-mode” DNs collectively activate multiple VNC neurons governing takeoff; VNC-intrinsic circuits (including both lateral interactions between descending circuits and ascending sensory feedback) then instruct transitions from one phase of the takeoff sequence to the next.

To substantiate the first model, it would be necessary to identify individual DNs that receive input from looming-sensitive neurons in the brain and initiate only a single action from the suite of motions necessary for takeoff. These DNs would have substantial synaptic influence on the motor pathways associated with one action, but not others. We did identify some DNs which may fit these criteria. For instance, DNb09 and DNxn174 target neurons presynaptic to TTMn without synapsing onto neurons presynaptic to wing MNs (see above) and would presumably initiate jumping with limited wing movement when activated on their own (Figure 19B). Since it is uncommon for *Drosophila* to leap without any wing movement in response to looming stimuli, these DNs may be activated in coordination with other DNs responsible for initiating the other actions associated with long-mode takeoffs.

Notably, however, the majority of LTct DNs which are likely to contribute to long-mode takeoffs exhibit efferent connectivity patterns which are likely to influence activity in multiple escape-related effectors including the direct wing MNs, the indirect wing MNs, and the TTMn (Figure 19B). For example, DNp02, DNp04, DNp06, and DNp11 have secondary and tertiary synaptic connectivity to all of the MNs listed above. Furthermore, flies that take off after optogenetic activation of these DNs perform full long-mode takeoff sequences (Dombrovski et al., 2023) rather than individual actions.

In support of a model in which local interactions within the VNC pattern instruct the sequencing of takeoff behavior, we discovered evidence that sensory neurons from the wings and legs synapse onto intrinsic neurons presynaptic to escape effectors (Figure 19C, D). This suggests that sensory input might influence the progression of activity in VNC escape circuits. SNs from the notum and the wing, including campaniform sensilla neurons which could detect wing deformation, synapse onto groups 14366 and 15024 (Figure 19C, D). These INs have direct synaptic input to the TTMn and also activate several other intrinsic neuron groups presynaptic to the “jump” MN, including the GFC2 and GFC2-like neurons (Figure 19D). In addition to receiving input from the GF, GFC2 and GFC2-like neurons receive descending inputs from other looming-sensitive DNs (such as DNp06) and other neurons associated with takeoffs (such as AN 10112, Figure 19B).

The GFC2 cells are not the only neurons implicated in takeoff initiation that receive strong afferent inputs from both SNs and DNs. AN 10112, for example, receives extensive monosynaptic inputs from wing SNs. The PSI receives both disynaptic and trisynaptic input from SNs via several groups of INs (Figure 19C, D). While some of these INs are sensitive to only a

single sensory modality, others are predicted to bind input from multiple types of SNs, or from groups of INs that receive input from SN types spanning two or more modalities. We hypothesize that AN 10112, PSI, and GFC2 serve as sites for the convergence of descending and ascending information streams, and that these two types of inputs may interact with one another. For example, descending input might modulate ascending sensory pathways, rendering these behavioral effectors more sensitive to cues such as wing raising after activation by LTct DNs.

What is the role of this sensory information? Some sensory pathways might bypass the central brain to trigger escape circuits directly, minimizing response latency to threats that are close enough to touch the fly. These sensory streams may also be tuned to sensations important to checkpoints in the takeoff process; for example, sensory inputs from the T2 leg could detect the initiation of a jump and trigger activity in the PSI, initiating a downstroke. Wing campaniform sensilla SNs could also detect wing deformation and initiate downstroke or jumping through the pathways described above. Consistent with this hypothesis, we have previously observed that the timing of certain motor subprograms within the long-mode takeoff sequences are always tightly coupled. For example, the initiation of the jump and the downstroke almost always occur with very short latency after the completion of wing raising (von Reyn et al., 2014), unpublished data).

A number of LTct neurons which are likely to be involved in coordinating takeoffs are also governed by inhibitory ANs. Two GABAergic ANs, AN 10603 and AN 10221, target IN 18987, AN 16900, AN 10016, and AN 10165; AN 10221 also synapses onto AN 10112 and AN 10603 inhibits the GF (Figure 19E, Figure 18A). These ANs might serve either as a persistent “brake” to prevent any takeoffs in particular behavioral contexts or as a “switch” by which one behavioral program might laterally inhibit others that would normally evoke takeoffs (Figure 19F). Alternatively, these neurons might have a role in instructing normal takeoff sequences by providing temporally precise inhibition of takeoff-related behavioral modules. Consistent with these many possible roles, AN 10603 and AN 10221 receive many diverse non-overlapping inputs. This afferent connectivity includes both DNs that do and others that do not also synapse onto some of the targets of AN 10603 and AN 10221 (Figure 19E).

2.7.3 Circuits for the flexible coordination of takeoffs

In summary, we identified synaptic pathways explaining how flies are able to perform coordinated movements of their wings and legs such as long-mode takeoffs (Figure 19G). We discovered that this coordination rarely emerges from monosynaptic connections between DNs and MNs, which would imply action sequencing occurs solely in the brain, but instead relies upon VNC-intrinsic nodes that have both a high input and a high output degree. These neurons are likely to pool input from a population of DNs that are activated by similar kinds of threatening features. They then synapse across multiple neuropils in the VNC to drive coordinated behaviors. Many of these neurons are ANs and, as such, also send projections back to the brain and/or premotor areas such as the sub-esophageal zone. Future connectomic volumes that include more of the central nervous system may elucidate the role of this efferent connectivity. Notably, in *Drosophila* larvae, ascending projections have been shown to synapse in the brain

onto DNs that may be activated sequentially in a behavioral sequence (Winding et al., 2023). It remains to be seen if these, or similar motifs, may play a role in the coordination of long-mode takeoffs.

Our analysis suggested that SNs, like ANs, play an outsized role in the control of behavior. Many VNC neurons, including a number that likely influence the activity of takeoff-critical MNs, received strong afferents from both sensory and descending input. We hypothesize that this convergence is critical for establishing precisely timed action sequences.

Finally, our analysis identifies VNC neurons that are poised to gate expression of takeoff behaviors. We identified two ANs, AN 10603 and AN 10221, that broadly inhibit many neurons that we believe to be important for long-mode takeoffs. We also observed a number of INs that directly target the axon of the GF, presumably exerting a strong influence on the successful propagation of GF spikes (and, therefore, the initiation of short-mode takeoffs in response to threats). These inhibitory motifs may be the substrate for enforcing reciprocal inhibition between different action pathways, ensuring that only a single movement is carried out during action selection, or they may be elements required to maintain the correct timing and sequencing of behavioral submodules in a complex action sequence like takeoff. Future functional studies are required to test these hypotheses and further flesh out how connectivity patterns in the VNC contribute to the motor control of the fly's wide range of behaviors.

3 Discussion

Within the last decade, the accelerated development of EM connectomics methods has greatly improved our ability to probe the organization and function of neural circuits. The densely-reconstructed connectivity of the Hemibrain connectome allowed researchers to carry out large-scale and open-ended interrogation of brain circuits, and we expect that the release of MANC will similarly stimulate inquiry into nerve cord circuits. To begin describing and understanding the connectivity from brain to VNC and motor output, we have systematically reconstructed, cataloged and annotated all DNs and MNs of the VNC, and identified 29% of DNs and 55% of MNs. While many DN and MN types in MANC are as-yet unidentified at the light level, the availability of their EM morphology will expedite neurobiologists' attempts to target and characterize them through tools such as color depth MIP mask search (Otsuna et al., 2018) and NBLAST (Costa et al., 2016). Using the densely-reconstructed MANC connectivity (Takemura et al., 2023), as well as the rich layer of annotations and metadata (Marin et al., 2023), we examined descending input-to-motor output connectivity broadly across the VNC as well as specifically in wing, leg and lower tectulum neuropils and circuits.

Our annotation and reconstruction of neurons passing through the neck connective reveal a DN cell count of 1328, greater than prior estimates that range from 700 to 1100 cells (Hsu and Bhandawat, 2016; Namiki et al., 2018), and comparable to the ascending neuron count of 1864, indicating that information flow between the brain and VNC is bidirectional. In contrast, we found and annotated 737 MNs in MANC (roughly half of DN count), setting an approximate upper limit

on the number of motor units found across the fly's motor systems, and indicating that descending information converges on MNs and their upstream circuits to determine motor output. Overall, roughly 80% of MN groups receive direct input from at least one DN group at a 1% input threshold, although total direct DN input to most MNs remains fairly low (<10% of their input synapses), with a few major outliers. Most prominently, DN input contributes up to ~60% of the total upstream synapse count of the neck MNs and a subset of abdominal MNs. The neck motor control system in flies is split between MNs located in the brain and the VNC (Strausfeld et al., 1987). Thus, it is plausible that many VNC neck MNs are under strong direct DN control to coordinate their action with neck MNs located in the brain–however, the neural circuitry underlying the *Drosophila* neck motor system remains largely unexplored. Nevertheless, intrinsic neurons make up the bulk of MN inputs as well as DN downstream targets, and thus most MNs are likely driven indirectly by VNC premotor networks through which DNs act.

To dissect the structure of VNC intrinsic networks, we carried out several methods examining both large- and fine-scale connectivity in these networks. Infomap partitioning of VNC circuits suggests that VNC premotor circuits have a modular structure with individual communities dedicated to controlling specific sets of MNs. Each leg hemisegment receives output from a single community, while upper tectular motor systems are more mixed, with several controlling both wing and haltere MNs, as well as a single community controlling neck muscles. Within the communities controlling the wing MNs, we further find subsets that are each specialized in controlling the steering and power MNs (with mixed output to the indirect control MNs), and DNs targeting the wing neuropil are likewise biased in their connectivity with these communities. This organization stands in contrast to leg communities, where leg neuropil-restricted neurons form a single community in each hemisegment, and the serially-repeating structure of leg control circuits allowed us to generate a single 'standard leg connectome' representing connectivity of restricted neurons in each leg hemisegment. Interestingly, Infomap community detection also suggested the presence of several communities in the intermediate layers of the VNC with low direct MN output—neurons of these communities commonly have input and output in the intermediate neuropils but also often cross neuropil boundaries to arborize widely in the VNC. These communities may thus serve as 'higher order' behavioral control centers through their connectivity with other communities. We explored the connectivity of two such communities which receive strong input from DNs targeting the lower tectulum (LTct). A significant fraction of LTct DNs are implicated in controlling escape takeoff, and we examined connectivity within these communities to identify circuit motifs that we hypothesize play roles in mediating takeoff motor actions, as well as action selection between two modes of escape takeoff. However, as most LTct-targeting DNs have not been behaviorally categorized, it is possible that the function of these communities in behavior may extend beyond escape alone.

Precision in leg kinematic control is thought to generally occur through the use of multiple motor units controlling the same joint movement that are innervated by MN sets that follow a size recruitment principle (Azevedo et al., 2020). That is, each set of muscles receive input from a hierarchy of MNs with different activation thresholds, where the MNs that have the lowest activation threshold also control the muscles which exert the least force. Indeed, in MANC, we find that many, but not all, MNs of different serial groups that control the same joint motion share

a large fraction of upstream partners by cosine similarity, showing that the associated muscles are likely under command of similar motor control signals and may differ mainly by their activation thresholds. Unlike the legs, the wing muscular system is functionally separated into two systems that separately control power generation and steering—and the upstream circuits and DNs are likewise partitioned. While the wing power generation system and its circuit arrangement has no direct leg analogs, the wing steering system has some potential parallels to the leg muscle system. Many wing steering muscles that control each sclerite of the wing hinge share common tendons and may conceivably act as motor units to differentially control force exertion, while some others with separate tendons can exert similar or different action on a sclerite (Dickinson and Tu, 1997). Indeed, prior work shows differential recruitment of muscles per sclerite depending on the magnitude of turning during flight, reflecting control of force generation for executing wing kinematic changes (Lindsay et al., 2017). This is partially borne out in the connectome: shared upstream connectivity is observed for some (but not all) MNs for muscles of the same sclerite. For example, we find that the tonically active b1 MN and the phasically active b2 MN partially share a high degree of upstream DN input and likely electrical input from w-cHINs, upon which DNs and haltere campaniform afferents converge. It is likely that depending on connectivity strength and activation threshold of the MNs, the same descending steering signals may shift the activation phase of the b1 MN in the wingbeat cycle during lower magnitude turns, and further activate the b2 MN during higher magnitude turns.

Population calcium imaging of supraesophageal DNs in spontaneously walking and behaving flies suggest that 60% of imaged DNs encode walking, likely encoding turning and to a lesser extent, speed. It was surmised that activity in these DNs more likely represented high-level behavior rather than low-level kinematic control (Aymanns et al., 2022). We describe 177 leg DNs and their leg MN connectivity with some detailed examples of DN circuits involved in turning and backwards walking. However, predicting the function of single or groups of DNs in the VNC required a deeper understanding of the serially repeated leg circuits, which we addressed in the form of the standard leg connectome. The number of intrinsic neurons dedicated to the single leg neuropils (Marin et al., 2023) reflects the complexity of a potential leg central pattern generator (CPG) that must continually adapt to environmental stimuli, spanning from the unevenness of the ground to the presence of a predator. With the exception of the DNfl neurons, which we hypothesize to be involved in behaviors such as grooming or reaching, most leg DNs extend their axons to all three leg neuropils within a single hemisphere of the VNC. Downstream of these DNs, we found a high proportion of serially repeated neurons restricted to single leg neuropils. This type of modulation from DNs requires a strong coordination between the leg neuropils. Our analysis of interconnecting neurons upstream of the standard leg connectomes allows us to compare our putative premotor circuits to previous predictions for six-legged walking in *Drosophila* (Bidaye et al., 2018; DeAngelis et al., 2019). Based on existing locomotor models, we expected that a large proportion of inhibitory neurons would control posterior-anterior and inter-hemisphere inhibition between and across distinct leg neuropils. Instead, we found that most inhibitory neurons target all leg neuropils in one or both hemispheres. Again contrary to previous predictions, we do not see a strong bilateral connection between neurons in the T2 leg neuropils. While we found serial sets of neurons that project both from the posterior to the anterior, as predicted, we also found anterior to posterior

projections within the same hemisphere, which are exclusively excitatory. These results provide a platform for detailed investigation of potential inter- and intra-leg CPGs upstream of the leg motor neurons and the modulatory input of different DNs on these circuits. They also suggest that leg CPGs may primarily operate at the level of single legs synchronized through numerically much weaker inter-leg connections.

While DNs are mainly thought of as providing information output within the VNC, most MANC DNs receive axonal synapse inputs at a mean of ~11:1 output-to-input ratio, suggesting that local VNC circuits play an active role in the regulation of DN output. Some DNs, such as the Giant Fiber (GF) receive more substantial VNC input. Activation of the GF is both necessary and sufficient for the initiation of a particular type of escape behavior (the short mode takeoff, see. Fig. 19) (von Reyn et al., 2014; Wyman et al., 1984). The local VNC input to this DN contains many putative inhibitory neurons that are under the regulation of other LTct-innervating DNs, and receive input from LTct DNs that are involved in executing another type of escape behavior (long-mode takeoffs), thus raising the hypothesis that this circuit participates in action selection by directly modulating GF excitability (Fig. 18). This example illustrates one mechanism by which VNC circuits could play a role in behavioral choices by integrating local computations with descending information.

Although the connectome does not allow direct assessment of electrical synapse connectivity, we made efforts to indirectly find and annotate putative electrical neurons throughout the VNC. Importantly, putative electrical neurons appear common in the upper tectulum (and part of the leg neuropils), and may be crucial to the interpretation of neck, wing and haltere circuitry. Indeed, prior findings show that the innexin ShakB (a protein important for the structure of gap junctions) is highly prevalent in the medial VNC, haltere afferent tracts and sections of the leg neuropils (Ammer et al., 2022). The prevalence of electrical synapses will pose a challenge for interpreting upper tectulum circuit connectivity, and additional work may be required to elucidate and characterize electrical synapse connectivity in the VNC. For example, serial-section transmission EM in osmium-fixed CNSes combined with immunogold labeling (Ando et al., 2016; Shahidi et al., 2015) potentially allows labeling of gap junction proteins in CNS EM volumes for the creation of an ‘electrical synapse connectome’.

While our analyses presented here gives readers a broad overview of DN-to-MN connectivity and premotor pathways in the VNC as well as specific details on a few key circuits, a comprehensive interpretation of most VNC connectivity remains challenging. The scale of the connectome means that large-scale analyses do not always capture nuances of connectivity, while small-scale circuit examination remains heavily manual. In addition, functional data is still lacking for most VNC cells, which is vital to circuit interpretation. Indeed, by focusing on DNs with available functional data, we were able to better direct our connectome search for pathways likely controlled by these DNs, as well as improve our interpretation of said connectivity. Thus, much future work remains to combine connectomics and experimental approaches for meaningful interpretation of circuits across the VNC. In addition, as is common in EM-based connectomics efforts, our efforts in examining VNC connectivity does not take into account non-synaptic neurotransmitter and neuromodulator release, differences in neuron

physiology, and also makes simplifying assumptions about the equivalence of synapse counts and synapse weights. Thus, we emphasize that the analyses of VNC-wide premotor circuits presented here is mainly a framework in which to aid future hypothesis-driven experimental exploration into VNC function, and perhaps to help define further connectome analysis.

In summary, the *Drosophila* VNC plays a key role in receiving a plethora of descending signals from the brain, where VNC circuits serve to generate patterned motor output, coordinate between different motor systems and potentially play a role in behavioral choice. Our work here in proofreading, curating and identifying DNs and MNs of the VNC lays the groundwork to enable neurobiologists to easily find and examine descending-to-motor pathways of interest.The comprehensive access to VNC connectivity as well as the wealth of neuronal annotations and metadata now empowers neurobiologists to explore VNC circuits and unravel their secrets.

Acknowledgements

We thank the following people for their contributions to this work: Feng Li, Emily Tenshaw, Julie Kovalyak, Christopher Dunne, Griffin Badalamente, and Marina Gkantia for contributions to focused MN or pre-MN proofreading. Erica Ehrhardt for pre-publication sharing of wing and haltere MN light-level data and type information, and discussion/verification of their MANC matches, and Joshua Lillvis for help with wing MN identification. Joshua Lillvis and Kaiyu Wang for pre-publication access to fruitless-positive neuron identifications in MANC. Jonathan Enriquez for providing image stacks of leg MNs and expert evaluation of leg MN identification. Tony Azevedo, John Tuthill, Wei-Chung Lee for generous pre-publication sharing and discussion of T1 leg MN identities and nomenclature in FANC. Ellen Lesser for cross-volume corroboration of wing MN identifications. Mark Eddison, Yisheng He, Jenn Jeter, Gudrun Ihrke, and the Janelia Project Technical Resources team for EASI-FISH. FlyLight team and Alyson Petruncio for standard neurotransmitter FISH work, and Jennifer Jeter and Christina Christoforou for FISH imaging. Janelia FlyLight Project Team and Janelia Project Technical Resources for screening split-Gal4 combinations for wing MNs. Hideo Otsuna for producing color maximum intensity projections of all MANC neurons and making available EM color MIP match search of MANC neurons on the neuronbridge preprint server. This work was supported by Wellcome Trust collaborative awards 220343/Z/20/Z and 221300/Z/20/Z to GSXEJ and GMC, GM Rubin, S Waddell and M Landgraf; by the Howard Hughes Medical Institute (GMC, FlyEM project team); core support from the MRC (MC-U105188491) to GSXEJ; a Walter Benjamin DFG fellowship to TS.

Supplementary Files

Supplementary file 1: DN typing, tracts and light-level matching in MANC

Supplementary file 2: MN and efferent light-level matching in MANC

Supplementary file 3: MANC intrinsic neuron Infomap community assignments

Supplementary file 4: Putative electrical neuron groups by presynaptic site count over volume

Table 1: Dipteran steering muscle function. Activity of steering muscles in *Drosophila* and other dipterans during turning in flight on the ipsilateral (inner side of turn) vs contralateral (outer side of turn) sides. Evidence compiled from (Egelhaaf, 1989; Heide, 1975; Heide and Götz, 1996; Lehmann and Götz, 1996; Lindsay et al., 2017; Nachtigall and Wilson, 1967). The iii2 muscle, which is not present in *Drosophila,* is omitted.

Muscle	Evidence type	Activity during flight	Activity during turning	
			Ipsilateral	Contralateral
b1	Electrophysiology, calcium imaging	Tonic	Phase delay	Phase advance
b2	Electrophysiology, calcium imaging	Phasic	Inactive	Active
b3	Calcium imaging	Tonic	Activity increased	Activity decreased
i1	Electrophysiology, calcium imaging	Phasic	Active	Inactive
i2	Calcium imaging	Tonic	Active/minor change	Active/minor change
iii1	Electrophysiology, calcium imaging	Phasic	Inactive	Active
iii3	Calcium imaging	Tonic	Activity decreased	Activity increased
iii4	Calcium imaging	-	Minor/inactive	Minor/inactive
hg1	Electrophysiology, calcium imaging	Phasic	Active	Inactive
hg2	Calcium imaging	-	Minor/inactive	Minor/inactive
hg3	Electrophysiology, calcium imaging	Phasic	Active	Inactive
hg4	Calcium imaging	Tonic	Activity increased	Activity decreased

Methods

EASI-FISH protocol

Expansion-Assisted Iterative FISH (EASI-FISH) (Wang et al., 2021) was used for probing neurotransmitter-related genes with improved spatial resolution and more sensitive detection of transcripts compared to standard FISH techniques. Briefly, flies of DN split-Gal4 lines were crossed to UAS-CsChrimson-mVenus. Brains of F1 offspring were prepared for EASI-FISH with GFP antibody detection of Gal4-labeled DNs as described in (Eddison, 2022). For each single brain (1-3 total brains per split-Gal4 line), EASI-FISH was carried out for pairs of neurotransmitter-related genes (*ChAT, Gad1, VGlut, Tbh, Tdc2, SerT*, marking the neurotransmitters ACh, GABA, Glu, OA, OA/TA, and 5-HT respectively). The combinations of gene pairs probed per line were selected based on predicted neurotransmitter identity in MANC: for DNs with high prediction scores (>=0.7) for one of the three primary neurotransmitters (ACh, GABA, Glut), the probe combination covered the likely positive neurotransmitter and another primary neurotransmitter as a negative control. DNs of interest or with low primary neurotransmitter predictions were probed for genes for more minor neurotransmitters. A set of brains for DNp20, DNp24, DNd02, DNg34 and DNp27 that were probed for Tbh and Gad1 were stripped using the protocol described in (Eddison, 2022) and reprobed for ChAT and VGlut. A single brain per split line was probed for each pair of neurotransmitter gene combinations, and neurotransmitter identity was called based on all DN cells of the given type labeled in the brain (a pair or more), unless noted in Supplementary File 2.

Standard FISH protocol

A standardized neurotransmitter FISH was carried out as previously described (Meissner et al., 2019) with neurotransmitter probes of one of two possible sets: *ChAT, Gad1*, and *VGlut* for ACh, GABA and Glu respectively, and *Tbh, SerT* and *pale* for OA, 5-HT and DA respectively. For each DN split-Gal4 line, 2-3 CNSes were probed for a given combination of neurotransmitter probes. Imaging was carried out on a Zeiss LSM 880 confocal microscope with a 63x/1.40 Oil Plan Apochromat DIC M27 objective with laser excitation at 488, 561, 594 and 633 nm.

CNS immunohistochemistry

Flies were anesthetized on ice and dissected in ice-cold PBS. Isolated CNSes were fixed in 4% formaldehyde in PBS with 0.5% Triton X-100 (PBST) at room temperature for 30 minutes. After washing with PBST, CNSes were incubated with anti-GFP sheep polyclonal antibody (3:5000, AbD Serotec, #4745-1051) and nc82 mouse monoclonal antibody (1:50, DSHB) in 5% normal donkey serum in PBST for 2 days at 4°C, then following another set of washes in PBST, Dylight 488-conjugated anti-sheep donkey antibody (3:5000, Jackson ImmunoResearch, #713-485-147) and Dylight 649-conjugated anti-mouse donkey antibody (1:250, Jackson ImmunoResearch, #715-495-150) for 2 days. Following washing, CNSes were mounted on poly-L-lysine-coated coverslips in Vectashield antifade reagent (Vector Laboratories, H-1000-10) and imaged on a Zeiss 980 confocal microscope with a 20x/1.0 W Plan-Apochromat DIC M27 75mm objective with laser excitation at 488 and 639 nm.

Thoracic muscle staining and immunohistochemistry

Flies were anesthetized on ice and briefly washed with 70% ethanol. Thoraces were isolated under 2% paraformaldehyde/PBS/0.1% Triton X-100 and fixed in this solution overnight at 4°C. After washing in PBS containing 1% Triton X-100, the samples were embedded in 7% agarose and sectioned on a Leica Vibratome (VT1000s) sagitally at 0.2 mm. The slices were incubated in PBS with 1% Triton X-100, containing Texas Red-X Phalloidin (1:50, Life Technologies #T7471) and anti-GFP rabbit polyclonal antibodies (1:1000, Thermo Fisher, #A10262) and a chitin-binding dye Calcofluor White (0.1 mg/ml, Sigma-Aldrich #F3543-1G) at room temperature with agitation for 2 days. After a series of four ~1h-long washes in PBS containing surfactants, the sections were incubated for another 24h in the above buffer containing secondary antibodies (1:1000, goat anti-rabbit, Thermo Fisher #A32731). The samples were then washed in PBS/1% Triton X-100 and fixed for 4 hours in 2% paraformaldehyde to reduce leaching of bound phalloidin from muscles during the subsequent ethanol dehydration step. To avoid artifacts caused by osmotic shrinkage of soft tissue, samples were gradually dehydrated in glycerol (2-80%) and then ethanol (20-100%) (Ott, 2008) and mounted in methyl salicylate for imaging.

Serial optical sections were obtained at 1 µm intervals on a Zeiss 980 confocal microscope with a LD-LCI 25x/0.8 NA objective, or at 0.5 µm with a Plan-Apochromat 40x/0.8 NA objective. Calcofluor White, Anti-GFP/anti-rabbit Alexa 488 antibodies and Texas Red phalloidin-treated samples were imaged using 405, 488 and 594 nm lasers, respectively. Images were processed in Fiji (http://fiji.sc/), Icy (http://icy.bioimageanalysis.org/) and Photoshop (Adobe Systems Inc.).

Identification of descending neurons

We chose a perpendicular plane through the neck connective posterior to the cervical nerve and anterior to the prothoracic neuropil entrance (Power, 1948; z = 67070) and annotated every neuronal profile passing through this plane. We then systematically proofread the automatic segmentation as described in (Scheffer et al., 2020) and (Takemura et al., 2023) with focus on the descending neurons (no soma in VNC). DNs were reconstructed by a human proofreader to capture the full extent of their axonic branches in the VNC. We then mirrored the left hand side neurons passing through the neck connective by transforming them through a symmetrized version of the dataset using the malevnc_symmetric_manc function. We then ran NBLAST clustering (Costa et al., 2016) analysis on the mirrored left hand side and non-mirrored right hand side neurons. This allowed for systematic high quality proofreading and grouping of left-right homologous pairs. Many left/right neuron pairs had unique morphological characteristics and branching patterns were grouped into a pair of a single neuron in each hemisphere. However in some instances larger groups containing multiple neurons with morphology were combined into groups containing more than one neuron per hemisphere.

To match DNs to light-level identifications, we obtained segmentations of DN Gal4 expression patterns (Namiki et al., 2018) and transformed them as described above for tract meshes into MANC space. Overlaying EM reconstructed DNs with the segmentations aided the identification of previously described DNs. We further used neuronbridge (Clements et al., 2022; Meissner et al., 2023) to match EM reconstructed DNs to Janelia's Gal4 and Split-Gal4 collection. For every

match, we indicated the line and slide code used for the matching and employed a confidence system of 1 to 5 from worst to best match (see Supplementary File 1).

Tract identification

We obtained the VNC longitudinal tract meshes generated by (Court et al., 2020) from https://www.virtualflybrain.org/ (Court et al., 2023) (ids: VFB_00104642, VFB_00104635, VFB_00104636, VFB_00104637, VFB_00104634, VFB_00104638, VFB_00104633) and transformed them from their original JRC2018VNC_U space into MANC space. We then simplified all DN axon skeletons to their longest neurite starting from their VNC entrance in the neck connective and NBLAST clustered them. Through manual review of the resulting clusters and checking for overlap with the longitudinal tracts from (Court et al., 2020) we assigned tract membership to all DNs. In accordance with the definitions in (Namiki et al., 2018) short DNs that terminated in T1 or did not join a tract for notable distance were not assigned a tract membership. We choose the tract nomenclature from (Namiki et al., 2018) and include a table below of tracts identified in this paper compared to prior identifications and their nomenclature (Table 2). Overlaying the longest neurite skeletons onto the EM images further helped the assignment of the tracts (Figure 2A, B). We found that DMT from (Court et al., 2020) is not overlapping with type-I MTD from (Namiki et al., 2018) and thus kept them separate with their original published name. Additionally, we identified two smaller tracts that were previously undescribed (type-III MTD and CVL). While type-I takes a ventral and type-II MTD a dorsal route, type-III originates in type-II, leaving the tract between T1 and T2 to run more ventral and lateral. The CVL tract starts in the neck connective ventro-medially and then curves around the T1 leg neuromeres ventrally towards the lateral posterior end of T1, it then continues medially followed by dorsally in T2, repeating the same pattern in T3 and the abdomen neuromeres.

We then created new tract meshes for MANC based on the neurons identified for each tract. First we choose three primary neurites of DNs in a given tract that represented the tract structure the best. We then subsetted all primary neurites to those three for each tract, keeping all points with a maximum distance of 10µm. We calculated the 3D α-shape from the xyz coordinates of the remaining points (R, alphashape3d package) and smoothed the meshes using Blender version 2.82. The tract meshes are available in the malevnc R package (https://natverse.github.io/malevnc).

Table 2: VNC tracts according to (Court et al., 2020) and (Namiki et al., 2018)

This study	**VFB_id**	**Court et al. 2020**	**Namiki et al. 2018**
MDA	VFB_00104636	MDT	MDA
DLT	VFB_00104633	DLT	DLT
DMT	VFB_00104635	DMT	
type-I MTD			type-I MTD

This study	VFB_id	Court et al. 2020	Namiki et al. 2018
type-II MTD			type-II MTD
type-III MTD			
ITD	VFB_00104638	ITD	ITD
VLT	VFB_00104637	VLT	VLT
DLV	VFB_00104634	DLV	DLV
VTV	VFB_00104642	VTV	VTV
CVL			

Identification of motor neurons

Motor neurons and other neurons that enter or exit through VNC nerves were identified by direct annotation of bodies passing through nerves, or for certain MNs with degradation issues, by morphological identification or matching to MNs on opposite side of VNC, or by assessment of input/output ratio (assuming MNs have high input and low output synapse count). The initial segmentation for some MNs were considered poorer due to MN degradation issues. Thus, a limited resegmentation of MNs was carried out by retraining the flood-filling network model used for EM segmentation (Januszewski et al., 2018; Takemura et al., 2023) with additional ground truth from six MN reconstructions with human-curated merges. When leg MNs could not be fully traced out through the leg nerves due to axonal damage or degradation, exit nerve was putatively annotated based on MNs in the same morphological group. For all MNs, a team of trained proofreaders carried out proofreading and reconstruction, as well as group assignments by manual assessment of morphology and NBLAST matching across the midline. Groups were then refined by serial homology matching by connectivity and morphology for leg MNs.

During cell class assignment, we distinguished between MNs and a more generic ‘efferent’ class based on several criteria: cells are considered MNs if cell morphology and muscle target is known in the literature; otherwise, cells were putatively classified as MNs if they send a single axon out of the VNC via a single nerve, and were considered efferents if they send multiple projections out of the VNC or have known or suspected neuromodulatory roles. The latter includes the ventral unpaired medians, which leaves the VNC via multiple nerves to innervate muscles on bilateral sides of the body and play a neuromodulatory role (Coggshall, 1978; Ehrhardt et al., 2023; Schlurmann and Hausen, 2003), and we note their identity wherever possible (Supplementary File 2).

To identify MNs across the VNC, we primarily matched MNs to light-level data from (Ehrhardt et al., 2023) for wing MNs, (Dickerson et al., 2019; Ehrhardt et al., 2023) for haltere MNs, and (Enriquez et al., 2018) for leg MNs. Secondarily, we cross-checked MN matches by a plethora of light-level imagery and descriptions available in the literature (Bacon and Strausfeld, 1986; Dickerson et al., 2019; Ehrhardt et al., 2023; King and Wyman, 1980; Namiki et al., 2018;

O'Sullivan et al., 2018; Schlurmann and Hausen, 2007; Sun and Wyman, 1997; Trimarchi and Schneiderman, 1994). For wing MNs, we further identified the hg4, b3 and ps2 MNs from new or published split-Gal4 lines (Figure 6–supplement 1) (Sterne et al., 2021; Wu et al., 2016). Confidence for all matches were rated on a scale of 1-5, where matches scored 3 and below are putative. In addition, for the T1 leg MNs, we referred to a recent description of all T1 leg MNs at both the light and EM levels (Azevedo et al., 2022). Wing MN identifications were corroborated with a parallel identification effort in FANC (Azevedo et al., 2022). Supplementary File 2 shows the bodyids, type, systematic type, light-level matches and match confidence (if known in literature) for all MNs and efferents found within the MANC volume.

Serial homology matching

To identify T2 and T3 leg MNs that are serially homologous to T1 leg MNs, we initially transformed the T1 leg MNs from the Female Adult Nerve Cord (FANC) EM volume (Azevedo et al., 2022) to MANC space and performed an NBLAST comparison between MNs from the two VNC datasets (Costa et al., 2016). With expert visual evaluation, this allowed us to match up all FANC-identified T1 leg MNs to the MANC dataset. As efforts were made to match serially-repeating homologs of other neuron classes across segments in MANC (Marin et al., 2023), we reasoned that this data could be leveraged to identify serial homologs of the T1 leg MNs in the T2 and T3 segments, by comparison of MN connectivity received from identified serially homologous neurons across the 3 thoracic segments, as well as connectivity from neurons that reach across several thoracic segments (mainly DNs, ascending neurons and intrinsic neurons). This method allowed us to transfer the MN identification from 198 MN the front legs to the middle and hind leg MNs. The dendritic morphology of the MNs identified by connectivity is highly stereotyped across the three leg neuromeres and their dendritic fields occupy similar yet slightly rotated areas in T1, T2 and T3. MNs that target the same type of muscle but in different leg compartments, such as the long tendon muscle (ltm) in the femur and the tibia, differ slightly also in their dendritic morphology in the VNC. Here one difference observed is two dendritic branches extending towards the midline for MNs innervating the femur and a single medial branch for MNs innervating the tibia ltm (Figure 7B on the left). However, there are also differences between leg MNs that innervate the same leg muscle target, for example the previously described slow and fast tibia extensor MNs, FETi and SETi (Figure 7B on the right) (Azevedo et al., 2022), which we observed consistently across all leg compartments. Muscles innervated by multiple MNs in T1 were assigned several serial sets, which we pooled together for the standard leg connectome analysis in the later sections of this manuscript.

The non-serially identified MNs in T2 and T3 were either not well constructed enough to make a match to T1 MNs or differed so strongly in their connectivity or morphology that they did not resemble any the T1 MNs. There were, however, some serial sets that could not be assigned a muscle target although there was a serial set present. For two of these serial sets (13214 and 11274) we assume that the function and muscle targets between the segments is distinct, as the T2 pair of these sets are the identified STTMm neurons (Figure 7–Supplement 1B, top). The other examples are a T1 MN pair that we could not identify in FANC, in the serial set 17664 with

a T2 MN pair and a serial set that only contains a T2 and T3 pair but we could not find a T1 resemblance (Figure 7–Supplement 1B bottom).

DN and MN systematic type naming and subclass

The systematic type is a combination of the prefix 'DN' or 'MN', the two-letter subclass (defined by the target) and a number that is consistent within the group and serial set. Smaller numbers were assigned to identified DNs or MNs, respectively.

DNs were assigned a two-letter subclass name in accordance with their VNC neuropil target. The subclasses nt,wt,ht,it,lt,fl,ml,hl and ad were given for the single neuropil innervating DNs corresponding to the targets NTct, WTct, HTct, IntTct, LTct, LegNpT1, LegNpT2, LegNpT3 and ANm. Subsequently DNs were assigned the subclass xl or ut if they targeted a combination of leg (target: LNP) or upper tectulum neuropils (target: UT). In situations where there were inconsistencies for neuropil innervation within pairs or groups of DNs, we calculated the mean percent to determine the assignment. All DNs that had more than a single neuropil and not a combination of upper tectulum or leg neuropils were given the subclass xn, for multiple neuropils. In total, 491 systematicTypes were given to DNs.

MNs were assigned a two-letter subclass name in accordance with their target muscle or target muscle group. For all unidentified MNs, the target muscle group was predicted by the exit nerve. The two-letter subclasses stand for front (fl), middle (ml) and hind leg muscles (hl), neck (nm), wing (wm) and haltere muscles (hm) and abdominal muscles (ad). There were only 6 MNs that we were unsure about the muscle they target in the periphery; they were assigned the xm subclass, for unknown muscle target. In total, 276 systematicTypes were given to MNs.

Connectome Analyses

The neuprint web application (https://neuprint.janelia.org) provides a graphical front end to explore many aspects of the vnc dataset (Plaza et al., 2022). However a wide range of more sophisticated analyses were enabled by developing small scripts using the natverse suite of tools (Bates et al., 2020) built on top of the R statistical programming language (https://www.r-project.org). Connectome data was queried via the neuprint API using the neuprintr package (https://natverse.org/neuprintr) (Schlegel et al., 2021). For convenience the most common functionality was wrapped in a specialized malevnc package (https://natverse.github.io/malevnc/) which is the recommended point of entry for detailed analysis.

Indirect connectivity strength

The connectome can reveal both the direct connections between any pair of neurons (or between any two groups of neurons) and the indirect pathways via one or more intermediate neurons. In many cases indirect pathways appear stronger than direct ones; it is therefore helpful to define a measure of connectivity that can quantify indirect connections. We adopted the general approach of (Li et al., 2020). Briefly, we retrieved the all-to-all connectivity matrix for

all valid VNC neurons (assigned a neuronal class in the neuprint ‘class’ field), and normalized all synapse weights to input fractions (sum of inputs for each neuron equals 1). Then, we carried out matrix multiplication of the normalized connectivity matrix with itself for a number of times equal to the path length of interest. For analyses of DN to wing MN connectivity, indirect connectivity strength was calculated at the neuron group level (i.e. synapse counts were summed by group before normalization), with or without separation of neuron side (soma, root or nerve side). Optionally, input fractions to DNs and SNs are set to zero to avoid considering paths through them.

To compare indirect connectivity strength values calculated across different path lengths, we first normalized the values for a given source neuron and path length with their non-zero mean at the given path length. Then, for each target neuron, we compared its normalized values across all path lengths (in practice up to 5); the top value, and the path length it was found at, was taken as the neuron’s normalized indirect connectivity strength value and path length. To determine groupwise normalized indirect connectivity strength value and path length, we then calculate the mean of both these values for all neurons belonging to the same group.

Indirect connectivity strength was also used as an exploratory tool to retrieve neurons or neuron groups contributing to the connectivity between two neurons or neuron groups of interest (e.g. as an intermediary between DN and MN). Here, indirect connectivity strength was calculated from the upstream neuron to each potential intermediary neuron, and separately from the intermediary neuron to the downstream neuron, where the individual path lengths sum to the total path length of interest. The product of the upstream and downstream indirect connectivity strength was then calculated, and top-scoring neurons were considered the best candidates for intermediary neurons. To consider paths through population neuron types where individual connectivity is weak but collectively provide large synapse counts, neurons were optionally collapsed by group (sum groupwise synapse counts before conversion to input fractions) before taking matrix products. Connectivity between DNs, these intermediary neuron or group candidates and MNs were then plotted in Cytoscape via the RCytoscape R package for further circuit exploration and graph plotting.

Connectome pathway exploration

We first calculated percent of the total input to the postsynaptic neuron and percent of the output budget of the presynaptic neuron for every edge in the VNC connectome. To favor connections that are strong edges for both the pre- and postsynaptic neuron in our connectome analysis we calculated the geometric mean of these two matrices. We then calculated the matrix-vector-product using the geometric mean matrix and a vector that is 1 for a pair or group of neurons of interest and is 0 for all other VNC neurons. Selecting the 20 postsynaptic neurons with the strongest edges reveals the first layer downstream of the neurons of interest. The resulting vector is then multiplied by the geometric mean matrix again to explore the second layer downstream. This step was repeated three more times to describe up to five downstream layers. After selecting the neurons involved in the circuit we used the RCy3 (version 2.17.1) and igraph (version 1.3.0) packages in R to create graphs in Cytoscape (version 3.9.1) for further exploration and visualization.

The same method was used to calculate effective connectivity strength between DNs of interest and leg MNs. For comparisons across the layers, we normalized by the non-zero mean of all scores in each layer. For each given DN-MN-pair we picked the highest score of the five layer matrices and recorded the layer in which it occurred. We termed this analysis effective connectivity strength.

Quantification of contact area between neurons for evaluating putative presence of electrical synapses

To quantify area of contact between putative electrical neurons and wing MNs, we retrieved 3D meshes of all neurons of interest that were generated and simplified from EM segmentation using the malevnc R package from the MANC clio data store (https://github.com/clio-janelia/clio_website) (Perlman, 2019). Using a custom python script in Blender version 3.4 (https://www.blender.org), all neuron meshes were expanded by 100 nm using the blender shrink/fatten function to create mesh intersection areas between closely-situated areas (up to 200 nm apart, but with inaccuracies as neuron meshes are simplified from the underlying segmentation) for pairs of neurons. Then, for each pair of neurons, we calculated pairwise mesh intersections using a hole-tolerant exact method and calculated the area of the intersection mesh, divided by half to get the mean of the two surfaces contributed by each neuron mesh.

References

Ache JM, Namiki S, Lee A, Branson K, Card GM. 2019. State-dependent decoupling of sensory and motor circuits underlies behavioral flexibility in Drosophila. *Nat Neurosci* **22**:1132–1139.

Agrawal S, Dickinson ES, Sustar A, Gurung P, Shepherd D, Truman JW, Tuthill JC. 2020. Central processing of leg proprioception in Drosophila. *Elife* **9**. doi:10.7554/eLife.60299

Ammer G, Vieira RM, Fendl S, Borst A. 2022. Anatomical distribution and functional roles of electrical synapses in Drosophila. *Curr Biol* **32**:2022–2036.e4.

Ando K, Hearn S, Suzuki E, Maruko-Otake A, Sekiya M, Iijima KM. 2016. Electron Microscopy of the Brains of Drosophila Models of Alzheimer's Diseases In: Van Bockstaele EJ, editor. Transmission Electron Microscopy Methods for Understanding the Brain. New York, NY: Springer New York. pp. 105–123.

Aymanns F, Chen C-L, Ramdya P. 2022. Descending neuron population dynamics during odor-evoked and spontaneous limb-dependent behaviors. *Elife* **11**. doi:10.7554/eLife.81527

Azevedo A, Lesser E, Mark B, Phelps J, Elabbady L, Kuroda S, Sustar A, Moussa A, Kandelwal A, Dallmann CJ, Agrawal S, Lee S-YJ, Pratt B, Cook A, Skutt-Kakaria K, Gerhard S, Lu R, Kemnitz N, Lee K, Halageri A, Castro M, Ih D, Gager J, Tammam M, Dorkenwald S, Collman F, Schneider-Mizell C, Brittain D, Jordan CS, Dickinson M, Pacureanu A, Sebastian Seung H, Macrina T, Lee W-CA, Tuthill JC. 2022. Tools for comprehensive reconstruction and analysis of Drosophila motor circuits. *bioRxiv*. doi:10.1101/2022.12.15.520299

Azevedo AW, Dickinson ES, Gurung P, Venkatasubramanian L, Mann RS, Tuthill JC. 2020. A size principle for recruitment of Drosophila leg motor neurons. *Elife* **9**. doi:10.7554/eLife.56754

Bacon JP, Strausfeld NJ. 1986. The dipteran "Giant fibre" pathway: neurons and signals. *Journal of Comparative Physiology A* **158**:529–548.

Baek M, Mann RS. 2009. Lineage and birth date specify motor neuron targeting and dendritic architecture in adult Drosophila. *J Neurosci* **29**:6904–6916.

Bates AS, Manton JD, Jagannathan SR, Costa M, Schlegel P, Rohlfing T, Jefferis GS. 2020. The natverse, a versatile toolbox for combining and analysing neuroanatomical data. doi:10.7554/eLife.53350

Bidaye SS, Bockemühl T, Büschges A. 2018. Six-legged walking in insects: how CPGs, peripheral feedback, and descending signals generate coordinated and adaptive motor rhythms. *J Neurophysiol* **119**:459–475.

Bidaye SS, Machacek C, Wu Y, Dickson BJ. 2014. Neuronal control of Drosophila walking direction. *Science* **344**:97–101.

Boerner J, Duch C. 2010. Average shape standard atlas for the adult Drosophila ventral nerve cord. *J Comp Neurol* **518**:2437–2455.

Brierley DJ, Rathore K, VijayRaghavan K, Williams DW. 2012. Developmental origins and architecture of Drosophila leg motoneurons. *J Comp Neurol* **520**:1629–1649.

Büschges A, Scholz H, El Manira A. 2011. New moves in motor control. *Curr Biol* **21**:R513–24.

Busch S, Selcho M, Ito K. 2009. A map of octopaminergic neurons in the Drosophila brain. *Journal of Comparative*.

Cande J, Namiki S, Qiu J, Korff W, Card GM, Shaevitz JW, Stern DL, Berman GJ. 2018.

Optogenetic dissection of descending behavioral control in Drosophila. *Elife* **7**. doi:10.7554/eLife.34275

Card G, Dickinson M. 2008. Performance trade-offs in the flight initiation of Drosophila. *J Exp Biol* **211**:341–353.

Castellanos MC, Tang JCY, Allan DW. 2013. Female-biased dimorphism underlies a female-specific role for post-embryonic Ilp7 neurons in Drosophila fertility. *Development* **140**:3915–3926.

Chen C-L, Hermans L, Viswanathan MC, Fortun D, Aymanns F, Unser M, Cammarato A, Dickinson MH, Ramdya P. 2018. Imaging neural activity in the ventral nerve cord of behaving adult Drosophila. *Nat Commun* **9**:4390.

Clements J, Goina C, Hubbard PM, Kawase T, Olbris DJ, Otsuna H, Svirskas R, Rokicki K. 2022. NeuronBridge: an intuitive web application for neuronal morphology search across large data sets. *bioRxiv*. doi:10.1101/2022.07.20.500311

Clyne JD, Miesenböck G. 2008. Sex-specific control and tuning of the pattern generator for courtship song in Drosophila. *Cell* **133**:354–363.

Coggshall JC. 1978. Neurons associated with the dorsal longtitudinal flight muscles of Drosophilla melanogaster. *J Comp Neurol* **177**:707–720.

Costa M, Manton JD, Ostrovsky AD, Prohaska S, Jefferis GSXE. 2016. NBLAST: Rapid, Sensitive Comparison of Neuronal Structure and Construction of Neuron Family Databases. *Neuron* **91**:293–311.

Court R, Costa M, Pilgrim C, Millburn G, Holmes A, McLachlan A, Larkin A, Matentzoglu N, Kir H, Parkinson H, Brown NH, O'Kane CJ, Armstrong JD, Jefferis GSXE, Osumi-Sutherland D. 2023. Virtual Fly Brain-An interactive atlas of the nervous system. *Front Physiol* **14**:1076533.

Court R, Namiki S, Armstrong JD, Börner J, Card G, Costa M, Dickinson M, Duch C, Korff W, Mann R, Merritt D, Murphey RK, Seeds AM, Shirangi T, Simpson JH, Truman JW, Tuthill JC, Williams DW, Shepherd D. 2020. A Systematic Nomenclature for the Drosophila Ventral Nerve Cord. *Neuron* **107**:1071–1079.e2.

DeAngelis BD, Zavatone-Veth JA, Clark DA. 2020. Correction: The manifold structure of limb coordination in walking. *Elife* **9**. doi:10.7554/eLife.65214

DeAngelis BD, Zavatone-Veth JA, Clark DA. 2019. The manifold structure of limb coordination in walking Drosophila. *Elife* **8**. doi:10.7554/eLife.46409

Deora T, Gundiah N, Sane SP. 2017. Mechanics of the thorax in flies. *J Exp Biol* **220**:1382–1395.

Deora T, Sane SS, Sane SP. 2021. Wings and halteres act as coupled dual oscillators in flies. *Elife* **10**. doi:10.7554/eLife.53824

Deora T, Singh AK, Sane SP. 2015. Biomechanical basis of wing and haltere coordination in flies. *Proc Natl Acad Sci U S A* **112**:1481–1486.

Dickerson BH. 2020. Timing precision in fly flight control: integrating mechanosensory input with muscle physiology. *Proc Biol Sci* **287**:20201774.

Dickerson BH, de Souza AM, Huda A, Dickinson MH. 2019. Flies Regulate Wing Motion via Active Control of a Dual-Function Gyroscope. *Curr Biol* **29**:3517–3524.e3.

Dickinson MH, Muijres FT. 2016. The aerodynamics and control of free flight manoeuvres in Drosophila. *Philos Trans R Soc Lond B Biol Sci* **371**. doi:10.1098/rstb.2015.0388

Dickinson MH, Tu MS. 1997. The Function of Dipteran Flight Muscle. *Comp Biochem Physiol A Physiol* **116**:223–238.

Dombrovski M, Peek MY, Park J-Y, Vaccari A, Sumathipala M, Morrow C, Breads P, Zhao A, Kurmangaliyev YZ, Sanfilippo P, Rehan A, Polsky J, Alghailani S, Tenshaw E, Namiki S, Zipursky SL, Card GM. 2023. Synaptic gradients transform object location to action. *Nature* **613**:534–542.

Dorkenwald S, McKellar CE, Macrina T, Kemnitz N, Lee K, Lu R, Wu J, Popovych S, Mitchell E, Nehoran B, Jia Z, Bae JA, Mu S, Ih D, Castro M, Ogedengbe O, Halageri A, Kuehner K, Sterling AR, Ashwood Z, Zung J, Brittain D, Collman F, Schneider-Mizell C, Jordan C, Silversmith W, Baker C, Deutsch D, Encarnacion-Rivera L, Kumar S, Burke A, Bland D, Gager J, Hebditch J, Koolman S, Moore M, Morejohn S, Silverman B, Willie K, Willie R, Yu SC, Murthy M, Seung HS. 2022. FlyWire: online community for whole-brain connectomics. *Nat Methods* **19**. doi:10.1038/s41592-021-01330-0

Eckstein N, Bates AS, Du M, Hartenstein V, Jefferis GSX, Funke J. 2020. Neurotransmitter Classification from Electron Microscopy Images at Synaptic Sites in Drosophila. *bioRxiv*. doi:10.1101/2020.06.12.148775

Eddison M. 2022. Expansion-assisted iterative fluorescence in situ hybridization (EASI-FISH) in Drosophila CNS v1. doi:10.17504/protocols.io.5jyl8jmw7g2w/v1

Egelhaaf M. 1989. Visual afferences to flight steering muscles controlling optomotor responses of the fly. *J Comp Physiol A* **165**:719–730.

Ehrhardt E, Whitehead SC, Namiki S, Minegishi R, Siwanowicz I, Feng K, Otsuna H, FlyLight Project Team, Meissner GW, Stern D, Truman J, Shepherd D, Dickinson M, Ito K, Dickson BJ, Cohen I, Korff W, Card GM. 2023. Single cell type analysis of wing premotor circuits in the ventral nerve cord of Drosophila melanogaster. *bioRxiv*. doi:10.1101/2023.05.31.542897

Enriquez J, Rio LQ, Blazeski R, Bellemin S, Godement P, Mason C, Mann RS. 2018. Differing Strategies Despite Shared Lineages of Motor Neurons and Glia to Achieve Robust Development of an Adult Neuropil in Drosophila. *Neuron* **97**:538–554.e5.

Ewing AW. 1977. The neuromuscular basis of courtship song inDrosophila: The role of the indirect flight muscles. *J Comp Physiol* **119**:249–265.

Fayyazuddin A, Dickinson MH. 1999. Convergent mechanosensory input structures the firing phase of a steering motor neuron in the blowfly, Calliphora. *J Neurophysiol* **82**:1916–1926.

Fayyazuddin A, Dickinson MH. 1996. Haltere afferents provide direct, electrotonic input to a steering motor neuron in the blowfly, Calliphora. *J Neurosci* **16**:5225–5232.

Feng K, Sen R, Minegishi R, Dübbert M, Bockemühl T, Büschges A, Dickson BJ. 2020. Distributed control of motor circuits for backward walking in Drosophila. *Nat Commun* **11**:6166.

Fenk LM, Avritzer SC, Weisman JL, Nair A, Randt LD, Mohren TL, Siwanowicz I, Maimon G. 2022. Muscles that move the retina augment compound eye vision in Drosophila. *Nature* **612**:116–122.

Gao XJ, Potter CJ, Gohl DM, Silies M, Katsov AY, Clandinin TR, Luo L. 2013. Specific kinematics and motor-related neurons for aversive chemotaxis in Drosophila. *Curr Biol* **23**:1163–1172.

Gordon S, Dickinson MH. 2006. Role of calcium in the regulation of mechanical power in insect flight. *Proc Natl Acad Sci U S A* **103**:4311–4315.

Götz KG. 1983. Bewegungssehen und flugsteuerung bei der fliege DrosophilaSymposium Physiology and Biophysics of Insect Flight 1982. Fischer. pp. 21–34.

Greenspan RJ, Ferveur JF. 2000. Courtship in Drosophila. *Annu Rev Genet* **34**:205–232.

Grillner S, Kozlov A. 2021. The CPGs for Limbed Locomotion-Facts and Fiction. *Int J Mol Sci* **22**. doi:10.3390/ijms22115882

Guo L, Zhang N, Simpson JH. 2022. Descending neurons coordinate anterior grooming behavior in Drosophila. *Curr Biol* **32**:823–833.e4.

Harcombe ES, Wyman RJ. 1978. The cyclically repetitive firing sequencess of identified Drosophila flight motoneurons. *J Comp Physiol* **123**:271–279.

Harcombe ES, Wyman RJ. 1977. Output pattern generation by Drosophila flight motoneurons. *J Neurophysiol* **40**:1066–1077.

Harris RM, Pfeiffer BD, Rubin GM, Truman JW. 2015. Neuron hemilineages provide the functional ground plan for the Drosophila ventral nervous system. doi:10.7554/eLife.04493

Heide G. 1983. Neural mechanisms of flight control in Diptera. *BIONA-report* 35–52.

Heide G. 1975. Properties of a motor output system involved in the optomotor response in flies. *Biol Cybern* **20**:99–112.

Heide G, Götz KG. 1996. Optomotor control of course and altitude in Drosophila melanogaster is correlated with distinct activities of at least three pairs of flight steering muscles. *J Exp Biol* **199**:1711–1726.

Hiraoka K. 2021. Phase-Dependent Crossed Inhibition Mediating Coordination of Anti-phase Bilateral Rhythmic Movement: A Mini Review. *Front Hum Neurosci* **15**:668442.

Hsu CT, Bhandawat V. 2016. Organization of descending neurons in Drosophila melanogaster. *Sci Rep* **6**. doi:10.1038/srep20259

Hulse BK, Haberkern H, Franconville R, Turner-Evans D, Takemura S-Y, Wolff T, Noorman M, Dreher M, Dan C, Parekh R, Hermundstad AM, Rubin GM, Jayaraman V. 2021. A connectome of the Drosophila central complex reveals network motifs suitable for flexible navigation and context-dependent action selection. *Elife* **10**. doi:10.7554/eLife.66039

Hürkey S, Niemeyer N, Schleimer J-H, Ryglewski S, Schreiber S, Duch C. 2022. Insect asynchronous flight requires neural circuit de-synchronization by electrical synapses. *bioRxiv*. doi:10.1101/2022.02.02.478622

Januszewski M, Kornfeld J, Li PH, Pope A, Blakely T, Lindsey L, Maitin-Shepard J, Tyka M, Denk W, Jain V. 2018. High-precision automated reconstruction of neurons with flood-filling networks. *Nat Methods* **15**:605–610.

Kennedy T, Broadie K. 2018. Newly Identified Electrically Coupled Neurons Support Development of the Giant Fiber Model Circuit. *eNeuro* **5**. doi:10.1523/ENEURO.0346-18.2018

King DG, Wyman RJ. 1980. Anatomy of the giant fibre pathway in Drosophila. I. Three thoracic components of the pathway. *J Neurocytol* **9**:753–770.

Koto M, Tanouye MA, Ferrus A, Thomas JB, Wyman RJ. 1981. The morphology of the cervical giant fiber neuron of Drosophila. *Brain Res* **221**:213–217.

Kravitz EA, Fernandez M de la P. 2015. Aggression in Drosophila. *Behav Neurosci* **129**:549–563.

Lacin H, Chen H-M, Long X, Singer RH, Lee T, Truman JW. 2019. Neurotransmitter identity is acquired in a lineage-restricted manner in the Drosophila CNS. *Elife* **8**.

doi:10.7554/eLife.43701
Lehmann FO, Götz KG. 1996. Activation phase ensures kinematic efficacy in flight-steering muscles of Drosophila melanogaster. *J Comp Physiol A* **179**:311–322.
Lehmann F-O, Skandalis DA, Berthé R. 2013. Calcium signalling indicates bilateral power balancing in the Drosophila flight muscle during manoeuvring flight. *J R Soc Interface* **10**:20121050.
Lesser E, Azevedo AW, Phelps JS, Elabbady L, Cook AP, Mark B, Kuroda S, Sustar A, Moussa AJ, Dallmann CJ, Agrawal S, Lee S-YJ, Pratt BG, Skutt-Kakari K, Gerhard S, Lu R, Kemnitz N, Lee K, Halageri A, Castro M, Ih D, Gager J, Tammam M, Dorkenwald S, Collman FC, Schneider-Mizell CM, Brittain D, Jordan CS, Sebastian Seung H, Macrina T, Dickinson MH, Lee W-CA, Tuthill JC. 2023. Synaptic architecture of leg and wing motor control networks in Drosophila. *bioRxiv*. doi:10.1101/2023.05.30.542725
Li F, Lindsey JW, Marin EC, Otto N, Dreher M, Dempsey G, Stark I, Bates AS, Pleijzier MW, Schlegel P, Nern A, Takemura S-Y, Eckstein N, Yang T, Francis A, Braun A, Parekh R, Costa M, Scheffer LK, Aso Y, Jefferis GS, Abbott LF, Litwin-Kumar A, Waddell S, Rubin GM. 2020. The connectome of the adult Drosophila mushroom body provides insights into function. *Elife* **9**. doi:10.7554/eLife.62576
Lillvis JL, Wang K, Shiozaki HM, Xu M, Stern DL, Dickson BJ. 2023. The neural basis of Drosophila courtship song. *Manuscript in preparation*.
Lindsay T, Sustar A, Dickinson M. 2017. The Function and Organization of the Motor System Controlling Flight Maneuvers in Flies. *Curr Biol* **27**:345–358.
Liu WW, Wilson RI. 2013. Glutamate is an inhibitory neurotransmitter in the Drosophila olfactory system. *Proc Natl Acad Sci U S A* **110**:10294–10299.
Marin EC, Morris BJ, Stuerner T, Champion AS, Krzeminski D, Badalamente G, Gkantia M, Dunne CR, Eichler K, Shin-Takemura Y, Tamimi IFM, Fang S, Moon SS, Cheong HSJ, Li F, Schlegel P, Berg S, FlyEM Project Team, Card GM, Costa M, Shepherd D, Jefferis GSXE. 2023. Systematic annotation of a complete adult male Drosophila nerve cord connectome reveals principles of functional organisation. *bioRxiv*.
McKellar CE, Lillvis JL, Bath DE, Fitzgerald JE, Cannon JG, Simpson JH, Dickson BJ. 2019. Threshold-Based Ordering of Sequential Actions during Drosophila Courtship. *Curr Biol* **29**:426–434.e6.
Meissner GW, Nern A, Dorman Z, DePasquale GM, Forster K, Gibney T, Hausenfluck JH, He Y, Iyer NA, Jeter J, Johnson L, Johnston RM, Lee K, Melton B, Yarbrough B, Zugates CT, Clements J, Goina C, Otsuna H, Rokicki K, Svirskas RR, Aso Y, Card GM, Dickson BJ, Ehrhardt E, Goldammer J, Ito M, Kainmueller D, Korff W, Mais L, Minegishi R, Namiki S, Rubin GM, Sterne GR, Wolff T, Malkesman O, FlyLight Project Team. 2023. A searchable image resource of Drosophila GAL4 driver expression patterns with single neuron resolution. *Elife* **12**. doi:10.7554/eLife.80660
Meissner GW, Nern A, Singer RH, Wong AM, Malkesman O, Long X. 2019. Mapping Neurotransmitter Identity in the Whole-Mount Drosophila Brain Using Multiplex High-Throughput Fluorescence in Situ Hybridization. *Genetics* **211**:473–482.
Mendes CS, Bartos I, Akay T, Márka S, Mann RS. 2013. Quantification of gait parameters in freely walking wild type and sensory deprived Drosophila melanogaster. *Elife* **2**:e00231.
Merritt DJ, Murphey RK. 1992. Projections of leg proprioceptors within the CNS of the fly

Phormia in relation to the generalized insect ganglion. *J Comp Neurol* **322**:16–34.
Miller A. 1950. The internal anatomy and histology of the imago of Drosophila melanogaster. *The Biology of Drosophila* 421–534.
Miyan JA, Ewing AW. 1988. Further observations on dipteran flight: Details of the mechanism. *J Exp Biol* **136**:229–241.
Miyan JA, Ewing AW, Lighthill MJ. 1985. How Diptera move their wings: a re-examination of the wing base articulation and muscle systems concerned with flight. *Philos Trans R Soc Lond B Biol Sci* **311**:271–302.
Nachtigall W, Wilson DM. 1967. Neuro-muscular control of dipteran flight. *J Exp Biol* **47**:77–97.
Nalbach G. 1989. The gear change mechanism of the blowfly (Calliphora erythrocephala) in tethered flight. *Journal of Comparative Physiology A* **165**:321–331.
Namiki S, Dickinson MH, Wong AM, Korff W, Card GM. 2018. The functional organization of descending sensory-motor pathways in Drosophila. doi:10.7554/eLife.34272
Namiki S, Kanzaki R. 2016. Comparative Neuroanatomy of the Lateral Accessory Lobe in the Insect Brain. *Front Physiol* **7**:244.
Namiki S, Ros IG, Morrow C, Rowell WJ, Card GM, Korff W, Dickinson MH. 2022. A population of descending neurons that regulates the flight motor of Drosophila. *Curr Biol* **32**:1189–1196.e6.
Ohyama T, Schneider-Mizell CM, Fetter RD, Aleman JV, Franconville R, Rivera-Alba M, Mensh BD, Branson KM, Simpson JH, Truman JW, Cardona A, Zlatic M. 2015. A multilevel multimodal circuit enhances action selection in Drosophila. *Nature* **520**:633–639.
O'Sullivan A, Lindsay T, Prudnikova A, Erdi B, Dickinson M, von Philipsborn AC. 2018. Multifunctional Wing Motor Control of Song and Flight. *Curr Biol* **28**:2705–2717.e4.
Otsuna H, Ito M, Kawase T. 2018. Color depth MIP mask search: a new tool to expedite Split-GAL4 creation. *bioRxiv*. doi:10.1101/318006
Ott SR. 2008. Confocal microscopy in large insect brains: zinc-formaldehyde fixation improves synapsin immunostaining and preservation of morphology in whole-mounts. *J Neurosci Methods* **172**:220–230.
Palmer EH, Omoto JJ, Dickinson MH. 2022. The role of a population of descending neurons in the optomotor response in flying Drosophila. *bioRxiv*. doi:10.1101/2022.12.05.519224
Pavlou HJ, Lin AC, Neville MC, Nojima T, Diao F, Chen BE, White BH, Goodwin SF. 2016. Neural circuitry coordinating male copulation. doi:10.7554/eLife.20713
Peek M. 2018. Control of escape behavior by descending neurons in Drosophila melanogaster. The University of Chicago. doi:10.6082/UCHICAGO.1415
Perlman E. 2019. Visualizing and Interacting with Large Imaging Data. *Microsc Microanal* **25**:1374–1375.
Phelps JS, Hildebrand DGC, Graham BJ, Kuan AT, Thomas LA, Nguyen TM, Buhmann J, Azevedo AW, Sustar A, Agrawal S, Liu M, Shanny BL, Funke J, Tuthill JC, Lee WA. 2021. Reconstruction of motor control circuits in adult Drosophila using automated transmission electron microscopy. *Cell* **184**. doi:10.1016/j.cell.2020.12.013
Plaza SM, Clements J, Dolafi T, Umayam L, Neubarth NN, Scheffer LK, Berg S. 2022. neuPrint: An open access tool for EM connectomics. *Front Neuroinform* **16**. doi:10.3389/fninf.2022.896292
Power ME. 1948. The thoracico-abdominal nervous system of an adult insect, Drosophila

melanogaster. *J Comp Neurol* **88**:347–409.
Pringle JWS, Gray J. 1948. The gyroscopic mechanism of the halteres of Diptera. *Philos Trans R Soc Lond B Biol Sci* **233**:347–384.
Rayshubskiy A, Holtz SL, D'Alessandro I, Li AA, Vanderbeck QX, Haber IS, Gibb PW, Wilson RI. 2020. Neural circuit mechanisms for steering control in walking Drosophila. *bioRxiv*. doi:10.1101/2020.04.04.024703
Rosenbaum P, Schmitz J, Schmidt J, Büschges A. 2015. Task-dependent modification of leg motor neuron synaptic input underlying changes in walking direction and walking speed. *J Neurophysiol* **114**:1090–1101.
Rosvall M, Axelsson D, Bergstrom CT. 2009. The map equation. *Eur Phys J Spec Top* **178**:13–23.
Rosvall M, Bergstrom CT. 2011. Multilevel compression of random walks on networks reveals hierarchical organization in large integrated systems. *PLoS One* **6**:e18209.
Rosvall M, Bergstrom CT. 2008. Maps of random walks on complex networks reveal community structure. *Proc Natl Acad Sci U S A* **105**:1118–1123.
Sadeh S, Clopath C. 2021. Inhibitory stabilization and cortical computation. *Nat Rev Neurosci* **22**:21–37.
Scheffer LK, Shan Xu C, Januszewski M, Lu Z, Takemura S-Y, Hayworth KJ, Huang GB, Shinomiya K, Maitlin-Shepard J, Berg S, Clements J, Hubbard PM, Katz WT, Umayam L, Zhao T, Ackerman D, Blakely T, Bogovic J, Dolafi T, Kainmueller D, Kawase T, Khairy KA, Leavitt L, Li PH, Lindsey L, Neubarth N, Olbris DJ, Otsuna H, Trautman ET, Ito M, Bates AS, Goldammer J, Wolff T, Svirskas R, Schlegel P, Neace E, Knecht CJ, Alvarado CX, Bailey DA, Ballinger S, Borycz JA, Canino BS, Cheatham N, Cook M, Dreher M, Duclos O, Eubanks B, Fairbanks K, Finley S, Forknall N, Francis A, Hopkins GP, Joyce EM, Kim S, Kirk NA, Kovalyak J, Lauchie SA, Lohff A, Maldonado C, Manley EA, McLin S, Mooney C, Ndama M, Ogundeyi O, Okeoma N, Ordish C, Padilla N, Patrick CM, Paterson T, Phillips EE, Phillips EM, Rampally N, Ribeiro C, Robertson MK, Rymer JT, Ryan SM, Sammons M, Scott AK, Scott AL, Shinomiya A, Smith C, Smith K, Smith NL, Sobeski MA, Suleiman A, Swift J, Takemura S, Talebi I, Tarnogorska D, Tenshaw E, Tokhi T, Walsh JJ, Yang T, Horne JA, Li F, Parekh R, Rivlin PK, Jayaraman V, Costa M, Jefferis GS, Ito K, Saalfeld S, George R, Meinertzhagen IA, Rubin GM, Hess HF, Jain V, Plaza SM. 2020. A connectome and analysis of the adult Drosophila central brain. *Elife* **9**. doi:10.7554/eLife.57443
Schlegel P, Bates AS, Stürner T, Jagannathan SR, Drummond N, Hsu J, Serratosa Capdevila L, Javier A, Marin EC, Barth-Maron A, Tamimi IF, Li F, Rubin GM, Plaza SM, Costa M, Jefferis GSXE. 2021. Information flow, cell types and stereotypy in a full olfactory connectome. *Elife* **10**. doi:10.7554/eLife.66018
Schlurmann M, Hausen K. 2007. Motoneurons of the flight power muscles of the blowfly Calliphora erythrocephala: structures and mutual dye coupling. *J Comp Neurol* **500**:448–464.
Schlurmann M, Hausen K. 2003. Mesothoracic ventral unpaired median (mesVUM) neurons in the blowfly Calliphora erythrocephala. *J Comp Neurol* **467**:435–453.
Schnell B, Ros IG, Dickinson MH. 2017. A Descending Neuron Correlated with the Rapid Steering Maneuvers of Flying Drosophila. *Curr Biol* **27**:1200–1205.
Shahidi R, Williams EA, Conzelmann M, Asadulina A, Verasztó C, Jasek S, Bezares-Calderón

LA, Jékely G. 2015. A serial multiplex immunogold labeling method for identifying peptidergic neurons in connectomes. *Elife* **4**. doi:10.7554/eLife.11147

Shepherd D, Sahota V, Court R, Williams DW, Truman JW. 2019. Developmental organization of central neurons in the adult Drosophila ventral nervous system. *J Comp Neurol* **527**:2573–2598.

Smiljanić J, Blöcker C, Edler D, Rosvall M. 2021. Mapping flows on weighted and directed networks with incomplete observations. *J Complex Netw* **9**:cnab044.

Soler C, Daczewska M, Da Ponte JP, Dastugue B, Jagla K. 2004. Coordinated development of muscles and tendons of the Drosophila leg. *Development* **131**:6041–6051.

Sterne GR, Otsuna H, Dickson BJ, Scott K. 2021. Classification and genetic targeting of cell types in the primary taste and premotor center of the adult Drosophila brain. *Elife* **10**. doi:10.7554/eLife.71679

Strausfeld NJ, Seyan HS, Milde JJ. 1987. The neck motor system of the flyCalliphora erythrocephala. *Journal of Comparative Physiology A* **160**:205–224.

Sun YA, Wyman RJ. 1997. Neurons of the Drosophila giant fiber system: I. Dorsal longitudinal motor neurons. *J Comp Neurol* **387**:157–166.

Takemura S-Y, Huang GB, Januszewski M, Lu Z, Marin EC, Preibisch S, Xu CS, Champion A, Cheong HSJ, Costa M, Eichler K, Knecht CJ, Li F, Morris BJ, Schlegel P, Stuerner T, Badalamente G, Bogovic J, Brooks P, Canino BS, Clements J, Cook M, Dunne CR, Fang S, Finley-May S, Funke J, George R, Gkantia M, Harrington K, Hayworth KJ, Hazlett A, Hopkins GP, Hsu J, Hubbard PM, Javier A, Kainmueller D, Katz WT, Korff W, Kovalyak J, Krzeminski D, Lauchie SA, Manley EA, Mooney C, Neace E, Nichols M, Okeoma N, Ordish C, Parekh R, Paterson T, Phillips EM, Plaza SM, Rivlin PK, Saalfeld S, Shepherd D, Smith C, Takemura S, Talebi I, Tamimi I, Tiscareno C, Trautman ET, Umayam L, Walsh JJ, Yang T, Zhao T, Hess HF, Rubin GM, Scheffer LK, Card G, Jefferis GSXE, Berg S. 2023. A Connectome of the Male Drosophila Ventral Nerve Cord. *bioRxiv*.

Tanouye MA, Wyman RJ. 1981. Inhibition between flight motoneurons in Drosophila. *J Comp Physiol* **144**:345–355.

Trimarchi JR, Murphey RK. 1997. The shaking-B2 mutation disrupts electrical synapses in a flight circuit in adult Drosophila. *J Neurosci* **17**:4700–4710.

Trimarchi JR, Schneiderman AM. 1995. Initiation of flight in the unrestrained fly, Drosophila melanogaster. *J Zool* **235**:211–222.

Trimarchi JR, Schneiderman AM. 1994. The motor neurons innervating the direct flight muscles of Drosophila melanogaster are morphologically specialized. *J Comp Neurol* **340**:427–443.

Tu MS, Dickinson MH. 1996. The control of wing kinematics by two steering muscles of the blowfly (Calliphora vicina). *J Comp Physiol A* **178**:813–830.

Vandervorst P, Ghysen A. 1980. Genetic control of sensory connections in Drosophila. *Nature* **286**:65–67.

van Hemmen JL, Schwartz AB. 2008. Population vector code: a geometric universal as actuator. *Biol Cybern* **98**:509–518.

von Philipsborn AC, Liu T, Yu JY, Masser C, Bidaye SS, Dickson BJ. 2011. Neuronal control of Drosophila courtship song. *Neuron* **69**:509–522.

von Reyn CR, Breads P, Peek MY, Zheng GZ, Williamson WR, Yee AL, Leonardo A, Card GM. 2014. A spike-timing mechanism for action selection. *Nat Neurosci* **17**:962–970.

Wang F, Wang K, Forknall N, Patrick C, Yang T, Parekh R, Bock D, Dickson BJ. 2020. Neural circuitry linking mating and egg laying in Drosophila females. *Nature* **579**:101–105.

Wang Q, Zhao C, Swank DM. 2011. Calcium and stretch activation modulate power generation in Drosophila flight muscle. *Biophys J* **101**:2207–2213.

Wang Y, Eddison M, Fleishman G, Weigert M, Xu S, Wang T, Rokicki K, Goina C, Henry FE, Lemire AL, Schmidt U, Yang H, Svoboda K, Myers EW, Saalfeld S, Korff W, Sternson SM, Tillberg PW. 2021. EASI-FISH for thick tissue defines lateral hypothalamus spatio-molecular organization. *Cell* **184**:6361–6377.e24.

Williamson WR, Peek MY, Breads P, Coop B, Card GM. 2018. Tools for Rapid High-Resolution Behavioral Phenotyping of Automatically Isolated Drosophila. *Cell Rep* **25**:1636–1649.e5.

Winding M, Pedigo BD, Barnes CL, Patsolic HG, Park Y, Kazimiers T, Fushiki A, Andrade IV, Khandelwal A, Valdes-Aleman J, Li F, Randel N, Barsotti E, Correia A, Fetter RD, Hartenstein V, Priebe CE, Vogelstein JT, Cardona A, Zlatic M. 2023. The connectome of an insect brain. *Science* **379**:eadd9330.

Wu M, Nern A, Williamson WR, Morimoto MM, Reiser MB, Card GM, Rubin GM. 2016. Visual projection neurons in the Drosophila lobula link feature detection to distinct behavioral programs. *Elife* **5**. doi:10.7554/eLife.21022

Wyman RJ. 1966. Multistable firing patterns among several neurons. *J Neurophysiol* **29**:807–833.

Wyman RJ, Thomas JB, Salkoff L, King DG. 1984. The Drosophila Giant Fiber System In: Eaton RC, editor. Neural Mechanisms of Startle Behavior. Boston, MA: Springer US. pp. 133–161.

Yamamoto D, Koganezawa M. 2013. Genes and circuits of courtship behaviour in Drosophila males. *Nat Rev Neurosci* **14**:681–692.

Yu JY, Kanai MI, Demir E, Jefferis GSX, Dickson BJ. 2010. Cellular Organization of the Neural Circuit that Drives Drosophila Courtship Behavior. *Current Biology*. doi:10.1016/j.cub.2010.08.025

Zheng Z, Scott Lauritzen J, Perlman E, Robinson CG, Nichols M, Milkie D, Torrens O, Price J, Fisher CB, Sharifi N, Calle-Schuler SA, Kmecova L, Ali IJ, Karsh B, Trautman ET, Bogovic JA, Hanslovsky P, Jefferis GSX, Kazhdan M, Khairy K, Saalfeld S, Fetter RD, Bock DD. 2018. A Complete Electron Microscopy Volume of the Brain of Adult Drosophila melanogaster. *Cell* **174**:730–743.e22.

Zwarts L, Versteven M, Callaerts P. 2012. Genetics and neurobiology of aggression in Drosophila. *Fly* **6**:35–48.